UNIVERSITÀ DEGLI STUDI DI SALERNO

Dipartimento di chimica e biologia

Ph.D. in Chemistry
XXXI Ciclo

Ph.D. Thesis

Charge transfer in organic materials with potential applications in electronics

Tutor:

Prof. Andrea Peluso

Coordinator:

Prof. Gaetano Guerra

PhD student:

Alessandro Landi
Matr. 8800100016

To my parents:
my support, my sanity, my fortune

"It is not the critic who counts; not the man who points out how the strong man stumbles, or where the doer of deeds could have done them better. The credit belongs to the man who is actually in the arena, whose face is marred by dust and sweat and blood; who strives valiantly; who errs, who comes short again and again, because there is no effort without error and shortcoming; but who does actually strive to do the deeds; who knows great enthusiasms, the great devotions; who spends himself in a worthy cause; who at the best knows in the end the triumph of high achievement, and who at the worst, if he fails, at least fails while daring greatly, so that his place shall never be with those cold and timid souls who neither know victory nor defeat."
(Theodore Roosevelt)

Contents

Abstract

Search for low cost electronic materials has led towards the synthesis and the employment of organic semiconductors (OSCs), a class of materials that combine the electronic advantages of semiconducting materials with the chemical and mechanical benefits of organic compounds. Despite the intense research effort, new OSCs have usually been discovered by trial and error and, even retrospectively, it was not always possible to explain why some materials exhibit better performances than others. A more efficient approach is now required and, in this respect, the use of computer-aided materials discovery can be highly beneficial. Increasing numbers of new OSCs have already been designed and improved through computational modeling, which requires the efficient simulation of charge transport (CT) processes taking place in OSC-based devices.

In this thesis we study and compare the relative performances of different models in the simulations of charge transport in OSCs.

In the first part we focus on the different properties of organic semiconductors with respect to their inorganic counterpart, their benefits and their drawbacks, restricting our analysis to organic crystalline semiconductors, which show the highest mobilities among all OSCs. Then we describe some of the most widely studied classes of OSC materials, showing some cases in which theory-guided material design has already been applied leading towards new materials with improved electronic performances.

In the second part of this thesis we dwell on the unique physical properties of organic semiconductors and on the reasons that animates the still topical debate about the most appropriate theoretical model for the CT description in these materials. Then, we briefly analyze strengths and drawbacks of five theoretical models: the Marcus theory, the Fermi Golden Rule (FGR), the Second Order Cumulant expansion of the density matrix (SOC), the quantum dynamics, and a recently developed approach, the Transient Localization Theory (TLT). In particular we describe some approximated strategies that significantly speed up the computations still ensuring accurate results.

In the third part we apply the abovementioned models to the description of charge transport in some of the most studied OSCs, comparing their predictions with experimental data and discussing the relative performances of each method. Our results show that SOC and TLT predictions are in good agreement with experimental data, the latter being the method of choice because of its low computational cost and physically well-sound assumptions.

In the last part of this thesis we focus on the simulation of CT in DNA oligomers, a topical issue since long range charge migration makes DNA a potentially well-suited material for nanoelectronics. Our analysis reproduces in a quantitative way published experimental data and allows us to reconcile experimental results disagreeing about the role of thymine bridges in CT across DNA oligomers.

List of publications

- <u>Alessandro Landi</u>*, R. Borrelli, A. Capobianco, A. Velardo, and A. Peluso, "A Second Order Cumulant Approach for the Evaluation of Anisotropic Hole Mobility in Organic Semiconductors", *J. Phys. Chem. C*, http://dx.doi.org/10.1021/acs.jpcc.8b08126 (2018)

- <u>Alessandro Landi</u>, and A. Troisi*, "Rapid Evaluation of Dynamic Electronic Disorder in Molecular Semiconductors", *J. Phys. Chem. C*, **122**, 18336-18345 (2018)

- <u>Alessandro Landi</u>, R. Borrelli, A. Capobianco, A. Velardo, and A. Peluso*, "Hole Hopping Rates in Organic Semiconductors: A Second-Order Cumulant Approach", *J. Chem. Theory Comput.*, **14**, 1594-1601 (2018)

- A. Capobianco*, <u>Alessandro Landi</u>, and A. Peluso, "Modeling DNA Oxidation in Water", *Phys. Chem. Chem. Phys.*, **19**, 13571-13578 (2017)

- A. Capobianco, R. Borrelli, <u>Alessandro Landi</u>, A. Velardo, and A. Peluso*, "Absorption Band Shapes of a Push-Pull Dye Approaching the Cyanine Limit: A Challenging Case for First Principle Calculations", *J. Phys. Chem. A*, **120**, 5581-5589 (2016)

- R. Borrelli*, A. Capobianco, <u>Alessandro Landi</u>, and A. Peluso, "Vibronic Couplings and Coherent Electron Transfer in Bridged Systems", *Phys. Chem. Chem. Phys.*, **17**, 30937-30945 (2015)

---

* Corresponding Author

Part I

ORGANIC SEMICONDUCTORS AND DEVICES

Chapter 1

Introduction

In the last years electronic industry has rapidly evolved, improving device performances and at the same time reducing both the size of the components and their costs. The search for low cost electronic materials has led towards the synthesis and the employment of organic semiconductors (OSCs), a class of materials that combine the electronic advantages of semiconductors with the chemical and mechanical benefits of organic compounds such as plastics [1–3]. In other words, the ability to absorb/emit light and conduct electricity occurs in a material whose chemical/physical properties can be easily tuned by using different functional group, with the aim of tailoring electronic properties, of making it soluble, or of gaining good mechanical properties.

Applications of materials showing all these appealing characteristics deposited over flexible substrates (like solar cell foils or lighting sheets) seem attractive, and indeed OSCs currently have several applications in devices like organic field-effect transistors (OFET) [4, 5], organic light emitting diodes (OLED) [6], and organic solar cells [7]. The large-scale exploitation of organic semiconductor materials in the xerographic process of any common photocopier machine is present in any typical office, while OLED-based displays are, for example, employed in the Galaxy smartphone series

13

by Samsung, and are thus also widely distributed (fig. 1.1). The widespread interest in organic semiconductors will probably increase in the next years and, according to a recent study by IDTechEx, the organic electronics market will grow from \$29.28 billion in 2017 to \$73.43 billion in 2027 [8].
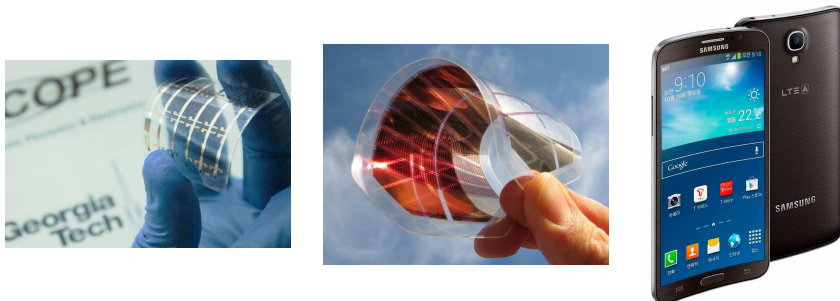

Figure 1.1. Examples of present organic semiconductor applications: an OFET (left), a flexible organic solar cell (middle) and the Galaxy round smartphone, whose display is OLED-based (right).

Even though the widespread interest in OSCs is relatively recent, the first studies on conductivity, photoconductivity, photoelectric effect, and fluorescence of organic solids date back to the beginning of the twentieth century [3, 9–11]. Even electroluminescence studies have been reported in the fifties by Bernanose [12] on a cellulose film doped with acridine orange. The main period of research on molecular crystals such as naphthalene and anthracene, however, took place in the years from 1950 to 1980. This field gained importance from the report of electroluminescence in an anthracene crystal by Pope in 1963 [13], and by Helfrich and Schneider in 1965 [14]. The technological development of organic semiconductors took off with the discovery of electroluminescence in about 100 nm thin amorphous organic films: in 1987, Tang and Van Slyke [15] reported an amorphous thin film LED made with the molecule Alq3 (Tris(8-hydroxyquinolinato)aluminium) with an external quantum efficiency (emitted photons to injected electrons) of 1%, a high value at that time. This was followed in 1990 by the report of

electroluminescence below 14 V in a 100 nm thick film of the non-doped π-conjugated polymer poly(paraphenylene vinylene) (PPV) [16]. Since then, enormous progresses have been made in the field of organic electronics (fig. 1.2), and the typical path to performance increase could be described as a two-stage process:

1. A new organic semiconductor is synthesized or used for the first time as the active layer in organic electronics.

2. The film deposition parameters for the semiconducting organic layer are optimized to obtain the most advantageous structural and morphological characteristics for improved performances.
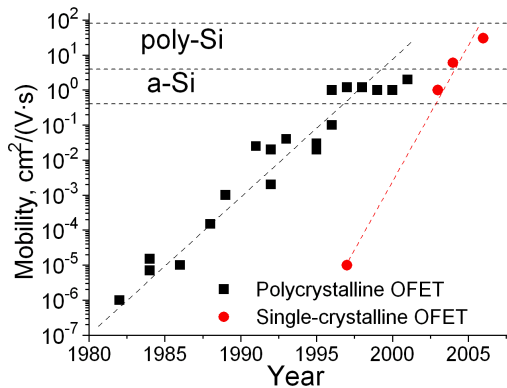
Figure 1.2. Evolution of carrier mobility in time for OFETs. The regions delimited by dashed lines identify typical μ values of amorphous and polycrystalline Si. Data from ref. [17].

One of the figure of merit used to characterize the electronic performances of a semiconductor is the charge carrier mobility μ, a quantity describing how fast an electron or a hole migrates in the material. In fig. 1.2 it is shown that, as the years pass, an increase in mobility is observed, either by improving the processes used for the fabrication of the transistors or by synthesizing new organic materials.

15

Research in the field of organic semiconductors is still very active, leading in recent years to materials displaying record mobilities of almost 50 cm^{2}V^{-1}s^{-1} [17–19]. This value exceeds the performances of amorphous and polycrystalline silicon [4, 20], making organic semiconductors a promising alternative to inorganic ones. This attempt to substitute inorganic semiconductors stems from the fact that, despite their good electronic properties, they suffer from a range of problems, such as rigidity, brittleness, short lifetime and high cost. Moreover, it is difficult to achieve a variation in their electronic properties, as, for instance, a slight modification in their wavelength emission. Finally, inorganic semiconductors usually have to be processed under demanding conditions and show compatibility problems with various substrates. On the contrary, organic semiconductors have a lot of appealing properties, such as light weight, mechanical flexibility, relatively low cost and a wide range of possible chemical modifications, that makes it possible to accurately tune their electronic properties. Besides, OSCs-based devices can be produced with a variety of solution-processing techniques or vacuum deposition methods and can be easily deposited over large substrates of paper or plastic.

Another important difference between inorganic and organic materials is that the "semiconducting nature" differs strongly between them. Silicon, GaAs and in general all inorganic semiconductors have low band gaps (e.g. 1.1 eV for Si and 1.4 eV for GaAs). For that reason, even at room temperature, charges can be promoted from the valence band into the conduction band by thermal excitation, reaching a concentration of charge carriers given by $N = N_0 e^{E_g/(2k_{\mathrm{B}}T)}$, where N_0 is the effective density of valence band states and E_g is the band gap. Furthermore, the dielectric constant is quite large ($\epsilon_r \approx 11$ [3]) so that Coulomb interactions between electrons and holes are unimportant due to dielectric screening, and light absorption at room temperature can create free electrons and holes. In contrast, the conductivity of organic semiconductors is extrinsic and results from

the injection of charges at electrodes, from doping and from the dissociation of photogenerated electron-hole pairs that are bound by their mutual Coulomb attraction (since ϵ_r is around 5 [21], quite lower than in inorganic semiconductors).
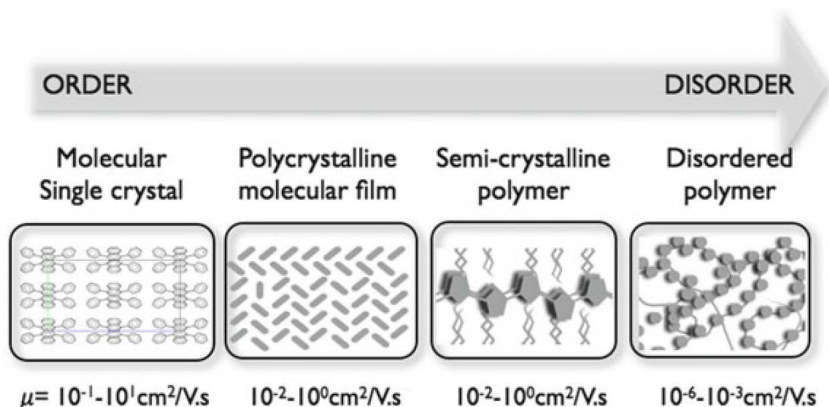
Figure 1.3. Pictorial representation of the decrease of mobility in a progression from single molecular crystals to disordered polymers. Reproduced from ref. 22.

Even if the semiconducting properties in all organic semiconductors have a similar origin, it is useful to distinguish between the following three classes of organic semiconductors:

1. Amorphous molecular films, i.e. organic molecules deposited as an amorphous film through evaporation or spin-coating. Thin amorphous films of molecules are usually employed for device applications such as OLEDs.

2. Molecular crystals. The charge mobilities that can be obtained in molecular crystals are high compared to those in noncrystalline organic materials [4], rendering them relevant for transistor applications.

17

3. Polymer films. Usually, they are processed from solution, allowing for a range of deposition techniques including simple spin-coating, ink-jet deposition, or industrial reel-to-reel coating.

Despite its simplicity, this basic classification is useful since OSCs' excited states, photophysical properties, and mobilities significantly differ depending on the order and coupling in the solid, as outlined in fig. 1.3, where we focus on the variation of the mobility as a function of the degree of disorder. This great difference, with performances differing by orders of magnitude, is related to the fact that defects, grain boundaries, impurities, thermal disorder, can act as traps for the charge carrier, or they can significantly distort the perfect geometrical arrangement present in an ideal single crystal, leading to a less efficient geometry for charge transport. For the same reason, subtle changes in the packing patterns can result in great differences in the semiconductivity of a material.

One of the most striking examples among the crystal structure-property relationship studies in OSCs is perhaps the case of rubrene. With a record single crystal OFET mobility of about 20 cm^{2}V^{-1}s^{-1} [23], rubrene can be viewed as a remarkable improvement of tetracene ($\mu \approx 2.4$ cm^{2}V^{-1}s^{-1} [24]), from which it differs for two phenyl groups (figure 1.4). This difference
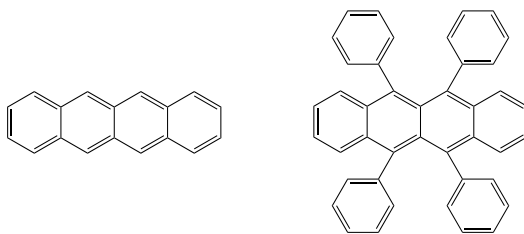

Figure 1.4.   Molecular structure of tetracene (left) and rubrene (right).

could be explained because, although the phenyl groups added to tetracene backbone do not participate in the π-conjugation, they help the backbone to π-stack very close to one of the maxima of the electronic coupling surface

[25].

Throughout this thesis, we will focus on organic molecular crystals, the class showing the highest experimental mobilities recorded up to now. Today's technological interest in organic semiconducting crystals arises mostly from the field of organic field-effect transistors (OFETs), which we will describe in the next sections.

1.1 Transistors

Transistors, probably the most important building blocks of modern electronic devices, were proposed for the first time in a patent application by Lilienfeld in 1930 [26], being for more than a decade only a conceptual device because further techniques were needed in order to actually produce them. Finally, they were successfully built by Shockley, Bardeen and Brattain at AT&T's Bell Labs in 1947, an accomplishment for which these three scientists were awarded the 1956 Nobel Prize in Physics. In today's applications, billions of them are used as switches or amplifiers in microelectronics, integrated circuits, computers and any other electronic device. There are two major parameters by which the performance of a transistor is assessed, that is the on-off ratio (high on-off ratio implies that a low driving voltage is needed to achieve a good signal to noise ratio) and the switching frequency (the maximal frequency at which the OFET can operate). Both depend linearly on the charge carrier mobility, so that, in essence, the crucial device parameter is the charge carrier mobility.

In general, a transistor can be defined as a semiconductor device carrying three electrodes, where the third is used to control the current flowing along the "channel" between the other two electrodes, with the aim of switching or amplifying the signal.

There are two basic types of transistors, the bipolar transistor and the field-effect transistor (FET) (fig. 1.5). The main difference between them is the way the current flowing in the channel is controlled. In the bipolar

transistor the control electrode (called "base") is directly connected to the channel, and the current between the other two electrodes ("emitter" and "collector") is regulated by the current flow from the base. For that reason the bipolar transistor is defined to be current-controlled. On the contrary, in the FET no current can actually flow from the control electrode (the "gate") into the semiconducting channel between the two electrodes ("source" and "drain"), since the control electrode is separated from the channel by an insulator. With this architecture, control electrode, insulating layer, and the semiconducting channel form a capacitor. When a voltage is applied to the gate, it creates an electric field inducing charges in the insulator layer, which modify the current flow from source to drain in the channel capacitively, thus giving rise to the name of "field-effect" transistor. Because of its modus operandi, the FET is defined to be voltage-controlled. Another difference between these two types of transistors is that bipolar transistor are built combining p-type and n-type semiconductors, while FET requires only one type of semiconductor.
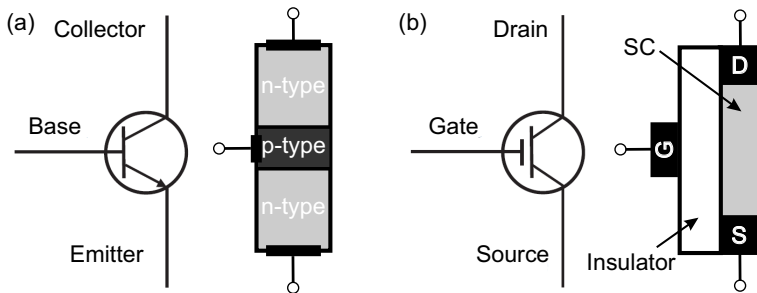
Figure 1.5. Symbol in a circuit diagram and scheme of (a) bipolar transistor (in the specific a n-p-n layer structure) and (b) field-effect transistor.

In 1965 Gordon Moore stated the law named after him: "the number of transistors in an integrated circuit doubles roughly every two years" [27]. This prediction still holds true today, but it probably will not work after 2020 or so, because the size of individual transistors is approaching

the fundamental barrier of atomic dimensions, with further miniaturization impossible for current semiconducting materials. Indeed, with the great progresses made since the early 20th century, devices that formerly occupied large rooms such as the first computer can now be carried in a pocket. Nowadays, research is focusing on the development of electronic circuits based on different materials, aiming for cheaper production, environmental sustainability or novel functionalities, features that, as previously discussed, should be ensured by organic semiconductors. The most important advantage is the expected low production cost, since the layers can be deposited and patterned around room temperature using a combination of solution-processing and direct-write printing, ensuring a low-cost fabrication of printed circuits, with the particular advantage of possible deposition over flexible substrates such as polymethylmethacrylate films.

1.1.1 Operational principles and experimental evaluation of mobility

In this section we will present in a simple manner the operational principles of OFET and we discuss the principal experimental techniques for the evaluation of the mobility in a semiconductor.
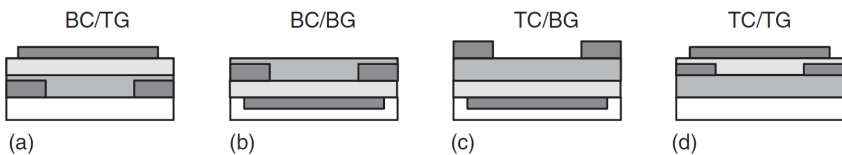
Figure 1.6. Different configurations for OFETs: (a) bottom contact, top gate, (b) bottom contact, bottom gate, (c) top contact, bottom gate, (d) top contact, top gate (rarely used). The insulator is indicated by the light gray layer, the organic semiconductor by the middle gray layer. Electrodes are shown in dark gray, while the substrate is shown in white. Reproduced from ref. 3.

Several configurations (fig. 1.6) are possible for OFET used in modern

devices. In all of them the gap between the source and drain electrodes, i.e. the channel length L, is on the order of 100 μm while the channel width is typically up to a few millimeters.

Regardless of the configuration, as outlined in the introduction, charge carriers are injected in an OFET from the electrodes and the current flowing in the transistor is adjusted through the variation of the number of charge carriers accumulated at the semiconductor/insulator interface by modulating the gate voltage. If, for example, a negative voltage V_g is applied to the gate, positive charges are attracted from the source electrode into a narrow ($\leq$5 nm) semiconductor region next to the dielectric (fig. 1.7). This
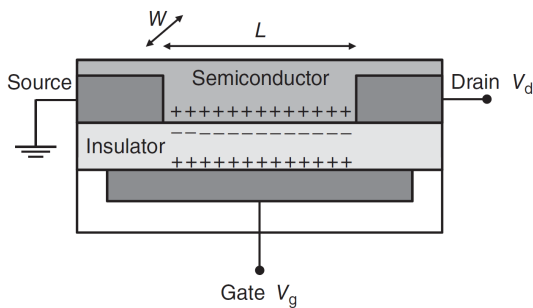
Figure 1.7. Illustration of the working principle of an OFET. Across a width W, source and drain electrode are separated by a semiconductor channel of length L. Reproduced from ref. 3.

induces the accumulation of positive charges in the insulator, leading, in an ideal (i.e. trap-free) transistor, to a number of charges proportional to the capacitance per unit area of the dielectric, C_i, and to the gate voltage V_g. If now a negative potential V_d is applied to the drain electrode, these positive charge carriers will migrate leading to a current flowing in the transistor. However, in real transistor some charges will be trapped, so current will flow only if the number of generated charges is greater than the number of the traps, in other words, if the gate voltage is greater than a threshold value V_{th} depending on the material used. The interested reader is referred

to ref. [3] for a formal discussion of the dependence of the current I and the other parameters in an OFET. Here we will limit to point out that when varying V_d it is possible to distinguish two regions in a current-voltage plot (fig. 1.8):
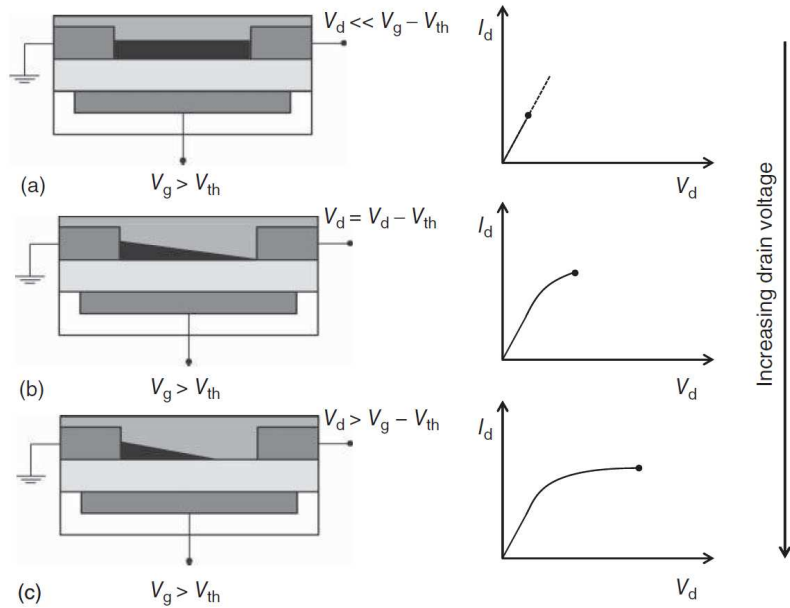
Figure 1.8. Diagrams illustrating the performance of an OFET at different applied voltages. The channel formed in the device as well as the current-voltage characteristics are shown for (a) linear regime, (b) start of saturation regime at pinch-off, (c) saturation regime. V_d, V_g, and V_{th} denote drain voltage, gate voltage, and threshold voltage, respectively. Reproduced from ref. 3.

- The linear regime ($V_d \ll V_g - V_{th}$). Here the transistor current obeys Ohm's law, i.e. I increases linearly with V_d.

- The saturation regime ($V_d > V_g - V_{th}$). When $V_d = V_g - V_{th}$, the concentration of mobile charge carriers reduces to zero at the drain electrode, and, as long as V_d further increases, the point where the

concentration of mobile charge carriers reaches zero moves towards the source, thus slightly shortening the actual channel. In this case, a depletion zone establishes near the drain, but current can still flow since the charges can overcome the narrow depletion zone. However the current remains constant as V_d increases.

As shown in ref. [3], the *I-V* expressions for the two regimes are:

$$I_d = \frac{W}{L}\mu_{lin}C_i\left(V_g - V_{th}\right)V_d \tag{1.1}$$

and

$$I_d = \frac{W}{2L}\mu_{sat}C_i\left(V_g - V_{th}\right)^2 \tag{1.2}$$

Eq.s 1.1 and 1.2 are often used [2, 28] to experimentally evaluate the carrier mobility of a semiconductor. It is possible to derive equivalent equations when the length of the channel is reduced, accounting also for the contact resistance by using a four probe measurements [29, 30]. It should also be noted that, in more accurate measurements, the dielectric constant (ϵ_r) of the insulating layer can affect the mobility, because the polarization induced by the charge carriers in the channel across the insulator affect the motion of the charges themselves, leading to slightly lower mobilities as ϵ_r increases [31, 32].

Another popular technique for the evaluation of the mobility is the time-of-flight (TOF) method [33], one of the first methods proposed for the experimental measurement of the mobility (the first experiments were conducted by Kepler [34] and Leblanc [35] in the 60s on anthracene crystals).

The experimental apparatus for a TOF measurement (fig. 1.9) consists in a semiconducting layer of a few μm sandwiched between two electrodes with an applied electric field of about 10^4-10^6 V/cm. The material is irradiated with a short laser pulse to generate a narrow sheet of charges of opposite signs that move towards the electrodes. By irradiating next to one of the electrodes, say the anode, the electrons immediately leave, while the holes have to travel through all the semiconducting layer to reach the
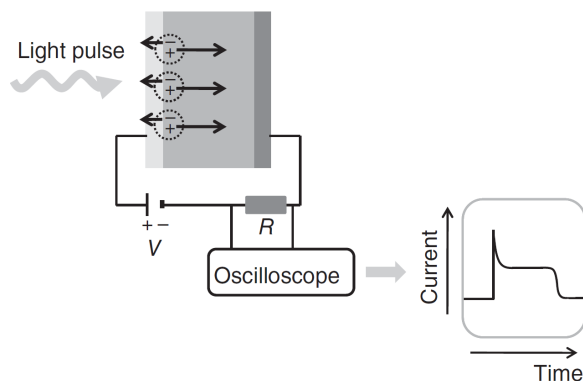
Figure 1.9. Illustration of the TOF method. A laser pulse creates electron-hole pairs close to the front electrode, chosen to be the anode, so that electrons leave the device immediately, while holes move through all the semiconducting layer reaching the counter electrode, inducing a displacement current monitored by an oscilloscope. The sudden drop of the current indicates that the holes reach the cathode. Electron mobility can be measured by inverting the polarity of the applied electrical field.

cathode. The time t_{tr} employed by the charges to arrive to the electrode is directly proportional to the distance d and inversely proportional to the applied electric field F and the mobility μ, i.e.

$$\mu = \frac{d}{Ft_{tr}} = \frac{d^2}{Vt_{tr}},\tag{1.3}$$

where V is the applied voltage. As represented in fig. 1.9, a typical TOF signal consists in a sharp peak, a plateau and a final decay. The peak occurs immediately after charge carriers generation because they have different energies and highest energetic carriers quickly migrate towards lower energy sites. This phenomenon always happens in organic materials, which have a distribution of sites at different energies. The plateau is due to the following motion of the carrier towards the electrode, so the transition time t_{tr} for the evaluation of the mobility is usually taken to be at the intersection between the plateau and the final tail.

However, the values obtained with the two techniques above described are affected by the purity and order of the materials (for example, μ values of 0.1 [36], 0.5 [37] 1.5 [38], 3 [39], 6 [40] up to 35 cm^{2}V^{-1}s^{-1} [18] have been reported for pentacene crystals depending on the experimental conditions), a problem that is unavoidable with the methods measuring the mobility over macroscopic distances (that is, on the scale of 1 mm). A relatively recent technique, the Pulse-Radiolysis Time-Resolved Microwave Conductivity (PR-TRMC) works over microscopic distances, so it should reasonably be less dependent on the macroscopic structure of the material and its fabrication. In this technique (see fig. 1.10), the sample is excited by
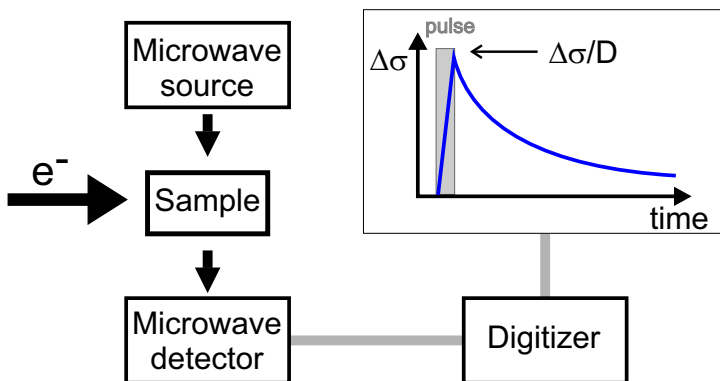
Figure 1.10. A very simplified schematic representation of the PR-TRMC equipment. $\Delta\sigma$ is the change of conductivity at the end of the pulse. Adapted from ref. 41.

a short pulse (5-20 ns) of electrons with energy in the MeV range, creating free carriers and the change in electrical conductivity $\Delta\sigma$ is measured via the decrease in the microwave power reflected by the sample

$$\Delta\sigma = e \sum \mu N_{e-h}. \qquad (1.4)$$

Here N_{e-h} is the density of charges generated by the irradiation, estimable dividing the energy of the electron pulse by the energy required to create

an electron-hole pair and a factor accounting for the fraction of initially formed charge carrier pairs which survive charge recombination [41].

This technique is electrode-free so it is not affected by the morphology of the semiconductor-electrode contact, plus the motion of the charges is measured on a very local spatial scale (depending on the frequency of the microwaves hitting the sample: the higher the frequency, the smaller the region probed) so it is less affected by impurity and disorder of the materials. In general, PR-TRMC gives the highest mobility values obtained for the material under examination ("intrinsic mobilities"), for example a μ of about 600 cm^{2}V^{-1}s^{-1} has been reported for an accurately tailored polyparaphenylene derivative [42].

It should be noted that this technique only evaluate the sum of electron and hole mobility. If interested in electron mobilities usually a doping with a strong hole scavenger like tetramethyl-p-phenylenediamine is used, while for hole mobility the sample is put in an environment saturated with oxygen (if possible), an efficient scavenger for excess electrons. Unfortunately, these "tricks" cannot be applied to all the samples.

Other methods are used for the evaluation of charge carrier mobilities in organic semiconductors. An exhaustive list can be found for example in ref. [3].

1.2   Materials
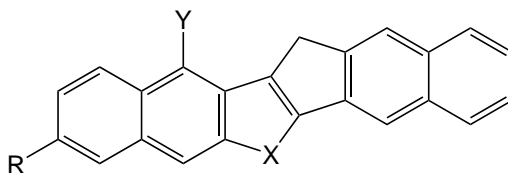
Figure 1.11.   A typical OSC structure. The conjugated core can be constituted by 5-member or 6-member aromatic rings.

The great majority of the materials of interest in organic electronics have a structure that can be derived from fig. 1.11 by varying the length of the conjugated core, replacing one or more C atoms of the conjugated rings with an heteroatom (e.g. X in fig. 1.11), inserting one or more substituents on the core (e.g. Y in fig. 1.11) or adding side chains (e.g. R in fig. 1.11). Usually the first three modifications influence the electronic properties while side chains are incorporated for enhancing the solubility, in order to enable solution processing techniques when devices are built. We will describe in the following some of the most popular OSCs' classes (fig. 1.12).
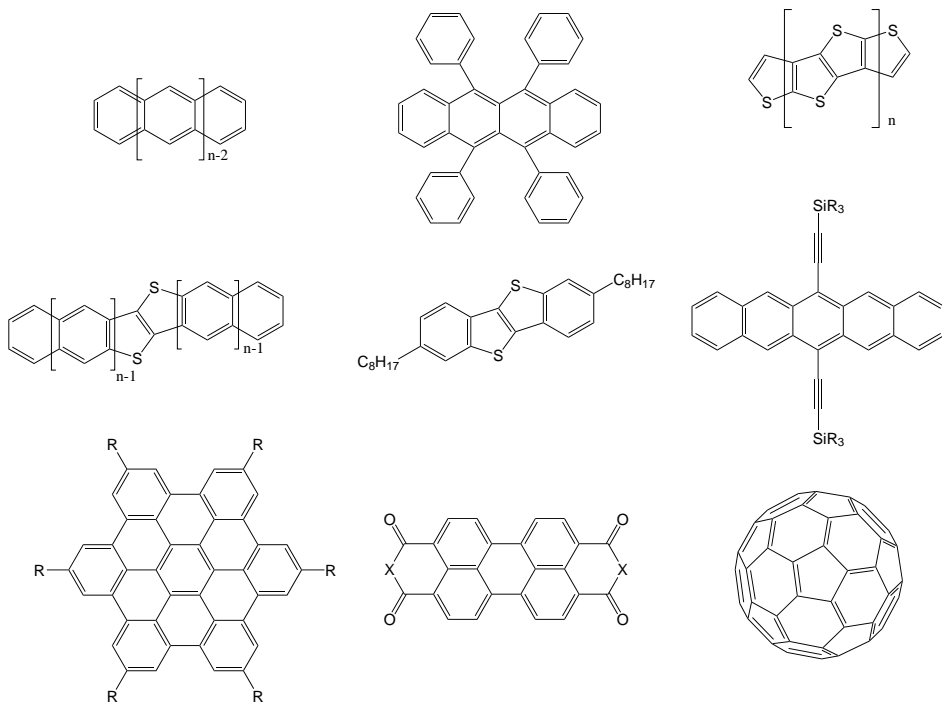
Figure 1.12.   Structures of some OSCs. Top: oligoacenes (left), rubrene (middle) oligothienoacenes (right); Middle: dithienoacenes (left), C8-BTBT (middle), TIPS-pentacene (right, R = isopropyl group); Bottom: hexabenzocoronene (left), perylene (middle), fullerene C60 (right).

Oligoacenes This class, formed by molecules consisting in linear fused benzene rings, has been the first class of organic semiconductors investigated [43], still being nowadays among the OSCs with best performances. The smallest interesting molecule in this class is anthracene, widely studied for its electronic and photoelectronic properties since the second half of the twentieth century [44] (see the introduction), showing a mobility of about 1 cm^{2}V^{-1}s^{-1} [44, 45]. Its superior homologue, tetracene, is constituted by 4 benzene rings, so it has a longer conjugation length. It has been widely studied and mobilities in the range 0.4-2.4 cm^{2}V^{-1}s^{-1} [24, 46] have been reported. Pentacene, constituted by five fused benzene rings, is probably the most studied organic semiconductor and several attempts have been made to accurately control the crystal polymorph, its morphology and its purity when constructing OFETs, in order to reach higher and higher mobilities [18, 38, 40, 47]. In particular, very high mobilities (up to 35 cm^{2}V^{-1}s^{-1}) have been reported when 6,13-pentacenequinone (the product of oxidation of pentacene and its principal impurity) concentration has been accurately lowered under 0.02% [18]. Despite this result, the large majority of μ reported for pentacene falls in the range 1-5 cm^{2}V^{-1}s^{-1} [38–40, 48–50]. The principal limit to the application of pentacene is its poor air-stability, which leads to a rapid decay of the device performances in time: as noted above, its oxidation product (pentacenequinone) is also its principal impurity. The problem of air-stability becomes increasingly worse when considering higher homologues such as hexacene, heptacene, octacene and nonacene, which are not only air-unstable but also chemically labile, undergoing reactions like cycloaddition and homodimerization [51], to such an extent that for the last three ones after the synthesis it was impossible to study their electronic properties [52].

Several structural modifications have been proposed in order to improve oligoacenes stability and performances. The first example was rubrene, a sort of modified tetracene, from which it differs for four phenyl groups, which induce a molecular stacking very close to one of the maxima of the

transfer integral surface [25], leading to mobilities almost one order of magnitude greater than tetracene. Given its rather large mobility, rubrene has been the subject of many recent studies, both experimentally and theoretically [23, 25, 53–56].

Other modifications, made in the attempt to solve the previously mentioned drawbacks of the oligoacenes (air instability, high temperature deposition) involve replacements of benzene rings with other heteroaromatic rings, addition of substituents to the aromatic core or inclusion of EWG (electron-withdrawing) groups, leading to different classes of materials which we will briefly describe in the following.

Oligothienoacenes These molecules consist in linear fused thiophene rings, so they can be viewed as oligoacenes where all benzene groups have been replaced by thiophenes. This substitution leads to a lower degree of aromaticity and also to an increased air-stability with respect to oligoacenes. Indeed cyclic voltammetry studies of oligothiophenes showed the reversibility of the oxidation (i.e. a good stability of the oxidized species) [57]. Unfortunately, molecules constituted by only fused thiophene rings showed poor performances ($\mu < 1$ cm^{2}V^{-1}s^{-1} [4]), so research focused on systems combining benzene and thiophene rings with the idea of keeping the excellent performances of oligoacenes and at the same time the improved stability of the oligothienoacenes.

Dithiophenes The best results were obtained putting two thiophene rings in the middle of an oligoacene structure, obtaining BTBT (benzo-thieno[3,2-b]benzothiophene; two benzene rings), DNTT (dinaphtho[2,3-b:2',3'-f]thieno[3,2-b]thiophene; four benzene rings) and DATT (dianthra-[2,3-b:2',3'-f]thieno[3,2-b]thiophene; six benzene rings). The first one is basically unused because of its poor processability [58] but its alkylated derivatives (see next section) show good electronic properties. In an attempt to extend the π-conjugated system of BTBT a very simple synthesis was proposed by Yamamoto et al. [59] for the DNTT molecule, which shows a good stability and processability, along with excellent mobilities

(8.3 $cm^2V^{-1}s^{-1}$ [60]). Finally, DATT constitutes an interesting example, because it has been identified as a very promising material by theoretical simulations, before its actual synthesis and characterization (we will discuss in detail this point later). Single crystal OFET measurement has led to μ higher than 10 $cm^2V^{-1}s^{-1}$ for this molecule [61], but, most importantly, DATT-based OFET do not show significant loss of performances when stored in ambient conditions even for a long time [4, 51].

DBTDT (dibenzo-thieno-dithiophene) has been synthesized by substituting the three central benzene rings of pentacene molecule with three thiophene rings. However, this molecule shows lower performances than the dithiophenes, reaching mobilities of 1-4 $cm^2V^{-1}s^{-1}$ [62, 63]

Core-substituted oligoacenes Another modification is the attachment of a side chain to the conjugated core, usually to increase the solubility and thus improving the processability by solution techniques. Moreover alkyl substituents on pentacene have been shown to improve its air stability [4]. However, although the side chains do not contribute to charge transport, they can still have an impact on the electronic properties of the semiconductors, by affecting the molecular packing and thus leading to quite different mobilities. Two rather interesting examples are the 6,13-bis(triisopropylsilylethynyl)pentacene (TIPS-pentacene) and the alkylated BTBT. The former consists of a pentacene core substituted in the peri-position with two triisopropylsilylethynyl groups, leading to a shift in the molecular arrangement from a herringbone pattern to a face-to-face π-stacking. Mobilities ranging from 0.7 to about 1 $cm^2V^{-1}s^{-1}$ [53, 64] have been reported for TIPS-pentacene. Analogously, various alkyl groups (ranging from C5 to C14 [65]) have been added to BTBT in the molecular long-axis direction of the core to increase its solubility, leading to materials with good semiconducting properties, like C8-BTBT ($\mu \approx 3$ $cm^2V^{-1}s^{-1}$ [66]) or C13-BTBT ($\mu \approx 2$ $cm^2V^{-1}s^{-1}$ [65]).

Another popular approach is the attachment of electron withdrawing groups

(in particular halogenes) to oligoacenes conjugated core in order to improve their air-stability. Fluorination and chlorination are the most used approaches to achieve air-stability in this context, leading for example to perfluoropentacene [67], partially chlorinated tetracene [68] partially fluorinated or partially chlorinated TIPS-pentacene [69]. Halogen substitution usually leads towards materials showing ambipolar or even n-type semiconducting properties, indeed for perfluoropentacene electron mobility of 0.11 $cm^2V^{-1}s^{-1}$ [67] but no p-type charge transport have been reported.

Discotic liquid crystals (DLC) These materials are formed by disc-like molecules, such as triphenylene or hexabenzocoronene, constituted by a conjugated core substituted with aliphatic chains. These molecules stack in a column-like structure, leading to a 1-dimensional charge transport. Even if they obviously cannot reach the same degree of order of a crystal, their columnar organization is ordered enough to reach μ of 1 $cm^2V^{-1}s^{-1}$ [70] or higher (up to 6.8 $cm^2V^{-1}s^{-1}$ derivatizing hexabenzocoronene with groups allowing the formation of more ordered self-assembling structures [71]). Unfortunately, except for these special case, in general DLCs have the drawback of a higher degree of impurities and defects with respect to organic crystals, so they show in general lower mobilities.

n-type semiconductors: Fullerenes and others Fullerene (C_{60}) and its derivatives are the most used acceptors in organic photovoltaics, because of their large electron affinity, high electron mobility, and large conjugated system which helps charge separation through delocalization. Mobilities of about 1.5 $cm^2V^{-1}s^{-1}$ have been reported [72, 73]. Related compounds are the carbon nanotubes, for which exceptional mobility of 10^5 $cm^2V^{-1}s^{-1}$ has been obtained [74]
Another widely studied n-type semiconductor is perylene. The peculiarity of perylene resides in its crystal packing, where dimers rather than single molecules are arranged in a herringbone pattern. It can be also functionalized with EWG moieties (X=Oxygen or X=NH in fig. 1.12) leading to n-type behaviour, with mobilities around 1.2 $cm^2V^{-1}s^{-1}$ [75].

The great majority of materials here presented are generally used as p-type semiconductors (unless otherwise noted). However, the distinction between n-type or p-type semiconductors is not related to their intrinsic ability to transport electrons or holes [2], since in several organic materials electron and hole mobilities are similar [76, 77]. Instead, this demarcation is based on the ease of injecting electron or holes in the materials, i.e. on the relative electron affinity or ionization potential with respect to the electrode Fermi level. In this respect, it has been pointed out that low electron μ can be due to extrinsic effects like traps or the instability of the radical anions with respect to water or hydroxyl groups. Indeed, the mobility of electrons in polythiophene increases when the SiO_2 is treated to cover free hydroxyl group [2, 78].

1.3   Computer Aided Material Science

As outlined in the previous sections, new organic semiconductors have usually been discovered by chance, and even after their applications it was not always possible to explain why some materials had higher performances than others. In other words, up to now material science has progressed following these steps: synthesis, structural and electronic characterization and only retrospectively theoretical studies to understand structure-property relationship. However, many authors [22, 54, 79] are advocating a theory-guided material design to rationalize and speed up the pace of discovery of new materials, that up to now has relied on a trial and error methodology.

Unfortunately, a complete de novo design would require crystal structure prediction, which is nowadays one of the major bottlenecks of in-silico design of new crystalline semiconducting materials [80–82]. Indeed, the crystal packing structure is essential for the theoretical evaluation of charge mobility, but up to now it is usually taken from experimental measurement,

narrowing the applicability of computations to molecules for which the crystal structure has already been determined. Besides this fundamental problem, another challenge in the field of computer-aided material science is that there is currently an active debate about the most appropriate theory that could take into account the processes taking place in OSC-based devices (see part II for an extensive discussion). Moreover, molecular packing in thin film devices can be different from bulk, being strongly dependent on the substrate where it is deposited on.

Despite these drawbacks, some successful theoretical designs of new semiconductors have been reported, where rational design techniques and computational chemistry methods guided the synthesis of:

- liquid crystal molecules with enhanced columnar organization and optimized intermolecular couplings [83];

- polycarbazole derivative for organic photovoltaic applications by first-principles screening of prototypical oligomers [84];

- polymers based on diketopyrrolopyrrole derivative [85];

- molecular semiconductors based on dinaphthothienothiophene derivatives [61].

In particular, the last example involved a theoretical study started after the experimental report [59] of a new molecule showing good hole mobility along with excellent air-stability (DNTT, fig. 1.13). Combining quantum and molecular mechanics, Sokolov et al. [61, 86], screened possible derivatives of DNTT (molecule "1" in fig. 1.13), focusing their attention on the ones showing low reorganization energies, which following Marcus approach are expected to yield better mobilities. On the basis of their study, they decided to further investigate only DATT (Dianthra[2,3-b:2',3'-f]thieno[3,2-b]thiophene, molecule "2" in fig. 1.13), which showed the highest transfer integral together with the lowest reorganization energy among the molecules under investigation, predicting a mobility twice as large as the

one of DNTT. The DATT was subsequently synthesized and incorporated in a transistor, recording experimental mobilities higher than $10\,cm^2V^{-1}s^{-1}$ [61].
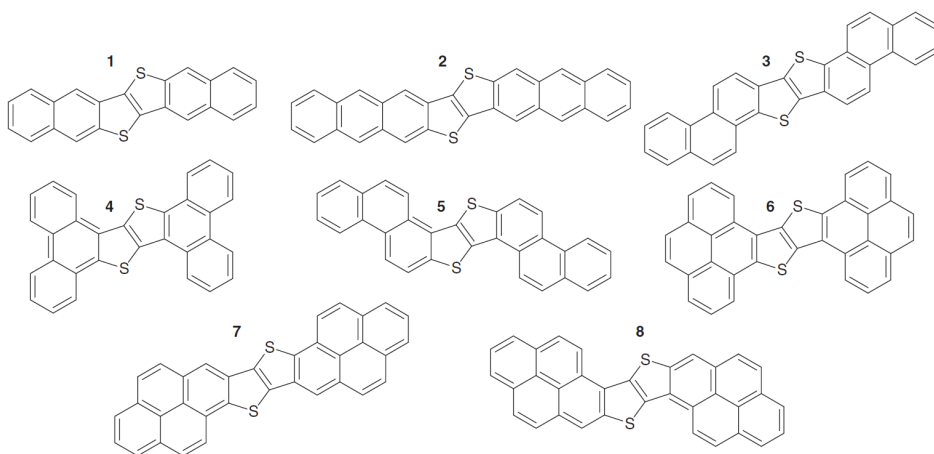
Figure 1.13. The structures of seven molecules studied in [61] (2-8) derived from the parent dinaphtho[2,3-b:2',3'-f]thieno[3,2-b]thiophene (1). Reproduced from ref. 61.

The abovementioned examples indicate that theoretical design before the synthesis is very promising; however it must be noted that all of them involved derivatives of an already experimentally characterized molecule, so that the "new" crystalline structure could be guessed from the one of the precursor. In other words, the crystal structure should be known, since the solid-state prediction from molecular structure is still a challenge.

In this respect, apart from theoretical design of derivatives showing better properties than their precursor, another very interesting approach [87] would be the screening of potential material candidates contained in large data sets (such as the CSD [88]), for which the crystal structure is already known. A tool able to perform such a prediction would be highly beneficial, considering that substantial experimental effort is required to grow ultra-pure single-crystalline samples for OFET measurements, while the

crystalline structure of the material is typically known shortly after the initial synthesis.

This would allow the selection of the most promising candidates, so that, in collaboration with synthetic chemists to assess synthetic viability, it would be possible to quickly identify the best materials, potentially reducing expensive and time-consuming experimental characterizations.

In light of all these considerations, in this thesis we focus on the comparison of five among the most popular models for the study of CT in organic semiconductors, highlighting their strengths and their shortcomings. Moreover, we discuss some approximate methodologies, developed in our group, to alleviate the computational burden of the models under investigation, making them more suitable for the analysis of a large number of molecules in a short amount of time.

Part II

THEORETICAL MODELS

Chapter 2

Overview

Charge transfer (CT) reactions are of widespread importance in many fields, such as chemistry, biochemistry and material physics. Concerning the biochemical processes, respiration, photosynthesis, and many others mainly rely on electron transfer between cofactors in proteins. Likewise, in the field of organic semiconductors, the subject of this thesis, the processes taking place in the devices are mainly CT reactions.

Franck and Libby were the first to realize that CT rates are regulated by the nuclear motions of the two molecules exchanging an electron and of the surrounding environment [89]. They applied the Franck-Condon (FC) principle to thermal CT reactions in solutions, obtaining a direct proportionality between CT rates and the square of the overlap between the vibrational states of the initial and final electronic states, that is, the FC factors. The pioneering studies of Lax and Kubo [90, 91] on radiationless transitions in condensed phase, and of Marcus [92–95], who first quantitatively described the solvent effects in CT processes in solutions, provided powerful theoretical means for computing FC factors, laying the foundations for modeling CT reactions in condensed phases.

Marcus work provided all the basic concepts to model CT processes in a very straightforward way. The price of this simplicity is however the base

of its limitations: it is a one-dimensional model in which nuclear vibrations are treated classically and without considering frequency changes between initial and final state. For this reason, Marcus model is rigorously applicable only at high temperature, where all vibrations are fully excited and tunneling effects (not included) play a minor role.

One of the most popular models going beyond classical Marcus equation is Fermi Golden Rule (FGR) [96], a full quantum mechanical approach obtained from the first order time-dependent perturbation theory. It was originally derived by Dirac [97] but significantly improved by Lax and Kubo [90, 91, 98] with the generating function approach, which allows for the inclusion of all the normal modes in the computations. Unfortunately, the FGR seems to fail in describing ultrafast processes [56, 99, 100] leading to strong overestimations of the transition rates.

A significant improvement to FGR, still in the framework of hopping process, is the Second Order Cumulant approach (SOC), developed in our group, based on the second-order cumulant expansion of the time dependent reduced density matrix [99]. Even if the cumulant expansion is a well-known technique [101–104], rather few applications to realistic systems have appeared in the literature [56, 99, 105, 106]. We will see that the SOC approach is useful in handling ultra-fast transitions because of the time-dependent nature of the transition rate; furthermore, it obtains kinetic rates approaching a constant value, namely the FGR prediction, for long times.

All the models previously discussed are hopping models, i.e. they predict the loss of coherence after each step of charge transport. However, in some systems, such as highly ordered materials, coherent charge transfer can occur, and hopping is no longer adequate. Instead, coherent quantum dynamics should be used, where the nuclear degrees of freedom can be propagated using classical equation of motion (semiclassical approaches, like Ehrenfest or surface hopping), or they can be included in the time-dependent Schrödinger equation describing both electronic and vibrational

states at the quantum level. We will focus on this latter approach, describing systems characterized by several electronic states with vibronic couplings to harmonic modes. In particular we will propose a strategy to solve one of the main difficulties of this method: the hugely high number of vibronic states to be considered to properly describe the effects of nuclear displacements upon ET. Our idea is based on the partitioning of the entire Hilbert space in a set of subspaces of significantly reduced size, where the convergence of computations is checked by iteratively increasing the number of subspaces.

It is clear that those models can be applied only in the framework in which they were developed, i.e. incoherent rather than coherent (band theory) charge transport, while quantum dynamics is a computationally expensive approach. However, it would be useful to have a model going beyond this distinction, applicable at a rather low computational cost. In this respect, Fratini et al. have developed the Transient Localization Theory (TLT) [107, 108], a model based on the idea that the unavoidable disorder in real crystals leads to a "transient localization" which would severely slow down carrier mobility; however, time fluctuations of crystal disorder may still activate charge diffusion. That theory should go beyond both the band approach (since it contains quantum localization correction) and hopping (since it does not predict the loss of coherence after each hop) [54].

In the following chapters we will briefly describe these five models, while their application to the description of charge transfer in organic semiconductors and in DNA oligomers will be shown in part III and IV, respectively.

Chapter 3

Hopping models

3.1 Marcus classical description of the electron transfer processes

In Marcus theory, the potential energy profiles of the two electronic states (a and b) exchanging an electron are expressed in one dimension and in the harmonic approximation, as two parabolas with the same curvature $K = M\omega^2$:

$$V_a = \frac{K(x - x_a)^2}{2} + E_a \qquad\qquad V_b = \frac{K(x - x_b)^2}{2} + E_b. \qquad (3.1)$$

For the sake of simplicity, in the following we assume that the zero of the reaction coordinate x is the equilibrium position of the state a ($x_a = 0$) and the zero of the energy is the equilibrium energy of the state b ($E_b = 0$) (fig. 3.1).

One of the simplest derivations of the Marcus equation considers the CT reaction as a radiationless transition between 2 electronic states, resorting to the Landau-Zener formula [96, 109–111] and assuming that there is no entropic nor volume changes (i.e. $\Delta E = \Delta G$).

The interested reader is referred to appendix A for a complete treatment,

here we will give the final formula obtained by Marcus:

$$k = \frac{|V_{ab}|^2}{\hbar} \sqrt{\frac{\pi}{\lambda k_{\mathrm{B}} T}} \exp \frac{(\Delta G^0 + \lambda)^2}{4\lambda k_{\mathrm{B}} T},$$

(3.2)

where ΔG^0 is the free energy change of the CT reaction and λ is the reorganization energy, i.e. the energy spent from the state a to reach the nuclear configuration of the state b without actually changing electronic state, see fig. 3.1. V_{ab} is the coupling between the initial and final CT states. For all the theoretical models discussed in this thesis, the V_{ab} are evaluated as [112]:

$$V_{ab} = \langle \phi_a^0 | \mathcal{F} | \phi_b^0 \rangle,$$

(3.3)

where ϕ_a^0 and ϕ_b^0 are the localized HOMOs of states a and b, respectively, and $\mathcal{F}$ is the Fock operator of the system. The suffix 0 indicates that the orbitals are unperturbed, i.e. computed for the isolated molecule. More details on this procedure can be found in chapters 5 and 8.

In the cases considered throughout this thesis, i.e. CT between two equal molecules, the net ΔG change is zero, so eq. 3.2 becomes:

$$k = \frac{|V_{ab}|^2}{\hbar} \sqrt{\frac{\pi}{\lambda k_{\mathrm{B}} T}} \exp \left[-\frac{\lambda}{4 k_{\mathrm{B}} T} \right].$$

(3.4)

The reorganization energy (λ)[92][96] consists of two components: one (λ_{int}) coming from the nuclear degrees of freedom of the two molecules between which the CT takes place, while the other (λ_{out}) comes from changes in the environment (usually the solvent),

$$\lambda = \lambda_{int} + \lambda_{out}.$$

(3.5)

The former component is the sum of the contributions of each intramolecular vibrational degree of freedom v_l:

$$\lambda_{int} = \sum_{v_l} \lambda_{int,v_l} = \frac{1}{2} \sum_{v_l} \omega_{v_l}^2 (\Delta q_{v_l})^2$$

(3.6)
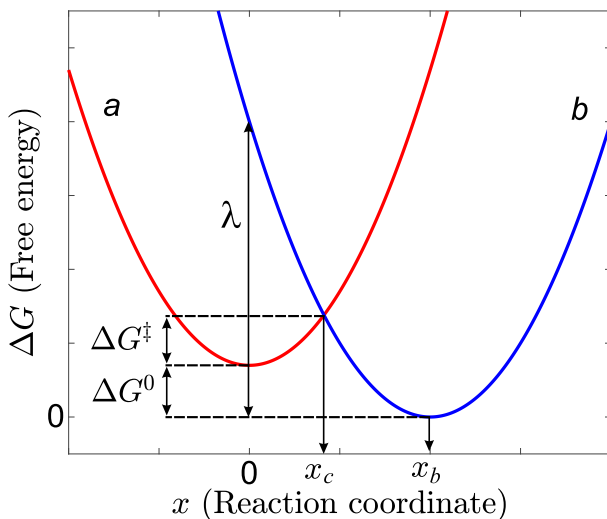
Figure 3.1. Nuclear motion accompanying electron transfer. Curves a and b represent the change in free energy with nuclear coordinate x for the states between which CT occurs. x_c is the coordinate where the two potential curves intersect.

where the contribution of the v_l-th normal mode to the reorganization energy is given in terms of its vibrational frequency ω_l and the change in equilibrium positions between the reactants and the products is $\Delta q_{v_l} = q_{v_l,b} - q_{v_l,a}$.

λ_{out} can be evaluated using a model in which reactants and products are modeled as spheres and the environment (usually the solvent) as a dielectric continuum:

$$\lambda_{out} = \frac{e^2}{4\pi\epsilon_0} \left[\frac{1}{2r_1} + \frac{1}{2r_2} - \frac{1}{r_1+r_2} \right] \left[\frac{1}{D_\infty} - \frac{1}{D_0} \right], \qquad (3.7)$$

where r_1 and r_2 are respectively the radii of the donor and acceptor molecule in the Marcus two spheres model, while D_∞ and D_0 are the optical dielectric constant (i.e. the square of the refractive index) and static dielectric constants of the medium; e is the electron charge and ϵ_0 the vacuum permittivity. The difference in the inverse dielectric constants is due to the

fact that nuclear degrees of freedom cannot readjust instantaneously to the motion of the electrons and thus contribute to the barrier's height.

It is interesting to point out that, in molecular organic semiconductors, where the environment is not represented by the solvent but by the crystalline structure, the λ_{out} contribution is negligible. Indeed, computations carried out by using a QM/MM approach with a polarizable force field for naphthalene in its molecular crystal structure showed that the intermolecular reorganization energy is of the order of a few meV [113]; further studies for acenes yield intermolecular reorganization energies typically lower than 0.2 kcal/mol [114], much smaller than the intramolecular one. Experimentally, it has been recently shown that the reorganization energy of rubrene is almost independent from the molecular packing structure [115], once again indicating that the intermolecular reorganization energy, the only part that depends on the molecular arrangement, is a minor contributor to the total λ.
In light of these considerations, throughout this thesis we will consider only the intramolecular part of the reorganization energy λ_{int}.

3.2   Fermi Golden Rule

Marcus equation is classical, i.e. it is valid only at temperatures high enough that all the vibrations are fully excited. A more accurate model, which allows for the inclusion of all the vibrational normal modes in the computation and thus valid at every temperature, is the Fermi Golden Rule (FGR). FGR is a simple formula to evaluate the kinetic rate constant for a transition between two electronic states a and b, each one with a manifold of vibrational states v_a and v_b.

Interestingly, even if it is named after Fermi, the formula was actually derived by Dirac [97]; the name is related to the fact that, because of its importance, Fermi named it "Golden Rule number 2" (the Golden Rule 1 describes a transition involving an intermediate state $|c\rangle$) [116].

We start considering a system described by a generic Hamiltonian $\mathcal{H}$ where two electronic states $|a\rangle$ and $|b\rangle$ are coupled to each other by a generic operator $\mathcal{V}$.

$$\mathcal{H} = |a\rangle\mathcal{H}_a\langle a| + |b\rangle\mathcal{H}_b\langle b| + |a\rangle\mathcal{V}_{ab}\langle b| + c.c. = \mathcal{H}_0 + \mathcal{V}. \qquad (3.8)$$

If $\mathcal{V}$ is time independent, the system will end in final states having the same energy of the initial state, while, if $\mathcal{V}$ oscillates in time with angular frequency ω the transition occurs into states with energies differing by $\hbar\omega$ from the energy of the initial state.

In both cases, the probability of the transition from $|a\rangle$ to $|b\rangle$, at the first order of the perturbation theory, is

$$k_{b \leftarrow a} = \left(\frac{2\pi}{\hbar}\right)|V_{ab}|^2 F(\Delta E, T), \qquad (3.9)$$

where $|V_{ab}|$ is the electronic coupling (also called transfer integral) between the two electronic states $|V_{ab}| = \langle a|\mathcal{V}|b\rangle$ and $F(\Delta E, T)$ is the Franck-Condon weighted density of states (FCWD) [96]:

$$F(\Delta E, T) = \frac{1}{Z}\sum_{v_a, v_b} e^{-\beta E_{v_a}} \times |\langle v_a|v_b\rangle|^2 \delta(E_{v_b} - E_{v_a} - \Delta E). \qquad (3.10)$$

Here $\Delta E = E_a - E_b$, $\langle v_a|v_b\rangle$ is the Franck-Condon (FC) factor (i.e. the overlap between two vibrational levels), Z is the vibrational partition function of the initial electronic state, and the sum runs over all vibrational states of $|a\rangle$ and $|b\rangle$. The evaluation of F by this infinite summations poses problems that can be avoided by using the generating function (GF) approach [90, 98], which takes advantage of the integral representation of the Dirac delta function. We use Duschinsky's normal mode transformation, which expresses the normal modes $\mathbf{Q}_a$ of a molecules in its electronic state $|a\rangle$ as a roto-translation of the modes $\mathbf{Q}_b$ in another state $|b\rangle$ [117],

$$\mathbf{Q}_a = \mathbf{J}\mathbf{Q}_b + \mathbf{K}, \qquad (3.11)$$

F can be evaluated in harmonic approximation including the whole sets of nuclear coordinates in computations [96, 118–121], as explained into details in appendix B.

3.3   Second Order Cumulant approach

The Fermi Golden Rule (FGR) has intrinsic limitations: it is based on the lowest order of time dependent perturbation theory, in which the upper limit of time integration is set to infinity. This is physically well-sound for processes with sufficiently long transition times, where the population decay of an initial state can be well represented by a single exponential function. In those cases an estimate of the quantum dynamical behaviour of the system in terms of a global reaction rate is adequate, but this approximation should be used with caution with ultrafast processes. A more suitable approach relies on the second-order cumulant expansion of the density matrix of the system. The cumulant approach [101–104, 122, 123] recently discussed and successfully applied to spin-boson and linear vibronic coupling Hamiltonian model [105, 106, 124] allows to take into account the change of the reaction rate with time, describing the population $P(t)$ of the state of interest with an equation of the form:

$$\frac{\mathrm{d}P(t)}{\mathrm{d}t} = k(t)P(t). \tag{3.12}$$

We use here the same Hamiltonian of the previous section, i.e.

$$\mathcal{H} = |a\rangle\mathcal{H}_a\langle a| + |b\rangle\mathcal{H}_b\langle b| + |a\rangle V_{ab}\langle b| + c.c. = \mathcal{H}_0 + \mathcal{V}, \tag{3.13}$$

modeling the electronic states in harmonic approximation.

The coupling operator $\mathcal{V}$ is usually assumed to have a constant value [96], but in general it is a function of the vibrational coordinates of the system. In this respect, a popular approximation assumes the coupling operator to be a linear function of the nuclear coordinates (linear vibronic model [125, 126]). The interested reader is referred to ref. [99] for an extensive discussion handling both cases.

Here we will describe the dynamic of the system using the density matrix $\rho(t)$ formalism, since it is more common in the literature [101–104, 122]. Moreover, we take advantage of the fact that the total Hamiltonian $\mathcal{H}$

can be splitted in two parts (eq. 3.13), where $\mathcal{H}_0$ is time independent and $\mathcal{V}$ couples two electronic states. In this case, $\mathcal{V}$ can be written in the interaction representation as

$$V_I(t) = e^{[+(\mathrm{i}/\hbar)\mathcal{H}_0(t)]}\mathcal{V}e^{[-(\mathrm{i}/\hbar)\mathcal{H}_0(t)]} \tag{3.14}$$

Using this particular form of V_I, the time evolution of $\rho_I(t)$ is given by:

$$\rho_I(t) = \mathcal{T}\exp\left(-\frac{\mathrm{i}}{\hbar}\int_0^t V_I^\times(\tau)\mathrm{d}\tau\right)\rho_I(0) \tag{3.15}$$

where $\mathcal{T}$ is a time ordering operator and $\rho_I(0)$ is the density matrix at time $t = 0$, specifying the initial conditions of the system. The operator $V_I^\times(\tau)$ is defined by its action on a generic operator $\mathcal{O}$ as $V_I^\times(\tau)\mathcal{O} = [V_I(\tau), \mathcal{O}]$ [101, 127].

The population of the initial electronic state $|a\rangle$ is formally given by:

$$
\begin{aligned}
P_a(t) &= \mathrm{Re}\,\mathrm{Tr}\langle a|\mathcal{T}\exp\left(-\frac{\mathrm{i}}{\hbar}\int_0^t V_I^\times(\tau)\mathrm{d}\tau\right)\rho_I(0)|a\rangle = \\
&= \mathrm{Re}\left\langle \mathcal{T}\exp\left(-\frac{i}{\hbar}\int_0^t V_I^\times(\tau)\mathrm{d}\tau\right)\right\rangle
\end{aligned}
\tag{3.16}
$$

where the trace is taken over the vibrational degrees of freedom and $\langle X\rangle = \mathrm{Tr}\langle a|X\rho_I(0)|a\rangle$. On the right side of this equation there is a time-ordered exponential, so we can resort to the cumulant expansion applied to a time-ordered exponential operator $W(\tau)$, obtaining the Magnus expansion [102, 103, 128], defined as

$$\mathcal{T}\exp\left[\lambda\int_{t_0}^t \mathrm{d}\tau W(\tau)\right] \equiv \exp\left[\sum_{n=1}^\infty \frac{1}{n!}\lambda^n Y_n(t, t0)\right] \tag{3.17}$$

where Y_n is the n-th order cumulant, defined as:

$$Y_1(t, t_0) = \int_{t_0}^t \mathrm{d}\tau W(\tau) \tag{3.18}$$

$$Y_2(t, t_0) = \int_{t_0}^t \mathrm{d}\tau_2 \int_{t_0}^{\tau 2} \mathrm{d}\tau_1 [W(\tau_2), W(\tau_1)] \tag{3.19}$$

$$Y_3(t, t_0) = \int_{t_0}^{t} \mathrm{d}\tau_3 \int_{t_0}^{\tau_3} \mathrm{d}\tau_2 \int_{t_0}^{\tau_2} \mathrm{d}\tau_1 \{ [W(\tau_3), [W(\tau_2), W(\tau_1)]] +$$
$$+ [[W(\tau_3), W(\tau_2)], W(\tau_1)] \} \tag{3.20}$$

and so on.

Using this expansion for our Hamiltonian, we make the ansatz:

$$P_a(t) = \left\langle \mathcal{T} \exp\left(-\frac{\mathrm{i}}{\hbar} \int_0^t V_I^\times(\tau) \mathrm{d}\tau \right) \right\rangle \equiv \exp(K(t)) \tag{3.21}$$

Applying the Magnus expansion to this expression, it is possible to show [99] that all odd-order cumulant terms, such as $K_1(t)$, $K_3(t)$, etc. are zero, because with the $\mathcal{V}$ used here we get that $\langle a | V_I{}^n | a \rangle = 0$ when n is odd. Therefore, the first contribution is given by the second-order cumulant:

$$K_2(t) = -2\hbar^{-2} \mathrm{Re} \int_0^t \mathrm{d}\tau_1 \int_0^{\tau_1} \langle i | [V_I(\tau_1), [V_I(\tau_2), \rho(0)]] | i \rangle \mathrm{d}\tau_2. \tag{3.22}$$

This is a rather general expression, but the actual form depends on V_I and the initial conditions of the system ρ_0.

For fast hole transfer, it is physically more sound to consider the thermally equilibrated ground state of the neutral molecule which instantaneously releases an electron. In this case, the initial density for hole transfer is given by the Boltzmann equilibrium distribution of the ground state $|g\rangle$ projected onto the excited (cationic) state $|a\rangle$:

$$\rho_{\mathrm{neq}}(0) = Z_g^{-1} |a\rangle \mathrm{e}^{-\beta \mathcal{H}_g} \langle a|. \tag{3.23}$$

where $\mathcal{H}_g$ is the vibrational Hamiltonian of the ground (neutral) molecule and Z_g its corresponding vibrational partition function. Under this assumptions, making explicit the interaction picture of operator V_{ab}, eq. 3.22 becomes:

$$K_{2,\mathrm{neq}}(t) = \frac{-2}{\hbar^2 Z_g} \mathrm{Re} \int_0^t \mathrm{d}\tau_1 \int_0^{\tau_1} \mathrm{Tr} \left[\mathrm{e}^{-\beta \mathcal{H}_g} \mathrm{e}^{\mathrm{i}\mathcal{H}_a \tau_2} V_{ab} \mathrm{e}^{-\mathrm{i}\mathcal{H}_b(\tau_2 - \tau_1)} V_{ba} \mathrm{e}^{-\mathrm{i}\mathcal{H}_a \tau_1} \right] \mathrm{d}\tau_2. \tag{3.24}$$

On the other hand, if we assume the equilibrium population of the unperturbed initial state ($\rho_{\text{eq}}(0) = Z_a^{-1}|a\rangle e^{-\beta\mathcal{H}_a}\langle a|$), eq. 3.22 becomes:

$$K_{2,\text{eq}}(t) = \frac{-2}{\hbar^2 Z_a}\text{Re}\int_0^t d\tau_1\int_0^{\tau_1}\text{Tr}\left[e^{i\mathcal{H}_a(\tau_2+i\beta)}V_{ab}e^{-i\mathcal{H}_b(\tau_2-\tau_1)}V_{ba}e^{-i\mathcal{H}_a\tau_1}\right]d\tau_2.$$
(3.25)

It is important to point out that a better insight into the physical process can be gained resorting to the differential equation expressing the variation of the electronic population (obtained differentiating eq. 3.21):

$$\frac{dP_a(t)}{dt} = k_{\text{SOC}}(t)P_a(t)$$
(3.26)

In this case, eq.s 3.24 and 3.25 become respectively

$$k_{\text{SOC,neq}}(t) = \frac{-2}{\hbar^2 Z_g}\text{Re}\int_0^t\text{Tr}\left[e^{-\beta\mathcal{H}_g}e^{i\mathcal{H}_a\tau}V_{ab}e^{-i\mathcal{H}_b(\tau-t)}V_{ba}e^{-i\mathcal{H}_a t}\right]d\tau,$$
(3.27)

and

$$k_{\text{SOC,eq}}(t) = \frac{-2}{\hbar^2 Z_a}\text{Re}\int_0^{\tau_1}\text{Tr}\left[e^{i\mathcal{H}_a(\tau+i\beta)}V_{ab}e^{-i\mathcal{H}_b(\tau-t)}V_{ba}e^{-i\mathcal{H}_a t}\right]d\tau. \quad (3.28)$$

This quantity k_{SOC} can be interpreted as the time dependent rate of the electronic transition, so it can be compared with transition rates obtained with different approaches, such as Marcus formula or FGR. In particular, it is possible to show that SOC rates reach a constant value, namely the FGR prediction, in the case of very long times [56, 99]:

$$\lim_{t\to\infty} k_{\text{SOC}}(t) = \text{constant} = k_{\text{FGR}}.$$
(3.29)

3.4 Evaluation of anisotropic charge mobility in the hopping framework

In general the current flow in a material is driven by the electric field applied and by the gradient in the charge concentration, leading to two contribution to the overall current: the drift current and the diffusion current,

respectively. However, for low electric fields, the diffusive process becomes dominant, so that charge transport can be described as a diffusion where the carriers move among adjacent molecules according to the charge transfer rates that apply in the absence of an external electric field. Under these assumptions, the mobility can be evaluated resorting to Einstein's formula:

$$\mu = \frac{eD}{k_{\mathrm{B}}T},$$

(3.30)

where e is the elementary charge, k_{B} is the Boltzmann constant, T is the absolute temperature and D is the diffusion coefficient, defined as:

$$D = \frac{1}{2n_s} \lim_{t \to \infty} \frac{\Delta X^2}{t},$$

(3.31)

where n_s is the dimensionality of the system and ΔX^2 is the mean-square displacement evaluated at $t \to \infty$, i.e. for long times, when the diffusion regime is established [107].

For an isotropic system, eq. 3.31 can be approximated as [129–131]

$$D = \frac{1}{2n_s} \sum_{i=1}^{N} d_i^2 k_i p_i,$$

(3.32)

where the sum runs over all neighbouring molecules N. Here, d_i is the hopping distance, k_i the relative rate constant, and p_i the hopping probability $(p_i = k_i / \sum_j^N k_j)$. It is easy to see that, if we are interested on the mobility along a single hopping pathway i, eq. 3.30 simplifies to:

$$\mu_i = \frac{ed_i^2 k_i}{2k_{\mathrm{B}}T}$$

(3.33)

Usually, this quantity is considered a poor descriptor of the actual electronic properties of the material, since it focuses on a single migration channel, while in real crystals there are multiple pathways along which the charge can diffuse. With this in mind, a better descriptor is the anisotropic mobility, i.e. the variation of the mobility according to the orientation of the
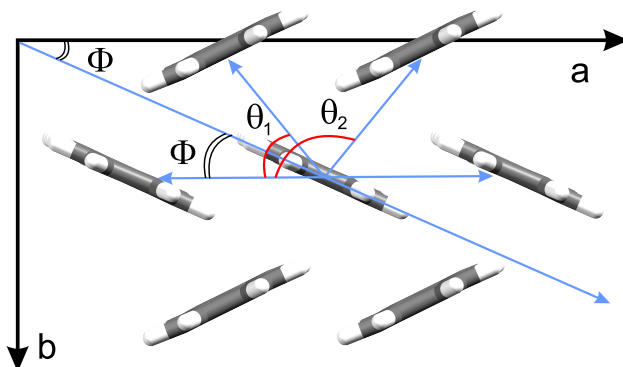
Figure 3.2. Scheme of a typical OSCs crystal. *a* and *b* identify any two crystallographic axes.

conductive channel relative to the crystallographic axes, when taking into account all possible charge migration pathways.

In this respect, assuming that there is no correlation between hopping events and that charge motion is a homogenous random walk, the mobility along a given conducting direction on a specific plane in the organic crystal can be computed as [131, 132]:

$$\mu(\Phi) = \frac{e}{2k_{\mathrm{B}}T} \sum_i k_i d_i^2 P_i \cos^2 \gamma_i \cos^2 (\theta_i - \Phi). \qquad (3.34)$$

Here Φ is the angle formed by the transistor channel and the reference axis, γ_i is the angle between the i-th hopping path and the plane of interest and θ_i is the angle of the projected i-th hopping path of different dimer types relative to the reference axis. With this construction (see fig. 3.2 for a schematic representation) the angles between the hopping paths and the conducting channel are $(\theta_i - \Phi)$, while $P_i \cos^2 \gamma_i \cos^2 (\theta_i - \Phi)$ describes the hopping probability of various dimer types relative to the specific transistor channel.

It is important to notice that (see fig. 3.3), in most instances, π-conjugated molecules have a crystal structure with a high-mobility plane, while the

Figure 3.3.   Pictorial representation highlighting the presence of high-mobility layers in organic semiconductors.

mobility perpendicular to this plane is 1-2 orders of magnitude smaller [54, 132, 133]. Therefore, in this thesis, we focus on the 2D-transport within the stacked organic layer of interest, evaluating the anisotropic mobility with respect to this layer, so that γ_i is always 0.
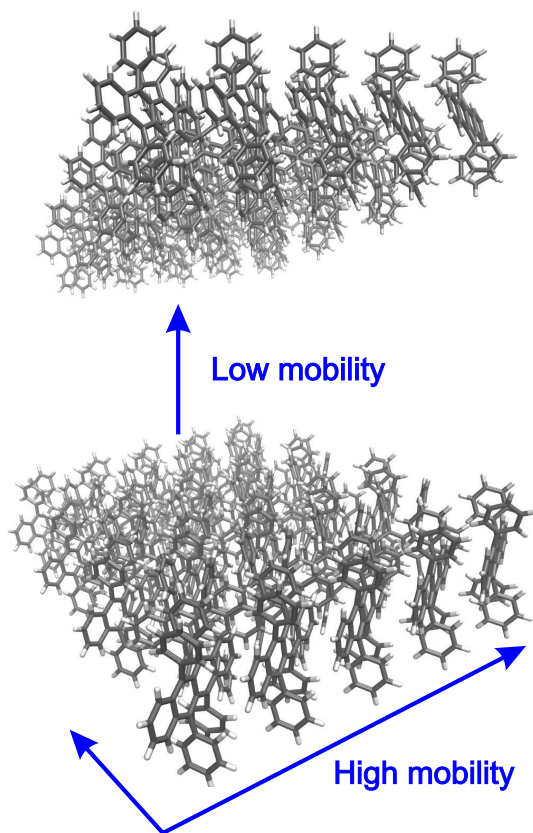
Chapter 4

Quantum Dynamics approach

All the models described in the previous chapter are hopping models, where, by definition, coherence and delocalization effects are neglected. However, hopping is no longer adequate for some systems, such as highly ordered materials, where coherent charge transfer can occur. In these cases, coherent quantum dynamics methods can be used, either semiclassical ones, where the electronic wavefunction is propagated with the time-dependent Schrödinger equation while the nuclear degrees of freedom follow classical trajectories, or full quantum mechanic methods, where both electronic and nuclear degrees of freedom are treated at the quantum level.

Here we will focus on a full quantum approach, based on the numerical solution of the time-dependent Schrödinger equation for systems characterized by several electronic states with vibronic couplings to harmonic modes.

Let us consider N_{el} weakly interacting molecular sites constituting a supramolecular system where a charge has been injected. Each molecular unit of this system is in its neutral $|i_N\rangle$ or charged $|i_C\rangle$ state, so we have N_{el} diabatic states, each of them corresponding to the charge fully localized on one molecular site. If the charge is localized on the j-th unit, the corresponding electronic state $|j\rangle$ can be written (under the assumption that the electronic coupling is weak) as the direct product of the eigenstate of

non-interacting molecular units,

$$|j\rangle = |j_C\rangle \prod_{i \neq j}^{N_{el}} |i_N\rangle, \tag{4.1}$$

and the electronic Hamiltonian operator of the isolated i-th molecular units in its redox state $X = C, N$ (i.e. charged or neutral state) is:

$$\mathcal{H}_{iX}^{(el)}|i_X\rangle = U_{iX}(\mathbf{Q}_{iX})|i_X\rangle, \quad X = C, N; \quad i = 1, 2, \ldots, N_{el}. \tag{4.2}$$

Here U_{iX} is the electronic energy and $\mathbf{Q}_{iX}$ are the normal modes of the i-th molecular units.

In the following we will work in harmonic approximation, i.e.

$$U_{iX} = E_{iX}^0 + \frac{1}{2}\mathbf{Q}_{iX}^\dagger \boldsymbol{\omega}_{iX}^2 \mathbf{Q}_{iX} \tag{4.3}$$

where E_{iX}^0 is the electronic energy at the equilibrium geometry, while $\boldsymbol{\omega}_{iX}$ is the matrix containing the vibrational frequencies of the normal modes of the i-th molecular unit in its X state ($X = C, N$).

The whole Hamiltonian operator is [134]:

$$\mathcal{H} = \sum_{l,m}^{N_{el}} |l\rangle\langle l|\mathcal{T}_N + \mathcal{H}_{el}|m\rangle\langle m|, \tag{4.4}$$

where all the nuclear and electronic coordinates of the whole system are included in $\mathcal{T}_N$ and $\mathcal{H}_{el}$.

The total time-dependent wavefunction can be expanded over a set of (time independent) Born-Oppenheimer product wavefunctions with time-dependent combination coefficients:

$$\Psi(t) = \sum_{l,\bar{v}_l} \mathbf{C}_{\bar{v}_l}^{(l)}(t)|l, \bar{v}_l\rangle. \tag{4.5}$$

Here the vibrational basis function $|\bar{v}_l\rangle$ for the l-th electronic states can be written (eq. 4.1) as the direct product of the vibrational states of each

molecular unit and the expansion coefficients are determined by solving the time-dependent Schrödinger equation,

$$
i\hbar
\begin{pmatrix}
\dot{\mathbf{C}}_{\bar{v}_1}^{(1)} \\
\dots \\
\dots \\
\dot{\mathbf{C}}_{\bar{v}_{N_{\text{el}}}}^{(N_{\text{el}})}
\end{pmatrix}
=
\begin{pmatrix}
\mathbf{H}_{11} & \mathbf{H}_{12} & \dots & \dots & \mathbf{H}_{1N_{\text{el}}} \\
\dots & \dots & \dots & \dots & \dots \\
\dots & \dots & \dots & \dots & \dots \\
\mathbf{H}_{N_{\text{el}}1}^{\dagger} & \mathbf{H}_{N_{\text{el}}2}^{\dagger} & \dots & \dots & \mathbf{H}_{N_{\text{el}}N_{\text{el}}}
\end{pmatrix}
\begin{pmatrix}
\mathbf{C}_{\bar{v}_1}^{(1)} \\
\dots \\
\dots \\
\mathbf{C}_{\bar{v}_{N_{\text{el}}}}^{(N_{\text{el}})}
\end{pmatrix},
\tag{4.6}
$$

with initial conditions specifying the initial state of the system.

In eq. (4.6), each block $\mathbf{H}_{11}$, $\mathbf{H}_{12}$, etc. of the Hamiltonian matrix is a matrix itself, with a size depending on the vibrational basis sets chosen for each electronic state l and m. The blocks composing the Hamiltonian matrix fall in two categories: diagonal blocks $\mathbf{H}_{ll}$, containing the energies of the l-th electronic state, and off-diagonal blocks $\mathbf{H}_{lm}$, providing the coupling between two electronic states $|l\rangle$ and $|m\rangle$.

$\mathbf{H}_{ll}$ are diagonal matrices, whose elements are the eigen-energies of multidimensional harmonic oscillators. By denoting with $n_{i,l,v_l}^{(\alpha)}$ the vibrational quantum number of the α-th normal mode of the i-th molecular unit in the l, v_l-th vibronic state, the diagonal elements are:

$$
H_{l,v_l,l,v_l} = \sum_{i=1}^{N_{\text{el}}} \left[\sum_{\alpha} \hbar n_{i,l,v_l}^{(\alpha)} \omega_{i,l}^{(\alpha)} \right] + E_l,
\tag{4.7}
$$

where E_l is the electronic energy of the l-th electronic state; the index i runs over all the molecular units and α over the normal modes of the i-th unit. It is worth noting that in eq. 4.7 the zero point energy contribution is not explicitly indicated since it is included in the electronic energy term.

After integration over the electronic coordinates, neglecting the weak dependence of the electronic couplings on the nuclear coordinates, the coupling terms between the vibronic states of $|l\rangle$ and $|m\rangle$ are:

$$
H_{l,l_i,\bar{v}_{l_i},m_j,\bar{v}_{m_j} \to m,l_i',\bar{v}_{l_i'},m_j',\bar{v}_{m_j'}} = H_{lm} \cdot \langle \bar{v}_{l_i} | \bar{v}_{l_i'} \rangle \langle \bar{v}_{m_j} | \bar{v}_{m_j'} \rangle,
\tag{4.8}
$$

where $H_{lm} = \langle l | \mathcal{H}^{(\text{el})} | m \rangle$ is the coupling term between the two electronic states $|l\rangle$ and $|m\rangle$, while $\langle \bar{v}_{l_i} | \bar{v}_{l'_i} \rangle$ and $\langle \bar{v}_{m_j} | \bar{v}_{m'_j} \rangle$ are the multidimensional Franck-Condon integrals over the normal modes of the two molecular units (i and j) which change electronic state, from l to l' and from m to m', respectively.

In conclusion, the quantities needed to build up the Hamiltonian matrix which determines the time evolution of the system are:

- the relative energies of the N_{el} vibronic ground states (including the zero point energy contribution);

- the electronic coupling terms;

- the normal modes of each electronic state, which, according to the above assumptions, can be evaluated separately for each molecular component;

- the Franck-Condon integrals.

Once the Hamiltonian matrix is built, time-evolution of the system can be followed resorting to Lanczos method (see Appendix C).

One of the main problems in this approach is the selection of the vibrational states to be used in the time evolution. Indeed, each molecule possesses $3N_A - 6$ normal modes (N_A being the number of atoms), and, even for small molecules and restricting ourselves to few simultaneously excited vibrations, each with a low quantum number, the Hamiltonian matrix quickly becomes too big for the computations, even with modern computational resources.

To gain quantitative insight in this problem, we here report a simple formula [135] to evaluate the size S_B of one block of the Hamiltonian matrix:

$$S_B = 1 + \sum_{J=1}^{NC} \binom{NM}{J} \times (NQ)^J, \tag{4.9}$$

where NM is the number of normal modes, NQ their quantum number (assumed to be equal for all the modes) and NC the number of simultaneously excited vibrations. For a very little system, say $NQ = 10$, $NM = 30$ e $NC = 3$, we get $S_B \approx 3 \times 10^6$! It should also be kept in mind that this is only the size of one block of the Hamiltonian matrix, which is formed by N_{el}^2 blocks, N_{el} being the number of electronic states considered.

4.1 A method for pruning basis set

Several strategies to reduce the size of the vibronic basis set have been proposed in the literature [136]. The approach we use here is based on the idea (applied in the field of molecular spectroscopy by Jankowiack [137] and Santoro [138], but used for the first time in quantum dynamics by our group [139]) of partitioning the entire Hilbert space H_s in a set of subspaces which differ in the number of vibrations which are allowed to be simultaneously excited:

$$H_s = \bigcup_c S_c.$$

Here S_c is the space spanned by the states in which only c vibrations are simultaneously excited, with a given maximum quantum number for each of them. Following this idea, the wavefunction of Eq. 4.5 can be rewritten as:

$$\Psi(t) = \sum_l^{N_{el}} \left[\sum_{c=1}^{N} \sum_{i_1 \ldots i_C}^{\binom{N}{c}} \sum_{v_{i_1} \ldots v_{i_c}} C_{v_{i_1} \ldots v_{i_c}}(t) \left| v_{i_1} \ldots v_{i_c} \right\rangle \right] \left| l \right\rangle =$$

$$\sum_l^{N_{el}} \left[C_0^{(l)}(t) \left| 0 \right\rangle + \sum_i^{N} \sum_{v_i} C_{v_i}^{(l)}(t) \left| v_i \right\rangle + \sum_{ij}^{\binom{N}{2}} \sum_{v_i v_j} C_{v_i v_j}^{(l)}(t) \left| v_i v_j \right\rangle + \ldots \right] \left| l \right\rangle, \quad (4.10)$$

where for sake of simplicity we have dropped the index l in the vibrational basis set.

This partition of the Hilbert space is based on the observation that, in molecular systems, the Franck-Condon integrals associated to a specific electronic transition becomes increasingly smaller with a larger number of excited modes. Therefore, since in our methodology the coupling between two vibronic states is directly proportional to the corresponding FC integrals, it is expected that the effect of states with a significant number of excited vibrations on the overall dynamics will only be marginal. This heuristic approach allows for a significant restriction of the active space of the problem and the associated numerical complexity, still retaining the most important features of the dynamical behaviour of the system. Using this strategy, convergence is checked by running several simulations with vibrational subspaces of increasing size, stopping when self-consistency is reached.

The active vibrational modes, i.e. the modes which are allowed to change their quantum number during the transition, are chosen resorting to the affine Duschinsky's transformation, already introduced when deriving FGR formula (eq. 3.11), which we report here for convenience:

$$\mathbf{Q}_l = \mathbf{J}\mathbf{Q}_m + \mathbf{K}. \tag{4.11}$$

Here $\mathbf{Q}_l$ and $\mathbf{Q}_m$ are the normal mode vectors of $|l\rangle$ and $|m\rangle$, $\mathbf{J}$ is the rotation matrix and $\mathbf{K}$ the displacement vector. $\mathbf{J}$ and $\mathbf{K}$ are evaluated starting from the equilibrium geometries and the normal modes of the two electronic states [140–145]. In general, the greater the components of $\mathbf{K}$, the higher are the FC integrals of the corresponding normal modes, so $\mathbf{K}$ plays a major role in determining the value of the effective couplings between vibronic states.

FC integrals are computed using the separated-mode approximation, factorizing the multidimensional FC into the product of one-dimensional integrals [146]. This approximate method, which allows to significantly

reduce the computational cost, takes into account the change in vibrational frequency, but neglects the mode mixing (i.e. the off-diagonal terms of the Duschinsky's matrix $\mathbf{J}$).

4.2   Mobility evaluation

When resorting to quantum dynamics D is once again defined as:

$$D = \frac{\langle \Delta X^2(t) \rangle}{n_s t}, \tag{4.12}$$

where n_s is the spatial dimensionality of the system (e.g. $n_s = 1$ for 1-dimensional transport). The mean squared displacement, $\langle \Delta X^2(t) \rangle$, of the hole wavefunction at time t is defined as [147, 148]:

$$\langle \Delta X^2(t) \rangle = \sum_A (x_A(t) - x_0)^2 p_A(t), \tag{4.13}$$

where $x_A(t)$ denotes the centre of mass of molecule A, x_0 is the initial position of charge carrier at $t = 0$ and $p_A(t)$ is the occupation of molecule A at time t given as $p_A(t) = \sum_{v_a \in A} |c_{v_a}|^2$, c_{v_a} being the combination coefficient of the vibrational state v_a of molecule A. The position of the charge at $t = 0$ is given as $x_0 = \sum_A p_A(t = 0) x_A(t = 0)$. With a slight modification, it is also possible to derive a similar formula for the mobility taking also into account the drift induced by an external electric field [147].

The diffusion constant thus evaluated can be then inserted in the Einstein relation (eq. 3.30) to eventually get the mobility value.

Chapter 5

Transient Localization Theory

Up to now we have assumed the transfer integral to be constant throughout the charge transfer process. However, it is now widely accepted [53, 54, 149, 150] that the transfer integral undergoes large fluctuations because of thermal motions, an effect known as dynamic disorder. This is a manifestation of the non-local electron-phonon coupling, i.e. it is related to the strong modulation of the transfer integral by low frequency molecular phonons. Several models have been proposed accounting for these fluctuations, such as Ehrenfest dynamics [151], modified surface hopping [152], open quantum systems dynamics [153], many-body physics methods [154] relying both on model Hamiltonians [155] and realistic chemical models [139, 147, 148, 156].

In this thesis we focus on the transient localization theory (TLT) [54, 107, 108, 157], which appears to be a very promising approach, since, when applied to several organic semiconductors [54, 107, 157], it has quite accurately predicted their mobility, with a rather low computational cost. Moreover, TLT does not introduce physical assumptions which may not hold for organic semiconductors, such as the loss of coherence after each step (assumed in Marcus and FGR) or a too long mean-free path (assumed in band theory) [54, 107].

This theory starts from the observation that slow thermal intermolecular motions induce a disordered landscape detrimental for charge motion, a factor severely limiting charge mobilities in OSCs. The disorder induces a quantum localization of the total wavefunction at timescales shorter than the period of molecular oscillations, but, since thermal motions are by nature dynamic, charges encounter different disordered landscapes when moving. In this way, quantum interferences are destroyed at longer times and diffusion can ultimately take place.

The Hamiltonian used in the following is the well-known SSH Hamiltonian [149, 158], written as a sum of 3 contributions: the electronic part, the phonon part and their interaction:

$$\mathcal{H} = \mathcal{H}^{\mathrm{el}} + \mathcal{H}^{\mathrm{ph}} + \mathcal{H}^{\mathrm{el-ph}}. \tag{5.1}$$

The former can be written as:

$$\mathcal{H}^{\mathrm{el}} = \sum_i E_i |i\rangle\langle i| + \sum_{i,j \neq i} V_{ij} |i\rangle\langle j|, \tag{5.2}$$

where the basis set is formed by one-electron states localized on site $|i\rangle$ (only one state per site is considered, e.g. the molecular HOMO for hole transport), E_i is the site electronic energy, V_{ij} is the transfer integral and the summation is limited to the nearest neighbour pairs.

The phonon term is:

$$\mathcal{H}^{\mathrm{ph}} = \sum_M \hbar\omega_M \left(-\frac{1}{2}\frac{\partial^2}{\partial \mathbf{Q}_M^2} + \frac{1}{2}\mathbf{Q}_M^2 \right), \tag{5.3}$$

where the sum runs over all nuclear modes with frequency ω_M and $\mathbf{Q}_M$ is the dimensionless coordinate of the normal mode.

Finally, the electron-phonon coupling part of the Hamiltonian is

$$\mathcal{H}^{\mathrm{el-ph}} = \sum_i \sum_M g_{i,M} \mathbf{Q}_M |i\rangle\langle i| + \sum_{i,j \neq i} \sum_M g_{ij,M} \mathbf{Q}_M |i\rangle\langle j|, \tag{5.4}$$

where we have explicitly splitted the total electron-phonon coupling in its two contributions: the local $(g_{i,M})$ and the nonlocal $(g_{ij,M})$ electron-phonon

couplings. The former describes the modulation of the site energies, while the latter concerns the modulation of the transfer integrals. Several works have dealt with the evaluation of the local electron-phonon coupling [159], which is now a routine calculation. On the contrary, we are interested in the non-local electron-phonon coupling $g_{ij,M}$, which determines the dynamic disorder and the fluctuation of the transfer integral σ_{ij}. This latter quantity can be evaluated at a given temperature from the electron-phonon coupling value as [160]:

$$\sigma_{ij}^2 = \left\langle (V_{ij} - \langle V_{ij}\rangle)^2 \right\rangle = \sum_M \frac{|g_{ij,M}|^2}{2} \coth\left(\frac{\hbar\omega_M}{2k_{\mathrm{B}}T}\right), \qquad (5.5)$$

where $k_{\mathrm{B}}T$ is the thermal energy.

It has been shown that the modulation of the transfer integral as a consequence of coupling to the phonon modes is of the same order of magnitude as the transfer integral itself [149], comparable with the characteristic timescale of carrier dynamics [25, 77]. More importantly, this quantity is now considered the factor ultimately limiting charge transport [107, 149] and it is one of the most important quantities involved in the transient localization theory (TLT).

As explained in more detail in ref.s 107, 108, 157, the TLT introduces the definition of a new quantity $L^2(t)$, called transient localization length for reasons that will become clear later

$$L^2(\tau) = \int_0^\infty \frac{\mathrm{d}\Delta X^2(t)}{\mathrm{d}t} e^{-t/\tau} \mathrm{d}t, \qquad (5.6)$$

where $\Delta X^2(t)$ is the mean square displacement (MSD) reached by a moving charge in the system after a time t.

Then, we resort to the relaxation time approximation (RTA). The basic idea underlying RTA is to express the dynamical properties of the actual system in terms of those of a suitably defined reference system from which it decays over time. It is easy to see that if we choose a system showing only static disorder, the RTA allows to recover the dynamic disorder due to low-frequency vibrational motion. Indeed, in an OSC where molecular positions

fluctuate on a timescale τ_{in}, the molecular lattice appears as a frozen disordered landscape to the moving charges, so its properties (indicated with $C(t)$) coincide with that of a system showing only static disorder (indicated by $C^{\mathrm{ref}}(t)$). However, due to lattice dynamics, the charges encounter different landscapes when moving, destroying interferences and restoring the diffusion process. This corresponds to a decay from the reference state, whose simplest mathematical form is:

$$C_+(t) = C_+^{\mathrm{ref}}(t)e^{-t/\tau_{in}} \tag{5.7}$$

Recalling the definition of the instantaneous diffusivity $D(t)$,

$$D(t) = \frac{1}{2}\frac{\mathrm{d}\Delta X^2(t)}{\mathrm{d}t} \tag{5.8}$$

and using the properties of the Laplace transform and the RTA [108, 157], the diffusion coefficient D can be expressed as:

$$D = \frac{L^2(\tau_{in})}{2\tau_{in}}. \tag{5.9}$$

Now it should be clear why L^2 is called "transient localization length": it is the MSD reached by the charge in a characteristic time τ_{in}, the time needed for the disorder to fluctuate, equal to the inverse of the intermolecular oscillation frequency (a typical value is 1 ps).

Substituting the diffusion coefficient in the Einstein formula for the mobility 3.30, we get

$$\mu = \frac{e}{k_{\mathrm{B}}T}\frac{L^2(\tau_{in})}{2\tau_{in}}, \tag{5.10}$$

where, resorting to Lehmann's representation of the mean square displacement expressed in terms of the position operator [108, 157], L^2 can be computed as

$$L^2(\tau_{in}) = \frac{1}{Z}\sum_{n,m}e^{-\beta E_n}\left|\langle n|[\mathcal{H},\mathcal{X}]|m\rangle\right|^2\frac{2}{(\frac{1}{\tau_{in}})^2 + (E_m - E_n)^2}. \tag{5.11}$$

Here $|m\rangle$ and $|n\rangle$ are two generic eigenvectors of the Hamiltonian $\mathcal{H}$ with corresponding eigenvalues E_m and E_n, while $\mathcal{X}$ is the position operator.

It should be noticed that, up to now, we have focused on equations describing 1-dimensional charge transport, however, in section 3.4, we have pointed out that in most OSCs, charge migration mainly occurs in the so-called high-mobility plane, i.e. it is a 2-dimensional transport.

Generalization of TLT to 2-dimensional charge transport is extremely straight-forward [54], since the total localization length is the mean of the contributions along the two directions, say x and y

$$L^2(\tau_{in}) = \frac{L_x^2(\tau_{in}) + L_y^2(\tau_{in})}{2}. \tag{5.12}$$

Summarizing, using this method the dynamic properties of the system are expressed as the decay (on the timescales of thermal motions) from a reference system with only static disorder. The Hamiltonian of the reference system is therefore built up with off-diagonal disorder modeled as Gaussian functions centered in V (transfer integral value) with a width equal to σ (oscillation of the transfer integral). Then $L^2(\tau_{in})$ is averaged over several computations, each one with a randomly sampled off-diagonal disorder, to statistically account for different disorders in real samples.

In the following section we will see an approach, developed in collaboration with prof. Alessandro Troisi from Liverpool University, for the fast evaluation of the non-local electron phonon coupling, which describes the strength of the thermal motions σ (eq. 5.5), the fundamental ingredient for the application of TLT model.

5.1 Non-local electron-phonon coupling

Even if in this thesis we focus on the TLT method, several models (mentioned in the previous section) require the computation of the non-local electron phonon coupling [161, 162]. Unfortunately, this property is computationally expensive to evaluate, a drawback that prevented the study of this property on large databases of molecules. However, the screening of

a large number of materials could reveal chemical patterns leading to new design rules for materials less sensitive to disorder.

The slow step for the computation of the non-local electron phonon coupling is the evaluation of the crystal vibrations and, for this reason, many rely on empirical force fields [163, 164]. However, empirical force fields can be inaccurate (since usually they are not parametrized to describe low frequency modes) and, most importantly, they need to be re-parametrized to describe every new chemical functionality that is introduced in novel compounds. On the other hand, evaluations of the phonons of molecular crystals starting from first principles, even if fairly well established [159, 165–167], are very difficult to perform on materials with hundreds of atoms in the unit cell − a common occurrence in organic semiconductors − because of their computational cost, so they cannot be used as a routine protocol for the screening of new materials.

The aim of this section is the development of a fast methodology for the evaluation of the dynamic electronic disorder in organic materials, relying on two main ideas: (i) the calculation of the electron-phonon coupling with respect to Cartesian displacement and (ii) the use of simplified phonons evaluated in the framework of the rigid-body approximation, [4, 160] where each molecule is assumed to oscillate independently, with the great advantage of separating effectively the internal (intramolecular vibrations) and external (intermolecular vibrations) degrees of freedom.

The transfer integrals V_{ij} are influenced by the set of displacements $\{\mathbf{Q}_M\}$. In particular, writing the Taylor series expansion V_{ij} around the equilibrium position, the couplings $\{g_{ij,M}\}$ appear in its second term:

$$V_{ij}(\{\mathbf{Q}_M\}) \cong V_{ij}(\{\mathbf{Q}_M\} = 0) + \sum_M g_{ij,M}\mathbf{Q}_M + \sum_{M,N} \frac{\partial^2 V_{ij}}{\partial \mathbf{Q}_M \partial \mathbf{Q}_N}\mathbf{Q}_M\mathbf{Q}_N + \dots$$

$$(5.13)$$

that is, the $\{g_{ij,M}\}$ can be evaluated as

$$g_{ij,M} = \left. \frac{\partial V_{ij}(\{\mathbf{Q}_M\})}{\partial \mathbf{Q}_M} \right|_{\{\mathbf{Q}_M\}=0} \qquad (5.14)$$

As outline in chapter 3, the transfer integrals are evaluated as [112]:

$$V_{ij} = \left\langle \phi_i^0(\{\mathbf{Q}_M\}) \middle| \mathcal{F}(\{\mathbf{Q}_M\}) \middle| \phi_j^0(\{\mathbf{Q}_M\}) \right\rangle. \tag{5.15}$$

where ϕ_i^0 and ϕ_j^0 are the localized HOMOs of molecule i and j, respectively, and $\mathcal{F}$ is the Fock operator of the dimer system. The suffix 0 indicates that the orbitals are unperturbed, i.e. computed for the isolated molecule.

We have represented the mode M as a vector of Cartesian displacements $\mathbf{Q}_M = \{x_k^M\}$, which spans the entire supercell, so we can write $g_{ij,M}$ as:

$$g_{ij,M} = \nabla V_{ij} \cdot \mathbf{Q}_M. \tag{5.16}$$

Here, ∇V_{ij} is the Cartesian gradient of the transfer integral, that is the derivative of the transfer integral with respect to the Cartesian displacement of an atom k:

$$\nabla V_{ij} = \left\{ \frac{\partial V_{ij}}{\partial x_k} \right\}, \tag{5.17}$$

where the elements of the vector ∇V_{ij} are zero if displacements x_k do not belong to molecule i or j.

Eq. 5.16 is particularly suited for the development of a fast protocol because the first term of the product (∇V_{ij}) only includes $6N_A$ differentiations (where N_A is the number of atoms in one molecule) and the second term does not depend on the transfer integral, so it needs to be evaluated only once. Anyway, it should be stressed that the gradient of the transfer integral can be evaluated relatively quickly (e.g. in less than 1 day per typical molecule using 16 processors), but the computation of all the lattice phonons $\mathbf{Q}_M$ is a computationally expensive task, in particular when a good sampling of the Brillouin zone is required [55, 160, 161].

To speed up the computations we use Einstein dispersionless phonons, that is, phonons evaluated assuming that each molecule oscillates independently from the others, separating intra- and intermolecular degrees of freedom. The former are assumed to be the vibrations of the isolated molecule, an excellent approximation particularly for high frequency modes, which are

known to show small frequency variations between bulk solid-state phases and solution [168, 169].

The intermolecular motion is described as the rigid motion of each molecule surrounded by the neighbouring molecules frozen in their equilibrium position [170–172]. In order to do this, we define three translations and three rotations, and then we numerically compute the 6×6 Hessian matrix $\mathbf{P}_{ij} = \partial^2 E / \partial \mathbf{q}_i \partial \mathbf{q}_j$ corresponding to these 6 modes $\mathbf{q}_1 \dots \mathbf{q}_6$, where E is the total energy of a cluster constituted by a molecule surrounded by all molecules in van der Waals contact according to the crystal structure. The eigenvalues ω_M^2 of the Hessian give the square of the frequencies of the "intermolecular" modes and the corresponding eigenvectors $\mathbf{w}_{j,M}$ allow us to represent the rigid molecules modes $\mathbf{Q}_M$ as linear combination of the original roto-translational modes:

$$\mathbf{Q}_M = \sum_{j=1}^{6} \mathbf{w}_{j,M} q_j. \tag{5.18}$$

Part III

CT IN ORGANIC SEMICONDUCTING CRYSTALS

Chapter 6

Overview

As extensively discussed in part I, research towards the identification of new, better OSCs (i.e. those showing higher mobilities together with easier processability) is very active; however, progresses in this respect have been slowed down by the limited theoretical understanding of the charge transport properties due to the complexity of organic materials and the wide variety of structures. Indeed, the computational methodology for the prediction of the charge mobility needs to be related to a mechanism of charge transport, inasmuch as different mechanisms require the evaluation of different parameters. For example, using the Marcus theory, the charge mobility is determined through the evaluation of the transfer integral between the interacting molecules and the reorganization energy [19, 56, 173], an approach that has been successfully used for the screening of big databases [174].

Unfortunately, while for inorganic semiconductors the band-transport model is now widely accepted, there is no such a consensus about the most appropriate theoretical approach to model charge transport in organic semiconductors, in particular when dealing with high-mobility semiconductors, that is those showing mobilities higher than ≈ 1 cm^{2}V^{-1}s^{-1} [54, 175]. Such controversy is mainly due to the fact that organic molecular crystals are

only weakly bound by van der Waals intermolecular interactions, so that lattice vibrations play a more important role in organic than in inorganic materials [54, 176].

For that reason, it has been proposed that possibly, neither the hopping nor the band-like mechanism are adequate in describing charge transport in organic semiconductors [54, 147, 149, 150, 156, 177, 178]. Going into the details, several authors pointed out that hopping theories yield to unphysically high transition rates [54, 56, 175] or, when used in conjunction with rate constants obtained by Marcus theory, they predict a thermally activated mechanism not consistent with experimental observations [54, 149]. On the other hand, a band-like mechanism is ruled out by the short mean free path observed in OFET, on the order of the intermolecular distances, not compatible with the basic assumptions underlying band transport theory [107, 179, 180]. Several alternative models have been proposed, based on Ehrenfest dynamics [151], modified surface hopping [152], open quantum systems dynamics [153], many-body physics methods [154] relying both on model Hamiltonians [155] and realistic chemical models [139, 147, 148, 156]. Among these, Fratini et al. recently proposed a method [107, 108], described in part II of this thesis, based on the idea that the unavoidable disorder in real crystals leads to a "transient localization" which slows down carrier mobility, but the fluctuations in time of crystal disorder allow for charge diffusion to take place.

Despite the abovementioned limitations of the hopping approach, both theoretical evaluations [150] and experimental measurements [18] on the scaling of mobility with temperature indicate that hopping model leads to reliable results around room temperature. Besides, a comparison between localized (Marcus) and delocalized (semiclassical dynamics) models showed that they predict quite similar mobilities, even if charge delocalization is taken into account at room temperature [181]. In addition, weak molecular interactions in organic crystals result in strong thermal motion and lattice distortion, giving rise to quite large fluctuations in the transfer integral

[149]. This breaks the translational symmetry of the electronic Hamiltonian and leads to localized charge carriers, even in pentacene, despite its low reorganization energy and large transfer integrals [81]. Finally, it has been pointed out that inclusion of nuclear tunneling effects in the hopping rates, for example using FGR, does not result in thermally activated mobilities [81, 118]. This is an important point, indicating that the hopping mechanism cannot be excluded only on the basis of the observed decreasing of the mobility with temperature. Nevertheless, it has been shown that FGR can lead to strongly overestimation of hole mobilities, in particular when dealing with high-mobility organic semiconductors, possibly because of the intrinsic limits of FGR in treating ultrafast transitions [56]. An improvement in this respect should be represented by the SOC approach, which should be adequate in treating ultrafast transitions, since it allows to take into account the change of the reaction rate with time. Moreover, being a full quantum mechanical model, it should lead to correct temperature dependence unlike Marcus theory.

In this part of the thesis, we will focus on the comparison of the five theoretical models previously described. In particular, in the first chapter we will show that the SOC approach can well reproduce experimental mobilities even when FGR fails (i.e. for high mobility semiconductors), as well as the experimental scaling of the mobility with temperature. In the second chapter of this part we will focus on the TLT theory, which should go beyond both band theory (since it contains quantum localization correction) and hopping models (since it does not predict the loss of coherence after each hop). In particular, since this theory takes into account the fluctuations of the transfer integral with time because of thermal motion, we will focus on the development of a computational protocol for the quick evaluation of this fluctuation. This study is a first step towards the final goal of developing a method suitable for material discovery through the analysis of big databases such as the Cambridge Structural Database (CSD)[88].

Chapter 7

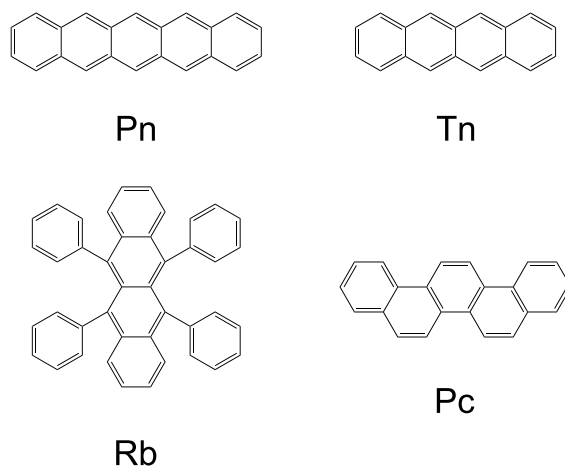# Comparison of Marcus theory, FGR and SOC

Figure 7.1. Molecular structure of the OSCs studied. Full names are: Pn = pentacene; Tn = tetracene; Rb = rubrene; Pc = picene.

In this chapter we compare the results obtained by using Marcus theory, FGR and SOC approach for pentacene, tetracene, rubrene and picene

(fig. 7.1), four of the most studied organic semiconductors because of their relatively high experimental mobility [19]. The crystal structure for these 4 molecules is derived from the Cambridge Structural Database (CSD) [88]. The CSD codes are: IUCr A03426 for tetracene, 1230799 for pentacene, 605647 for rubrene and 560122 for picene.

As discussed in part II, the majority of molecular semiconductors have a crystal structure with a high-mobility plane [133, 182, 183], so here we refer to a standard 2D lattice where there can be up to three nearest-neighbour transfer integrals (fig. 8.2). Indeed, allowing for some of the transfer integrals to be zero, or for pairs of parameters to be identical, such a lattice can describe almost all high-mobility organic molecular semiconductors [54]. So, in fig. 7.3 the intermolecular arrangements corresponding to the fastest
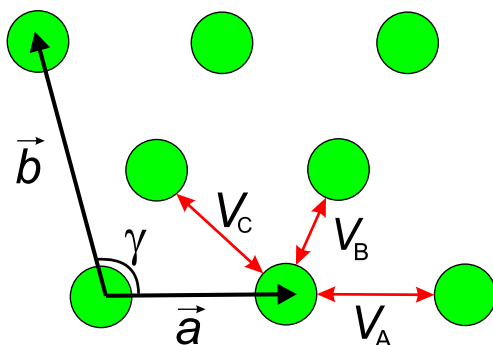
Figure 7.2. Definition of a standard 2D lattice used to present the parameters needed for the calculation of the mobility. a and b identify any two crystallographic axes and γ is the angle between them.

hole paths [131, 184] are shown and labeled according to the scheme in fig. 7.2.

In table 7.1 we report the wavenumbers ω of the most displaced normal modes for the hole injection half reaction and their contributions (E_r, harmonic approximation) to the total reorganization energies. In the last line of the table the total electronic reorganization energy computed at
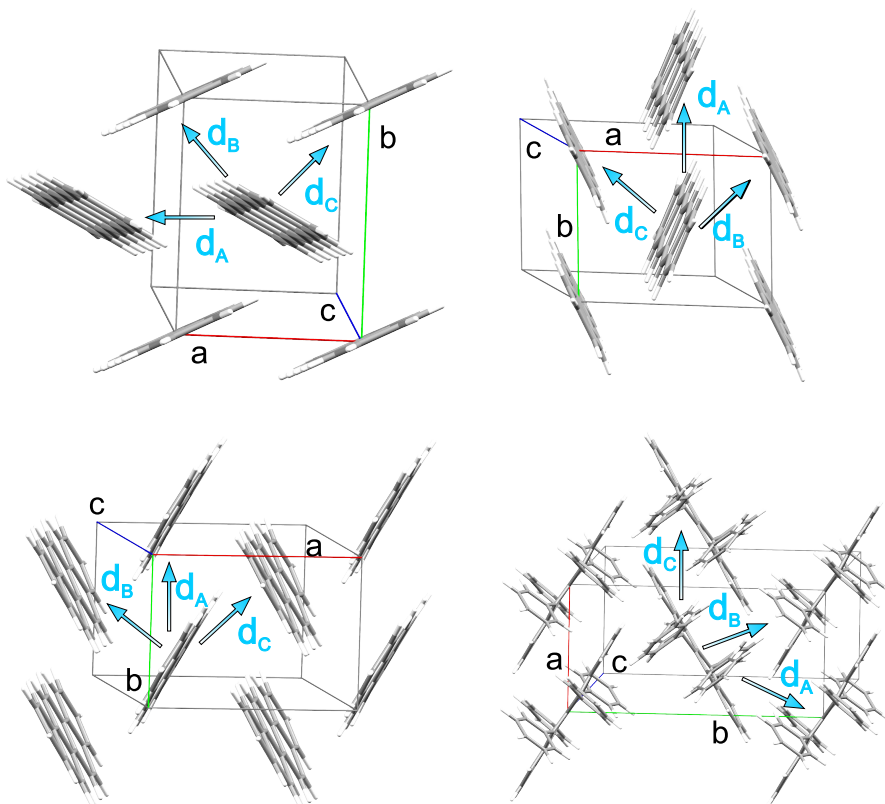
Figure 7.3. Hole hopping paths in: pentacene (top left), tetracene (top right), picene (bottom left), and rubrene (bottom right) crystal structures.

PCM/B3LYP level, using an effective dielectric constant $\epsilon = 4$ (the average value of the dielectric constants for the OSC crystals under study according to previous works [21]) is reported.

It is important to notice that, even if we have performed our computations using PCM/B3LYP with $\epsilon = 4$, the effect of the dielectric constant is almost insignificant on both equilibrium position displacements and reorganization energies, as shown in table 7.2, where we report the same quantities of table 7.1 evaluated in gas phase.

Table 7.1. Wavenumbers (ω, cm^{-1}), intramolecular reorganization energies (E_r, cm^{-1}), and equilibrium position displacements (**K**, absolute values Å uma$^{1/2}$) of the most displaced normal modes of Pn/Pn$^+$, Tn/Tn$^+$, Pc/Pc$^+$ and Rb/Rb$^+$ redox pairs. All data refer to hole injection X $\to$ X$^+$. Electronic calculation at the B3LYP/6-31+g(d,p), PCM $\epsilon = 4$.

Pn/Pn$^+$			Tn/Tn$^+$			Pc/Pc$^+$			Rb/Rb$^+$		
ω	E_r^a	**K**	ω	E_r^a	**K**	ω	E_r^a	**K**	ω	E_r^a	**K**
263	9	0.36	317	9	0.24	32	30	1.00	24	73	2.30
797	3	0.08	761	4	0.11	259	45	0.59	68	11	0.57
1023	6	0.11	1186	23	0.20	425	10	0.21	89	29	0.86
1186	13	0.15	1232	61	0.31	593	70	0.49	214	14	0.36
1213	54	0.29	1420	25	0.18	1390	217	0.56	252	8	0.25
1421	106	0.43	1435	142	0.44	1654	143	0.42	995	20	0.20
1564	131	0.41	1652	112	0.38	1665	137	0.41	1340	127	0.43
									1583	108	0.37
$E_\mathrm{r,tot}^b$	382			736			608			448	

^{a}Computed by harmonic approximation from **K** components. ^{b}From electronic computations.

Table 7.2. ω (cm^{-1}), E_r (cm^{-1}), **K** (absolute values, Å uma$^{1/2}$) of the most displaced normal modes of Pn/Pn$^+$, Tn/Tn$^+$, Pc/Pc$^+$ and Rb/Rb$^+$. Electronic calculation at the B3LYP/6-31+g(d,p), gas phase.

Pn/Pn$^+$			Tn/Tn$^+$			Pc/Pc$^+$			Rb/Rb$^+$		
ω	E_r^a	**K**	ω	E_r^a	**K**	ω	E_r^a	**K**	ω	E_r^a	**K**
263	9	0.26	318	3	0.15	41	27	0.20	21	68	2.38
804	2	0.07	760	2	0.06	260	62	0.70	68	8	0.48
1023	4	0.09	1187	23	0.20	426	8	0.19	84	32	0.90
1186	21	0.19	1230	52	0.29	595	64	0.47	213	9	0.30
1213	54	0.30	1420	27	0.20	1392	220	0.56	253	5	0.20
1442	139	0.44	1434	142	0.44	1657	148	0.42	996	21	0.20
1564	82	0.32	1654	117	0.38	1665	129	0.40	1336	119	0.42
									1586	111	0.37

^{a}Computed by harmonic approximation from **K** components.

We have computed the photoelectron spectra of the four molecules using the components of the **K** vectors of Table 7.1, comparing them with their experimental counterpart [115, 185, 186]. Computed and experimen-
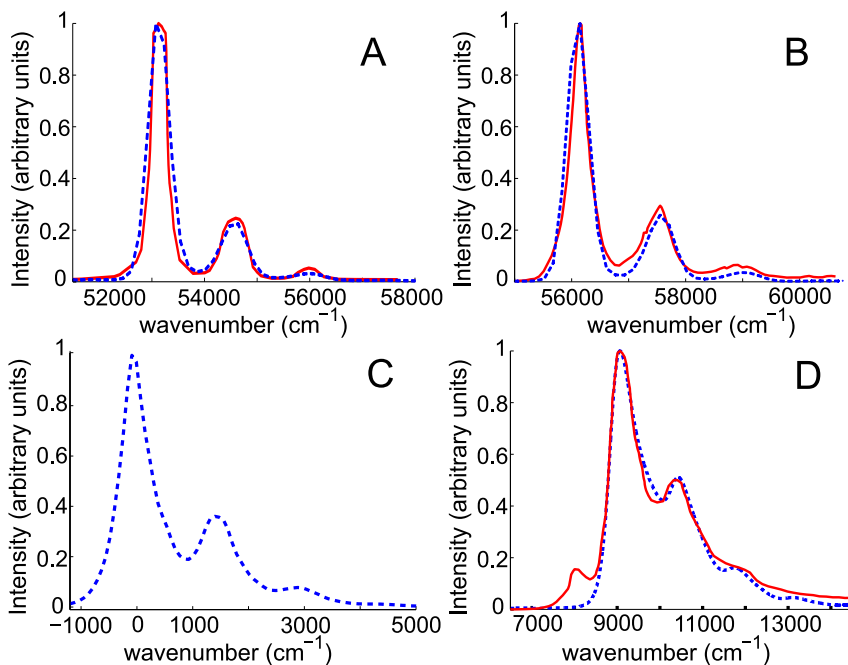

Figure 7.4. Experimental (red full line, ref.s 115, 185, 186) and computed (blue dashed line) photoelectron spectrum of: Pn at $T = 505$ K (A); Tn at $T = 480$ K (B); Pc at $T = 468$ K (C); Rb at $T = 140$ K (D). The experimental spectrum of Pc is not shown because it exhibits two overlapping electronic transitions, a complication not considered here.

tal spectra are in good agreement between each other (fig. 7.4), ensuring the reliability of our approach. Only the computed spectrum of rubrene shows slight discrepancies, at low wavenumbers, with the experimental one. A more accurate approach to describe that spectral region would require the use of anharmonic potentials [187, 188], but this would preclude the inclusion of all normal modes for the computations of hole transfer rates. For that reason we have decided to still work in harmonic approximations.

The experimental spectrum of picene (ref. 185) is not shown since it displays two overlapping electronic transitions, so it is not comparable with the simulated spectrum, where only the first transition has been included.
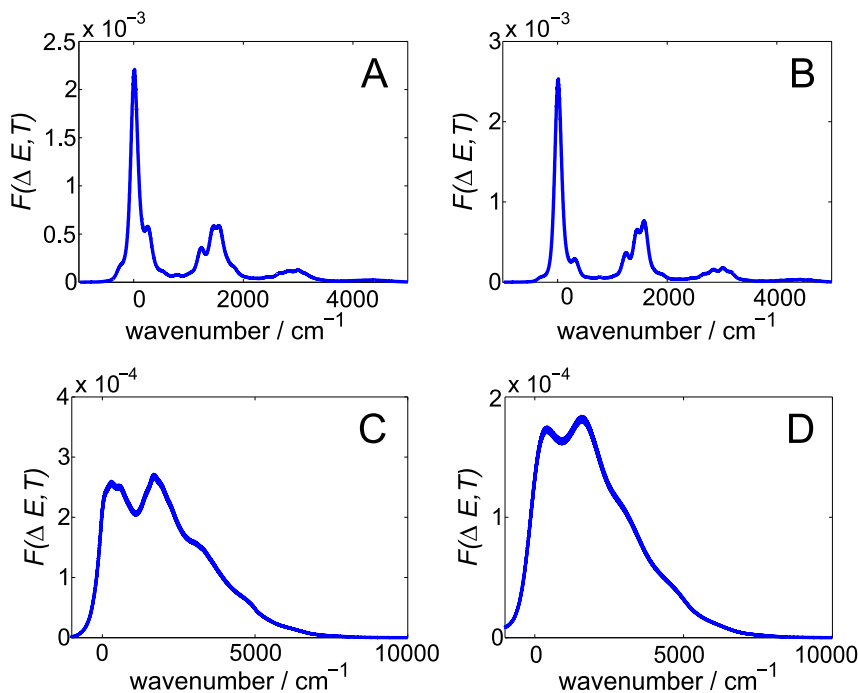

Figure 7.5.   Computed densities of states for hole hopping in Pn (A), Tn (B), Pc (C), and Rb (D). $T = 298$ K; all mode calculation.

In fig. 7.5 the computed Franck-Condon weighted densities of states ($F(\Delta E, T)$) for hole hopping in homodimers are reported as a function of ΔE. For Pn and Tn, $F(\Delta E, T)$ is peaked around $\Delta E = 0$ with a total width of about 3000 cm^{-1}, while, for both Rb and Pc, it is a much broader function of ΔE, with a total width of more than 6000 cm^{-1}. This difference is related to the presence, for Rb and Pc, of strongly displaced normal modes at low energies, significantly below the thermal energy at $T = 298$ K (Table 7.1).

Table 7.3. Kinetic constants ($k/10^{13}$ s^{-1}) and mobilities ($\mu/$cm^{2}V^{-1}s^{-1}) along the different hole channels for the 4 molecules under study. Electronic couplings V (meV) obtained as explained in part II (see also table 8.1 and relative discussion in the next chapter).

		Marcus		FGR$^a_{av}$		FGR		SOC$^b_{eq}$		SOC$^c_{neq}$	
	V	k	μ	k	μ	k	μ	k	μ	k	μ
Pentacene (d_A)	+22.3	0.85	0.59	3.16	2.19	6.54	4.52	2.72	1.88	2.54	1.76
Pentacene (d_B)	−77.5	12.0	5.46	44.4	20.24	91.9	41.8	12.3	5.60	11.5	5.23
Pentacene (d_C)	+40.2	2.37	1.18	8.28	3.86	16.9	7.85	4.99	2.36	4.66	2.23
Tetracene (d_A)	+3.60	0.005	0.002	0.015	0.0076	0.04	0.014	0.011	0.006	0.010	0.006
Tetracene (d_B)	+18.9	0.51	0.26	2.33	1.20	5.19	2.66	2.34	1.21	2.29	1.18
Tetracene (d_C)	−70.4	8.26	3.72	39.2	17.7	87.7	39.5	11.3	5.09	10.9	4.91
Rubrene (d_A)	+140	20.4	20.3	19.6	19.5	24.1	23.9	22.2	22.1	33.4	33.2
Rubrene (d_B)	−19.5	0.38	0.47	0.36	0.45	0.44	0.543	0.41	0.506	0.61	0.752
Rubrene (d_C)	−19.5	0.38	0.47	0.36	0.45	0.44	0.543	0.41	0.506	0.61	0.752
Picene (d_A)	+115	8.92	6.57	19.8	14.6	21.5	15.8	20.6	15.2	27.9	20.5
Picene (d_B)	−89.8	5.44	3.02	12.0	6.65	13.1	7.26	12.6	6.98	17.0	9.43
Picene (d_C)	−81.8	4.51	2.32	10.0	5.14	10.9	5.61	10.4	5.35	14.1	7.25

[a]From averaged Franck-Condon weighted density of states. [b]Initial state from the equilibrium thermal distribution of the cationic state. [c]Initial state from the equilibrium thermal distribution of the neutral state.

Marcus, FGR and SOC hole hopping rates for the paths of figure 7.3 at $T = 298$ K are reported in table 7.3 together with the electronic coupling elements adopted, which have been obtained as explained in part II. FGR rates have been calculated either at $\Delta E = 0$, as usual in the literature, or by averaging $F(\Delta E, T)$ over a range of 400 cm^{-1} around $\Delta E = 0$, a practical way to account for the effect of thermal disorder. Time averaged SOC rates used for the evaluation of anisotropic mobilities have been obtained interpolating the populations assuming a monoexponential decay. As we will see in the following, this approximation, whose quality is not known a priori, proves to be effective since it leads to good agreement with experimental results. A better approach would be the inclusion of the time dependent kinetic constants for the evaluation of the mobility, but unfortunately they are incompatible with the model here used (eq. 3.34). Further studies on alternative methods allowing the introduction of time-dependent kinetic constants are ongoing.

As reported in table 7.3, FGR rates for channel d_B of pentacene and d_C of tetracene are very high, leading to transition times of the order of a few femtoseconds. With such ultrafast decay rates, neglect of coherence could be inappropriate, leading to strongly overestimated transition rates. We have checked the reliability of FGR rates by comparing its monoexponential decay with the time dependent population $P(t)$ obtained with the SOC approach, adopting as initial state the equilibrium thermal distribution of the cationic state (SOC$_{eq}$ in table 7.3) or the equilibrium distribution of the neutral state (SOC$_{neq}$ in table 7.3). The latter approach may be physically more appropriate for ultrafast transitions, when hole transfer is fast enough to compete with vibrational relaxation to the thermal equilibrium distribution.

As shown in fig. 7.6 for channel d_B of pentacene and channel d_C of tetracene, FGR predicts that the initial state completely decays within 5 fs, whereas SOC approach yields a decay time of about 30 fs. Slightly

longer decay times are predicted by FGR when the energy averaged Franck-Condon weighted density of states is used, but decay times still are smaller than 10 fs.

Those results point out that FGR overestimates the hole transfer transition rate in pentacene and tetracene, probably because transitions occur on such a short timescale that the integral representation of the Dirac delta function is unsuitable, making FGR inadequate to describe the transition. Moreover,
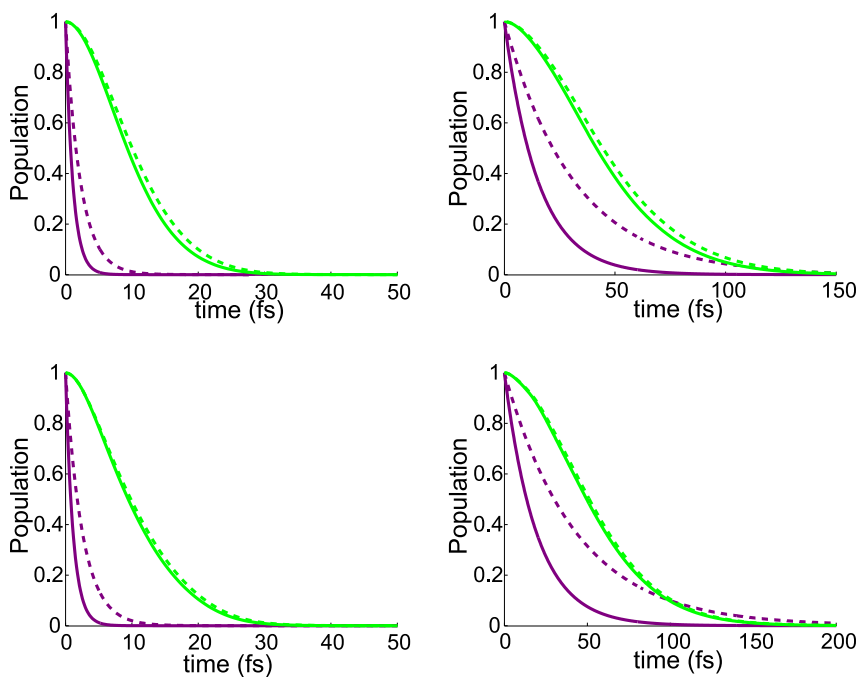

Figure 7.6. Time decay probabilities predicted by FGR and SOC approaches for hole hopping in pentacene and tetracene dimers. Top left: Pn channel d_B; top right: Pn channel d_C; bottom left: Tn channel d_C; bottom right: Tn channel d_B. Purple full line: FGR at $\Delta E = 0$; purple dashed line: FGR averaged over 400 cm^{-1} around $\Delta E = 0$; green full line: equilibrium SOC; green dashed line: non-equilibrium SOC.

from fig. 7.6 we can see that SOC$_{\text{eq}}$ and SOC$_{\text{neq}}$ transition rates are very similar. To gain deeper insight in this behaviour, we notice that all the

displaced modes of Pn/Pn+ and Tn/Tn+ redox pairs fall at relatively high frequency (table 7.1) and $F(\Delta E, T)$ is strongly peaked at $\Delta E = 0$. Both factors concur in making the thermal equilibrium distributions of both the neutral and the cationic states nearly coincident with the ground state. Therefore, SOC rates are virtually independent on the initial population: $\mathrm{SOC}_{\mathrm{eq}}$ and $\mathrm{SOC}_{\mathrm{neq}}$ rates in table 7.3 are very close.

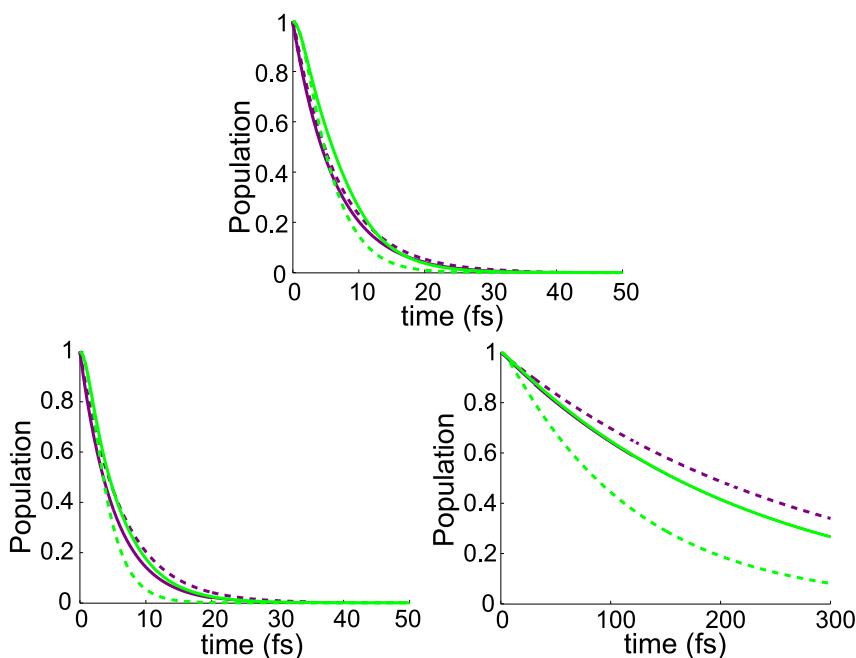Rubrene and picene show a completely different behaviour, related to the

Figure 7.7.   Time decay probabilities for hole hopping in picene and in rubrene. Top: Pc channel d_A; bottom left: Rb channel d_A; bottom right: Rb channel d_B. Purple full line: FGR at $\Delta E = 0$; purple dashed line: FGR averaged over 400 cm^{-1} around $\Delta E = 0$; green full line: equilibrium SOC; green dashed line: non-equilibrium SOC.

fact that they possess low-frequency strongly displaced vibrational modes, together with a broader and lower $F(\Delta E, T)$ than pentacene and tetracene. Indeed, as shown in fig. 7.7, FGR and SOC approaches lead to very similar

results even if FGR still predicts slightly higher rates. Besides, for both picene and rubrene, SOC decay rates depend on the initial population: the equilibrium thermal populations of the neutral state always provide faster rates than those of the cationic one.

To better understand the reasons of this different behaviour, we recall that (see eq. 3.9) $k_{FGR} \propto V^2 F \equiv V_{\text{eff}}$, so, since the highest electronic coupling of all the molecules under study are similar, but pentacene and tetracene have F about one order of magnitude greater than the other molecules, they have a too high V_{eff} to be handled by FGR. In other words, this high V_{eff} gives rise to ultrafast transitions for which coherence effects could not be neglected.

We have also computed decay rates by the numerical solution of the time dependent Schrödinger equation (TDSE) as an additional test for assessing the reliability of the SOC approach. More than 80% of the computed reorganization energies for molecules' oxidation can be accounted for by considering only the few modes in table 7.1, so we have explicitly considered only these nuclear degrees in the dynamics [139]. Quantum dynamics calculations have been performed for increasing size of the basis set and of the active space, in order to have converged results for the time interval considered here. We noticed that using vibrational basis set states with at most three vibrations simultaneously excited leads to convergence, since at higher excitation levels the population decay of the initial state does not show any significant variation. For the four molecules studied we have followed the dynamics starting from the ground vibrational state, either of the cationic or of the neutral species. The results are reported in fig. 7.8 for the fastest hole paths of the four molecular crystals. TDSE and SOC predict a very similar time decay of the initial state, at least until TDSE solution begins to oscillate between initial and final state, a problem which is prevented using SOC approach [99].

We have also computed the temperature dependence of the rate constants using all the three hopping models (fig. 7.9). It is interesting to notice
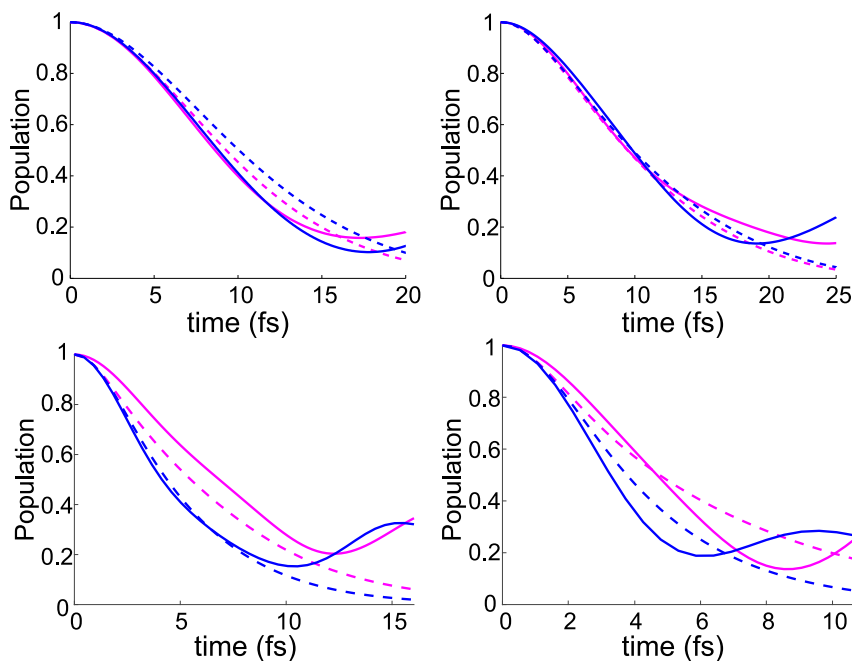
Figure 7.8. Comparison between time decay probabilities for hole hopping in dimers predicted by the TDSE (full line), and from SOC (dashed line). Initial state: equilibrium thermal population of the cationic state, magenta; equilibrium thermal population of the neutral state, blue. Top left: Pn channel d_B; top right: Tn channel d_C; bottom left: Pc channel d_A; bottom right: Rb channel d_A.

that, even if Marcus and SOC approaches yield similar rates at room temperature, the predicted T dependence is very different, showing the limits of the semiclassical approach at low temperatures, where tunneling plays a dominant role. Besides, Marcus and FGR approaches yield rates that significantly depend on temperature, while the averaged SOC rate constants have a very modest temperature dependence, being almost independent on T in the case of pentacene, as it could be expected from the computed normal modes equilibrium position displacements of Table 7.1. The great decrease of FGR rates as T increases is probably an artifact related to

the mentioned inapplicability of FGR to ultrafast processes. Indeed, for rubrene, which is characterized by a lower V_{eff}, FGR and SOC approaches leads to quite similar results, almost indistinguishable at low temperatures, as shown in the right panel of fig. 7.9.
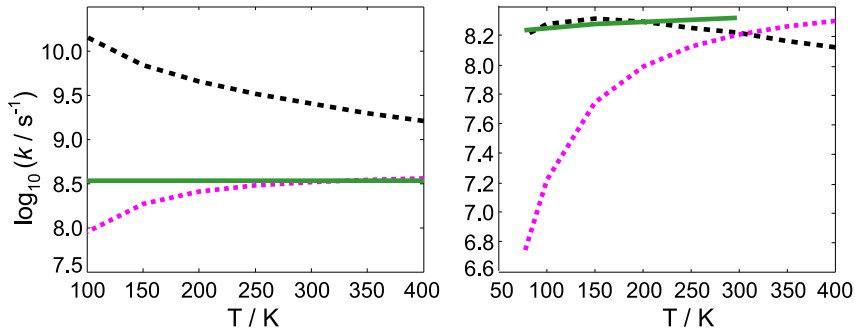

Figure 7.9. Rate constants for Pn (left) and Rb (right) fastest path at different temperatures using FGR (black dashed line), Marcus (dotted purple line), and SOC (green line) approaches.

We have then evaluated the anisotropic mobilities for the four molecules under study, using the methodology discussed in the part II of this thesis, including all the hopping paths shown in fig. 7.3. In fig. 7.10 we have reported the angles formed between the hopping paths and the reference axis a (numerical values are reported in the caption of the figure) in pentacene crystal. As previously discussed, all the hopping paths are in the same plane (ab plane), so that $\gamma = 0$ in eq. 3.34. Using that formula, together with the rates in table 7.3, we have obtained the angular dependence of the hole mobility, shown on the top right of fig. 7.10, where the experimental results of Lee et al. [49, 131] are also reported.

Our results show that FGR mobilities are about one order of magnitude larger than experimental data [49, 189], which on the other hand are in excellent agreement with SOC predictions (see bottom of fig. 7.10). It is important to remark that extracting mobility values from experiments is
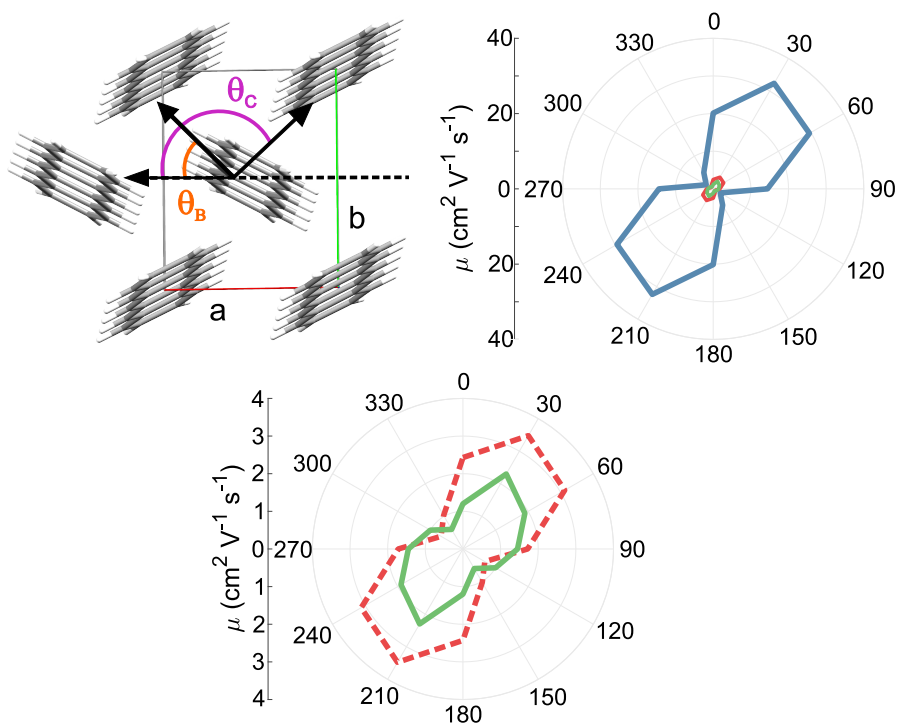
Figure 7.10. Top left: projection of hopping paths in pentacene single crystal to a conducting channel in the *ab* plane; angles relative to the reference axis *a* are: $\theta_A = 0°$, $\theta_B = 47.32°$, $\theta_C = 126.47°$. Top right: polar plot of experimental [49] (green line) and predicted anisotropic hole mobility of pentacene using FGR (blue line) or SOC (red dashed line); bottom: magnified view of experimental and SOC mobilities.

of critical importance, since different research groups have obtained different results for the same material [54, 190]. As discussed in several papers [54, 87], because of the large spread of experimental values reported in the literature, the most reasonable procedure would consist in considering only experimental mobilities showing good reproducibility among different groups. In this respect, we point out that the maximum value of experimental anisotropic mobility here chosen for a comparison with our data is in good agreement with the large majority of mobility values reported in
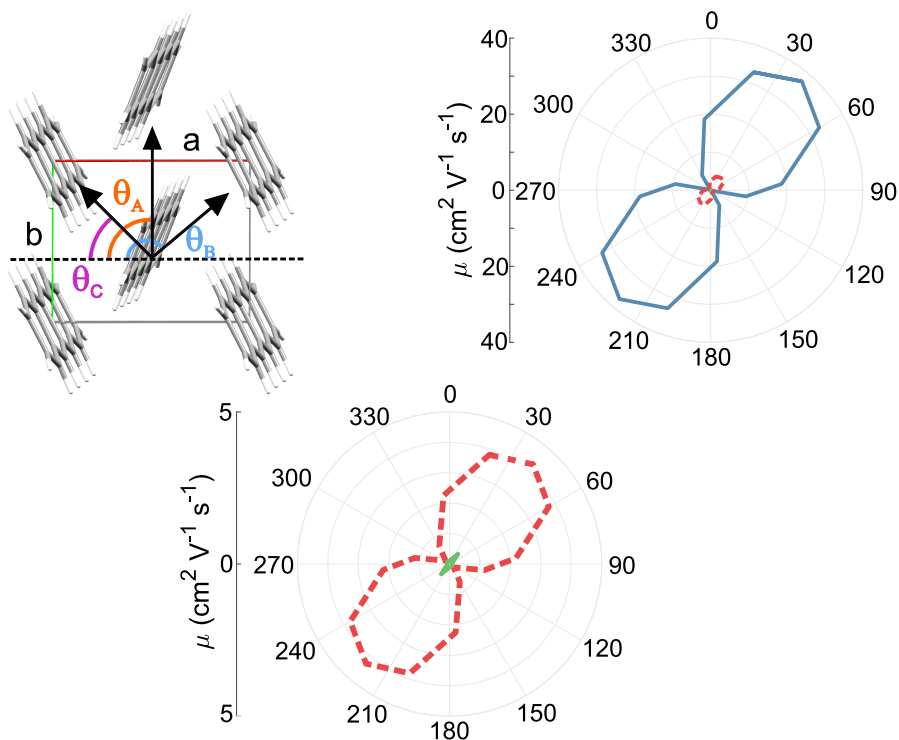
Figure 7.11. Top left: projection of hopping paths in tetracene single crystal to a conducting channel in the *ab* plane; angles relative to the reference axis *a* are: $\theta_A = 90.00°$, $\theta_B = 141.67°$, $\theta_C = 39.95°$. Top right: polar plot of experimental [46] (green line) and predicted anisotropic hole mobility of tetracene using FGR (blue line) or SOC (red dashed line); bottom: magnified view of experimental and SOC mobilities.

the literature for pentacene [50, 191, 192]. However, a quite higher experimental mobility (around 35 $cm^2V^{-1}s^{-1}$ at room temperature) have been reported by Jurchescu et al. in highly purified single crystal of pentacene, in which 6,13-pentacenequinone traps were removed by vacuum sublimation [18]. However, for such high degree of purification it is highly likely that hopping approach is not suitable, because coherence effects should be taken into account, as pointed out by the authors themselves on the basis of the observed temperature dependence of mobility [18].

Tetracene exhibits a similar behaviour, as shown in fig. 7.11, where its anisotropic mobility, evaluated with respect to the reference axis a, is reported. Unlike pentacene, predicted mobilities are quite higher than experimental ones, even SOC predictions. However, this is probably related to the fact that experimental samples unavoidably contain impurities, defects and dislocations which have not been considered in our model. In line with this point, recent experimental measurements [24] carried out on purer samples led to significantly higher mobilities, up to 2.4 $cm^2V^{-1}s^{-1}$, in good agreement with our SOC results.
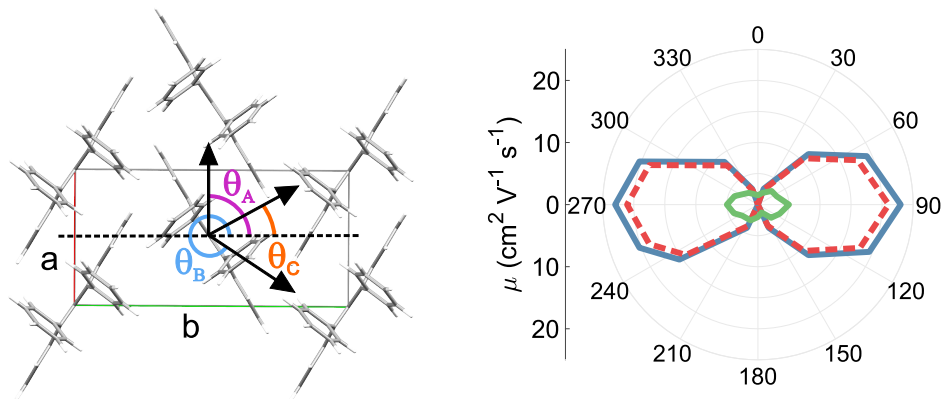

Figure 7.12. Projection of hopping paths in rubrene single crystal to a conducting channel in the ab plane (left); angles relative to the reference axis b are: $\theta_A = 90.0°$, $\theta_B = 331.70°$, $\theta_C = 28.30°$. On the right, the polar plot of experimental [189] (green line) and predicted anisotropic hole mobility of rubrene using FGR (blue line) or SOC (red dashed line).

Rubrene and picene show a quite different behaviour: as previously discussed, FGR is adequate for the description of CT in these system, so it should lead to reliable mobility values.

Indeed, the anisotropic mobilities obtained by both FGR and SOC approach for rubrene (see fig. 7.12) are almost indistinguishable from each other, but quite higher than experimental data, whose angular dependence is however reproduced. Nevertheless recent experimental measurements [24]

led to higher mobilities, about 20 cm^{2}V^{-1}s^{-1} at room temperature [193], in very good agreement with our results.

It is interesting to notice that, as pointed out elsewhere [131], while for rubrene the direction along which the anisotropic mobility reaches its maximum is along the dimer with the largest electronic coupling, pentacene behaves differently. This is due to the fact that pentacene has different hopping paths whose electronic couplings are of the same order of magnitude, while for rubrene one electronic coupling is much larger than all the others.
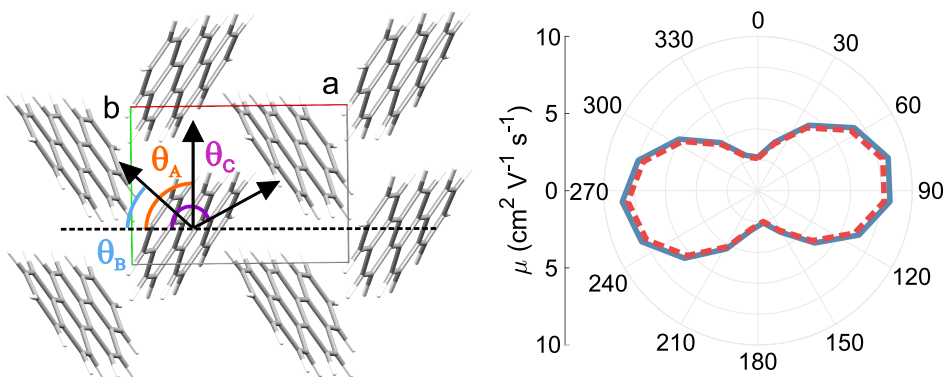
Figure 7.13. Projection of hopping paths in picene single crystal to a conducting channel in the ab plane (left); angles relative to the reference axis a are: $\theta_A = 87.10°$, $\theta_B = 37.30°$, $\theta_C = 142.05°$. On the right, the polar plot of predicted anisotropic hole mobility of picene using FGR (blue line) or SOC (red dashed line).

Picene anisotropic mobility (fig. 7.13) shows an excellent agreement between FGR and SOC. Unfortunately, to the best of our knowledge, no experimental results have been reported yet in the literature to be compared with our data. Anyway, upper limits for picene mobility have been reported [194] around 9 cm^{2}V^{-1}s^{-1}, in good agreement with our results.

For all the molecules under study we have not shown anisotropic mobilities based on Marcus rate constants, because they are very similar to SOC ones, as can be inferred from the rates in table 7.3. However, on the

basis of this analysis, it is only possible to conclude that Marcus approach is adequate for the evaluation of the mobilities at room temperature, but nothing can be inferred about the validity of Marcus mobilities at different temperatures, in particular because, as discussed earlier, the T dependence of the rate constant predicted by Marcus theory is quite different from FGR and SOC ones.

It is important to notice that the temperature dependence of the mobility depends on two factors: (i) the T dependence of the CT rates themselves and (ii) the inverse T dependence included in the Einstein relation (eq. 3.30). To gain deeper insight, we have computed hole mobilities of pentacene and rubrene at different temperatures (fig. 7.14). For both molecules, Marcus formula leads to a thermally activated behaviour, predicting increasing mobility values as T increases, in contrast with experimental data. Marcus formula failure at low temperatures is somewhat expected, since it treats molecular modes classically, an approximation valid only at relatively high temperatures. On the contrary, in line with experimental behaviour, both FGR and SOC approaches predict a decrease of the hole mobility with increasing temperature for both pentacene and rubrene.

In particular, SOC temperature dependence of mobility for pentacene is in fairly good agreement with the experimental trend reported in ref. 18, although predicted and observed mobilities are somewhat different. The discrepancy between experimental and theoretical data increases as the temperature decreases, possibly because coherence effects play a larger role at lower temperatures. As expected because of its inapplicability to this system, FGR mobility is severely overestimated with respect to the experimental data. We remark once again that our discussion is restricted to single crystals, for which hole mobility was observed to decrease upon increasing temperature [18]. This should be kept in mind, since experimental mobilities for other pentacene-based devices are somewhat contradictory: in thin films different behaviours have been observed, including an almost temperature independent device mobility [195–197].
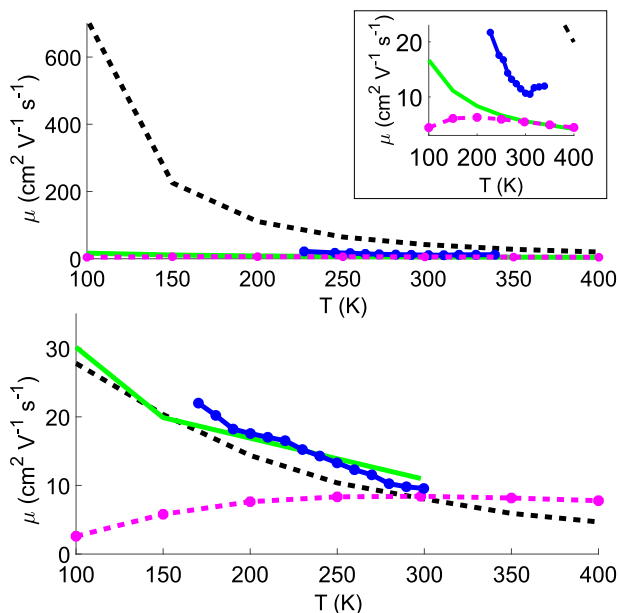
Figure 7.14. Predicted hole mobilities as a function of the temperature for: pentacene (top) and rubrene (bottom). Green full line: SOC approach; black dashed line: FGR; pink dashed line with dots: Marcus formula; blue full line with dots: experimental values from ref.s 18 (pentacene) and 193 (rubrene). Inset: detailed comparison of experimental, SOC and Marcus mobilities for pentacene.

As concerns rubrene, FGR and SOC temperature dependence are very similar both yielding to increasing mobility with decreasing temperature. Our predictions (bottom panel in fig. 7.14) are also in excellent agreement with the observed values, which vary from ≈ 25 cm^2 V^{-1} s^{-1} at 175 K up to ≈ 10 cm^2 V^{-1} s^{-1} at 300 K [23, 193].

Chapter 8

Fast evaluation of electron-phonon coupling

The results presented in the previous chapter have been obtained under the assumption that the transfer integral value does not change during the charge transfer process. However, it is now widely accepted [53, 54, 149, 150] that the transfer integral undergoes large fluctuations because of thermal motions, which is one of the key factors limiting the charge mobility of molecular semiconductors. This quantity is computationally expensive to evaluate, thus posing a severe impediment towards the development of a fast protocol for exploring new materials. With this in mind, in part II we have proposed a methodology relying on two main ideas: (i) the calculation of the electron-phonon coupling with respect to Cartesian displacements and (ii) the use of phonons evaluated in the simplified framework of the rigid-body approximation, [4, 160] where each molecule is assumed to oscillate independently, with the great advantage of separating effectively the internal (intramolecular vibrations) and external (intermolecular vibrations) degrees of freedom.

Here this methodology is applied to study a selection of organic semiconductors widely investigated in the literature (fig. 8.1) because they show the
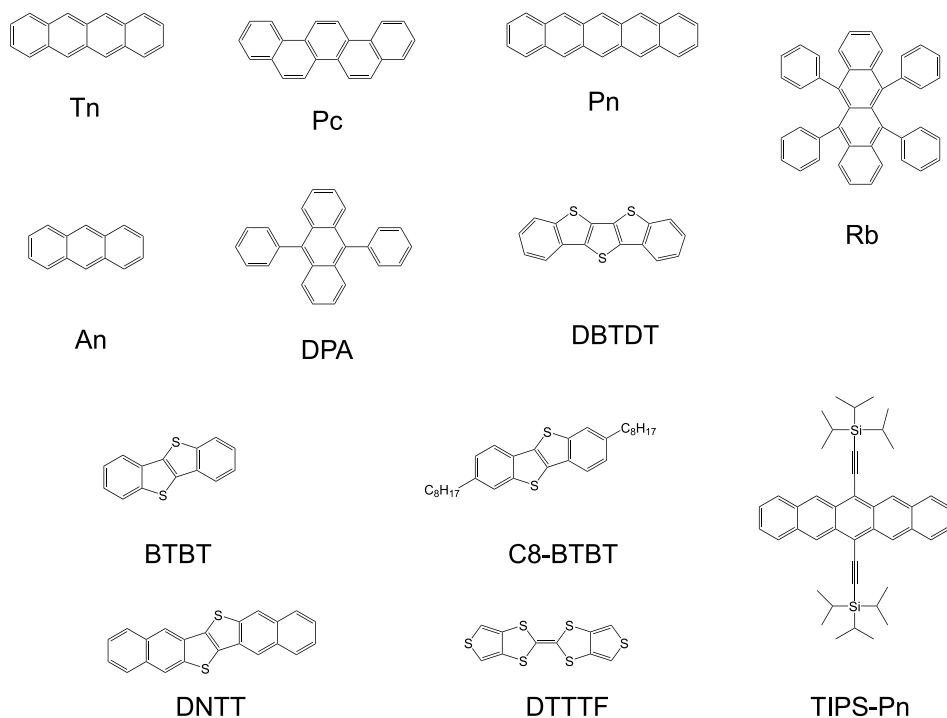
Figure 8.1. The organic molecules studied in this chapter. Full names are: An=anthracene; Pn = pentacene; Rb = rubrene; Tn = tetracene; Pc = picene; BTBT = [1]benzothieno[3,2-b][1]benzothiophene; C8-BTBT = 2,7-dioctyl[1]benzothieno[3,2-b][1]benzothiophene; TIPS = 6,13-bis(triisopropylsilylethynyl)pentacene; DPA = diphenil-anthracene; DTTTF = dithieno-tetratiofulvalene; DBTDT = dibenzo-thieno-dithiophene; DNTT = dinaphtho-thieno-thiophene.

highest mobilities recorded up to now [19, 20, 54, 198]. After a few tests ensuring the reliability of our approach, we outline some general trends which could provide a useful starting point towards a more rational approach to the discovery of new OSCs. Finally, in the last part of the chapter we evaluate the mobility for rubrene, pentacene, tetracene and picene using the TLT and compare the results with data obtained in the previous chapter using hopping models.

We use here the same standard 2D lattice discussed in the previous chapter to identify the interacting couples in the organic semiconductors studied [54].

Figure 8.2.   Definition of a standard 2D lattice used to present the parameters needed for the calculation of the mobility. a and b identify any two crystallographic axes and γ is the angle between them.
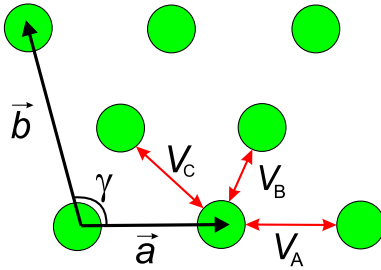
To further speed up the computations, we have calculated electronic structure and normal modes by employing the self-consistent-charge density-functional tight-binding (SCC-DFTB) method as implemented in the DFTB+ software package [199, 200]. The DFTB method is a non-orthogonal tight-binding method based on a second-order expansion of the DFT total energy expression. Thanks to a series of approximations, including the two-centre approximation and the use of minimal atomic basis sets, the elements of Hamiltonian and overlap matrices are evaluated starting from pre-computed values, so computations are about 3-4 orders of magnitudes faster using DFTB rather than DFT [200, 201].

However, DFTB cannot be used to evaluate the transfer integral, as this method resort to the use of confined orbitals, which gives a poor description of the interacting regions between the two molecules, leading to severe underestimations of the transfer integral itself [202–206]. The proposed solution to this problem, a case-by-case recalibration of additional diffuse basis set in DFTB [202, 203], would not be convenient for the study of a large variety of materials. For that reason the transfer integrals were

evaluated at the B3LYP/3-21g* level of theory as implemented in Gaussian 09 [207]. ∇V has been evaluated by using the finite-difference 2-point approximation, using displacement of ± 0.01 Å. To construct the Hessian matrix P_{ij} needed to evaluate intermolecular modes (see part II), the second derivative of the energy has been evaluated numerically by performing single-point DFTB+ calculation on a supercell in which the molecule of interest is distorted along the rigid molecular displacements, in the presence of periodic boundary conditions (PBC). The supercell size is chosen so that in presence of PBC the molecule of interest is not in van der Waals contact with its repetition.

In Table 8.1 we report the transfer integral (V), the norm of the transfer integral gradient ($|\nabla V|$) and the fluctuation of the transfer integral (σ) evaluated at $T = 298$ K for each pair in the high-mobility plane of the molecules in fig. 8.1. The crystal structure is derived from the Cambridge Structural Database (CSD) [88] and the interacting pair is identified by providing: (i) the ID of the first molecule of the pair in the reference cell (where ID is a number varying between 1 and the number of the independent molecules in the unit cell), (ii) the ID of the other molecule constituting the pair, (iii) three integers n_1, n_2, n_3, which define the translation $n_1 \vec{\nu}_1 + n_2 \vec{\nu}_2 + n_3 \vec{\nu}_3$ of the second molecule with respect to the first one (in this formalism, $\vec{\nu}_1$, $\vec{\nu}_2$, $\vec{\nu}_3$ generally designate the lattice vectors in the reference crystallographic structure).

It should be stressed that the sign of the transfer integral is related to an arbitrary phase of the orbitals involved. Nevertheless, all transfer integrals of a solid need to be evaluated consistently, e.g. once a phase is chosen for an orbital, all transfer integrals must be reported with that phase. The phase-consistency is of paramount importance, since electronic properties like band structure or charge mobility strongly depend on the relative transfer integral sign [54]. Here we have arbitrarily selected the phase, paying attention that it is identical for orbitals on translationally invariant molecules and we report one of the correct sign combinations (the

Table 8.1. List of pairs in the high-mobility plane for molecules in fig. 8.1 and relative values for: V, $|\nabla V|$ and σ at 300 K. The molecules constituting each pair are identified as explained in the main text. Reference values from: [a] ref. 161; [b] ref. 159; [c] ref. 55; [d] ref. 177.

Molecule & CSD code	Label	ID_1, ID_2, n_1, n_2, n_3	V (meV)	$|\nabla V|$ (meV/Å)	σ (meV)	σ (meV) other works
An (599019)	A	1, 1, 0, −1, 0	−61.2	176	14.6	10-11[a]
	B	1, 2, −1, −1, −1	+35.1	724	41.4	20-21[a]
Tn (IUCr A03426)	A	1, 1, 0, −1, 0	+3.60	180	17.2	14-16[a]
	B	1, 2, 0, 0, 0	+18.9	375	22.8	19-21[a]
	C	1, 2, −1, 0, 0	−70.4	301	21.4	17-18[a]
Pn (1230799)	A	1, 1, −1, 0, 0	+22.3	142	13.1	14-15[b]
	B	1, 2, 0, 0, 0	−77.5	218	23.9	24-28[b]
	C	1, 2, −1, 0, 0	+40.2	249	22.7	22-24[b]
Rb (605647)	A	1, 1, −1, 0, 0	+140	289	46.3	49[c]-51[d]
	B	1, 2, 0, 0, 0	−19.5	124	18.7	9.7[c]-9.9[d]
Pc (1319885)	A	1, 1, 0, −1, 0	+115	217	17.9	
	B	1, 2, 0, 0, 0	−89.8	527	24.1	
	C	1, 2, 1, −1, 0	−81.8	526	27.8	
BTBT (975935)	A	1, 1, 0, −1, 0	+119	1222	46.7	
	B	1, 2, 0, 0, 0	−23.4	808	43.2	
DTTTF (1236389)	A	1, 1, 0, −1, 0	+114	1134	84.2	
	B	1, 2, −1, −1, 0	−55.0	537	87.5	
DNTT (644240)	A	1, 1, −1, 0, 0	+131	197	15.2	
	B	1, 2, −1, 0, 1	−146	712	53.7	
DBTDT (1236389)	A	1, 1, 0, 0, −1	+15.5	124	9.47	
	B	1, 3, −1, 0, 1	−20.8	208	12.6	
	C	1, 3, 0, 0, 0	−68.1	245	14.4	
DPA (113041)	B	1, 3, −1, 0, 0	+36.9	190	11.5	
	C	1, 2, 0, 0, 0	−44.9	199	13.3	
TIPS (172476)	A	1, 1, 0, −1, 0	+3.01	33.1	12.3	
	B	1, 1, −1, 1, 0	+45.3	762	101	
	C	1, 1, −1, 0, 0	+45.3	1147	144	
C8-BTBT (679293)	A	1, 1, −1, 0, 0	+70.2	1464	148	
	B	1, 2, −1, −1, 0	+70.2	1616	306	
	C	1, 2, 0, 0, 0	−9.65	448	71.2	

other can be derived trivially from eq. 5.15).

As discussed in the methods part (eq. 5.15), the transfer integrals values have been evaluated starting from the Fock operator of the dimer system, while a more popular approach involves the use of the Fock matrix built starting from the density matrix of the non-interacting monomer. However, as shown in fig. 8.3, a comparison between the transfer integrals obtained using these two approaches for pentacene, rubrene and tetracene leads to almost negligible differences (less than 5% with correlation coefficient between the two calculations $r^2 = 0.995$). Moreover, additional tests using
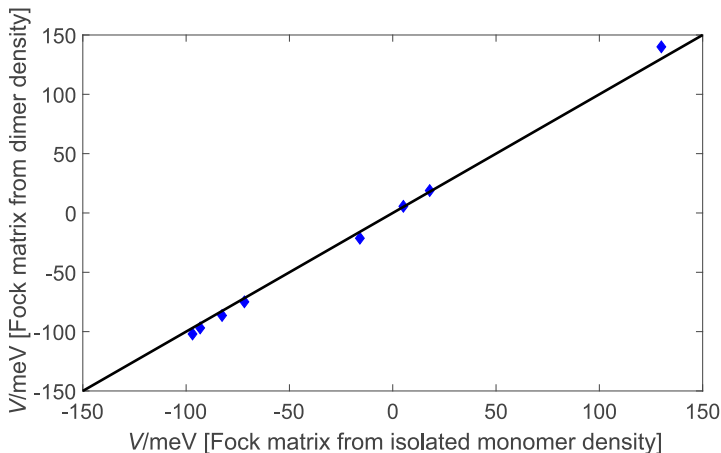
Figure 8.3. Scatter plot showing V obtained starting from the density matrix of the dimer vs. V obtained starting from the density matrix of the non-interacting monomer for pentacene, rubrene and tetracene.

the methodology proposed in ref. 208, resorting to the transformation of the Fock matrix extracted from adiabatic first-principle calculations, also give consistent results, ensuring the validity of our approach (ref. 87).

In general, our transfer integral values show a good agreement with results obtained with the latter approach and reported in the literature [2, 19, 209], except for rubrene, for which smaller values have been reported using different approximate methodologies [2, 209, 210].

Then, we have tested the sensitivity of the transfer integral to the density functional and basis set used. As shown in fig. 8.4, where we compare the transfer integrals for the molecules studied using different functionals and basis sets (B3LYP/3-21g*, B3LYP/6-31g*, B3LYP/6-311g** and PBE/6-31g*), we get very similar values, as expected.

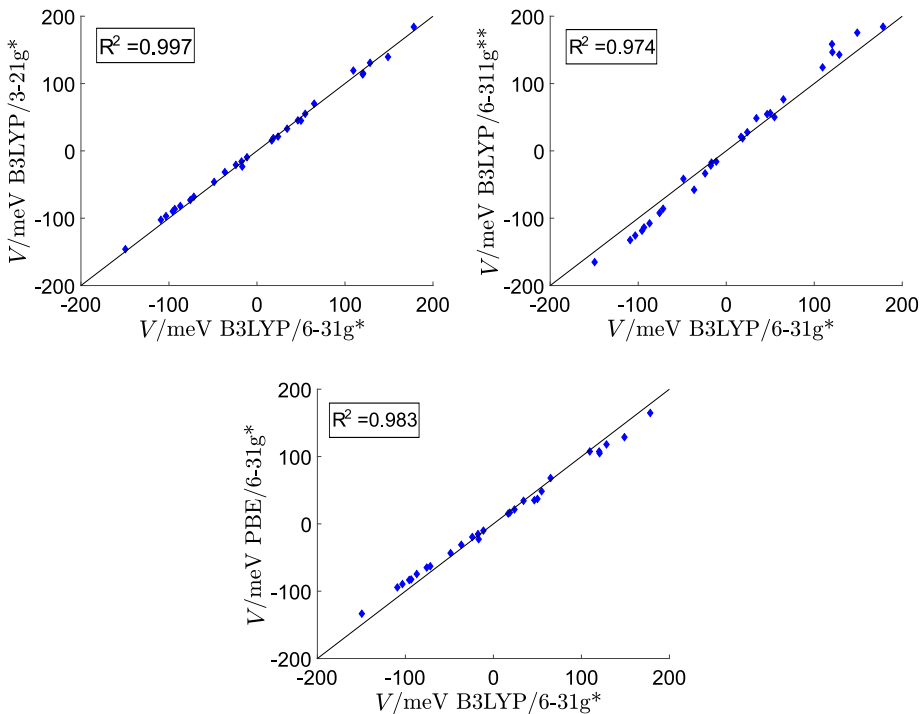Figure 8.4. Comparison between transfer integrals for the molecules shown in fig. 8.1 obtained with B3LYP/6-31g* vs. B3LYP/3-21g* (top left), B3LYP/6-311g** (top right) and PBE/6-31g* (bottom), respectively.

In addition, the little variations shown in fig. 8.4 do not affect the mobility evaluated through the transient localization approach, since it only depends on the relative magnitude and sign of the coupling [54]. For these

reasons, we have computed transfer integrals and their gradients (∇V) using the cheapest method (B3LYP/3-21g*), in order to develop a less time-consuming protocol, more suitable for the analysis of big databases. Indeed, the evaluation of the gradient of transfer integral is a computationally intensive step, requiring $12 \times N_A$ single-point calculations (N_A being the number of atoms in one molecule). For consistency, even if the evaluation of the transfer integrals themselves is rather fast, we decided to compute them at the same level.

In our last test, we checked the accuracy of the approximate modes used for the computation of the nonlocal electron-phonon coupling, by defining a spectral density,

$$B_{ij}(\omega) = \frac{1}{2\hbar} \sum_M g_{ij,M}^2 \delta(\omega - \omega_M), \tag{8.1}$$

in which the squared non-local electron-phonon coupling weights the contribution of each mode in the spectrum of frequencies [211]. In our numerical analysis, the Dirac δ function is replaced by a finite broadening (a Gaussian distribution with a width of 5 cm^{-1}).

We have evaluated B_{ij} for the couple of Tn and Rb showing the largest total fluctuation (i.e. Tn dimer B and Rb dimer A) and compared it with the spectral density obtained with a more accurate approach incorporating the effect of phonon band dispersion (kindly provided by the authors of ref. 55). In light of the rather severe approximations introduced, we have a quite good agreement between the two methods (fig. 8.5), ensuring the reliability of our approach.

Finally, when comparing the room temperature fluctuation of the transfer integral (eq. 5.5) obtained with the two approaches, we notice that they lead to quite similar results (see table 8.1), within 15 %, suggesting that, at least for rigid molecules, our very approximate crystal vibrations are acceptable. We have also reported in the same table σ values computed by other groups with other methods at a similar level of approximation [159, 161], and the results are reassuringly consistent.
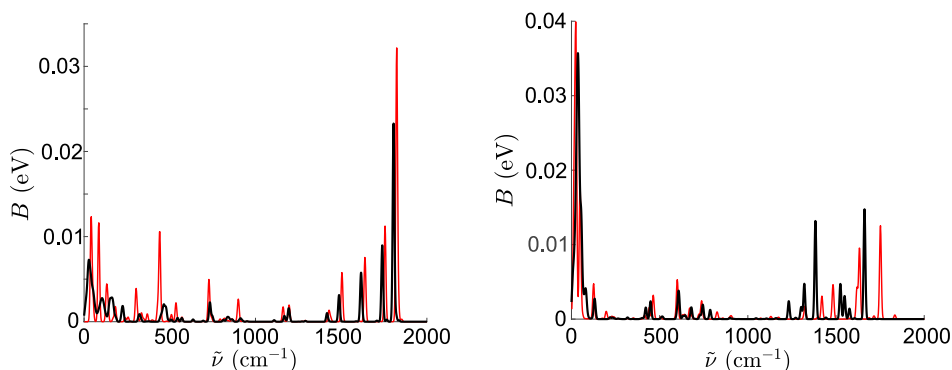
Figure 8.5.   Total spectral density B_{ij} for Tn dimer B (left) and Rb dimer A (right). Black line: our results, red line: data from ref. 55.

Up to now we have shown that our results are in good agreement with the data available in the literature obtained with other approaches. Given its reliability, we conclude that our approximate methodology can be used in the field of material discovery, exploring a range of materials to look at the value of their non-local electron-phonon coupling. The strength of our approach resides in the computation of the phonons, which represents the slow step in other approaches (up to several months required); using our approximations it can be performed on a time scale comparable to the evaluation of the gradient of transfer integral, so that the computations of V, ∇V and σ takes about 2-3 days for each system studied (using 16 Intel Sandbridge processors). Unfortunately, because of the severity of our approximations, the methodology developed leads to rather inaccurate values when applied to molecules containing highly flexible fragment, like the two alkyl chains in C8-BTBT. Indeed, the non-local electron phonon coupling is probably overestimated in such molecules, since large amplitude vibrations of the isolated molecule are strongly affected by the crystal field (shifted at higher energy and reduced in amplitude) an effect that is not described by the current version of our method.

In the following, we will focus on the identifications of some general trends and relations among the quantities in table 8.1, since, to the best of our knowledge, this is the first time that the non-local electron-phonon coupling has been evaluated for such a relatively large set of molecules. First of all, it is widely recognized that good semiconducting materials should have both high transfer integrals and a low degree of disorder, but, on the basis of the small number of molecules studied up to now, it was believed that the relative fluctuation $\sigma/|V|$ should be around 0.5 at room temperature [54]. On the contrary, our analysis points out that σ and V values are essentially uncorrelated, as one can see from the scatter plot and the histogram illustrating the distribution of $\sigma/|V|$ in fig. 8.6. This is
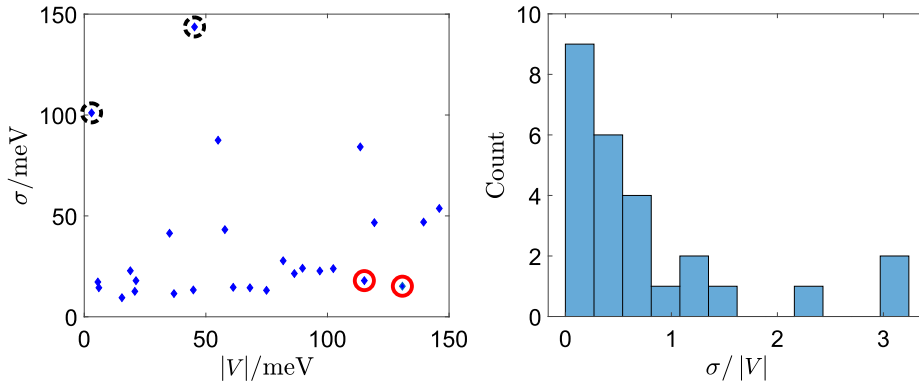
Figure 8.6. Scatter plot showing σ vs. absolute value of V (left) and histogram of $\sigma/|V|$ (right) for all the couples reported in Table 8.1. Black dashed circles identify TIPS values, red full circles identify DNTT-A and Pc-A values. The rather high $\sigma/|V|$ for TIPS is not reported in the histogram for convenience.

of paramount importance, since it suggests the existence of a quite large range of $\sigma/|V|$; in other words, the dynamic disorder is not unavoidable, pointing towards the possibility for the development of materials where it is substantially smaller. Another consequence of this point is that research should not focus on materials showing only high transfer integrals, but

rather on those having a low $\sigma/|V|$ since a high transfer integral alone does not ensure good semiconducting properties. Narrowing this discussion down to the molecules under examination, TIPS (black dashed circles in fig. 8.6), which shows the highest values of $\sigma/|V|$ for all the interacting couples, has the lowest experimental mobilities reported among the molecules in fig. 8.1 (0.6 cm^{2}V^{-1}s^{-1} [54]). On the contrary, a low ratio $\sigma/|V|$ is found for high mobility materials, e.g. DNTT and Pc, with experimental mobilities up to 8.3 cm^{2}V^{-1}s^{-1} and 9.0 cm^{2}V^{-1}s^{-1} respectively [60, 212].
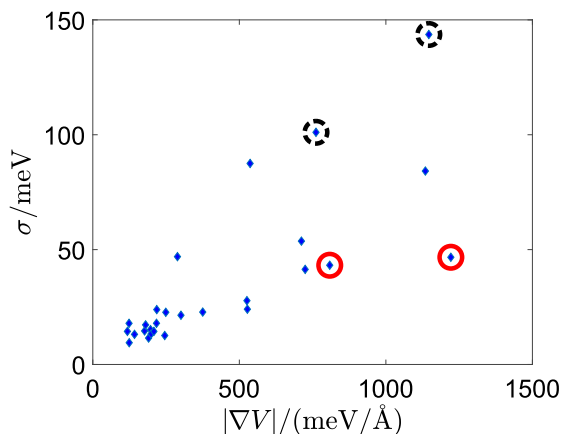
Figure 8.7.   Scatter plot showing σ vs. $|\nabla V|$ for all the couples reported in Table 8.1.   Black dashed circles highlight TIPS values, while red circles identify BTBT values.

Another interesting analysis based on the data in table 8.1 allows to verify if σ is mainly affected by the strength of the transfer integral gradient (∇V) or by the polarization of the phonons ($\mathbf{Q}_M$). Fig. 8.7 shows a correlation between σ and $|\nabla V|$, suggesting that ∇V is the main contributor to the total σ, at least for low values. Indeed, as can be inferred from σ definition itself (eq.s 5.5 and 5.16), small $|\nabla V|$ are always associated with small disorder, while larger σ are also affected by phonon polarization (in fig. 8.7 we highlighted two molecules, BTBT (red circles) and TIPS (black

dashed circles), showing quite similar $|\nabla V|$ but very different σ).

The implications of this analysis on material discovery is that, since we are only interested on materials showing low disorder, for which there is an excellent correlation between σ and $|\nabla V|$, it is possible to identify promising materials using $|\nabla V|$ rather than σ, with the advantage that the former is cheaper to compute and it does not depend on vibrational properties of the solids.

To better understand why materials with similar $|\nabla V|$ have very different σ, such as BTBT and TIPS, we graphically represent the gradient of transfer integral and the phonon displacements ($\mathbf{Q}_M$), whose scalar product defines the non-local electron-phonon coupling (eq. 5.16). Those two quantities are reported in fig. 8.8 as a set of green ($\mathbf{Q}_M$) and red (∇V) arrows centred on the corresponding atom for the mode showing the highest contributions to total σ for BTBT-A ($\omega = 58$ cm^{-1}) and TIPS-C ($\omega = 15$ cm^{-1}). It is evident that, for BTBT, the gradient of transfer integral is virtually orthogonal to the direction of phonons, leading to a rather low σ despite the quite high value of $|\nabla V|$ (see Table 8.1). On the other hand, for TIPS, the molecule showing the highest value of σ, there is a considerable overlap between the mode displacements and the transfer integral gradient. In this way the effect of phonon direction on the fluctuations of transfer integral can be explained; however the design of materials having the desired phonon characteristics is virtually impossible because accurate computations are extremely time-consuming, as previously discussed.

The analysis we have conduced so far can be summarized in the idea that, in order to design better semiconducting materials, the ratio $|\nabla V|/|V|$ should be kept as low as possible. In that respect it would be very useful the development of an intuitive understanding of what makes the transfer integral less sensitive to the nuclear motion. Usually researchers focus on the intermolecular geometries that maximize the transfer integrals [77], but, as discussed above, a better property to be studied is $|\nabla V|/|V|$. For that reason we propose the construction of a map of the ratio $|\nabla V|/|V|$
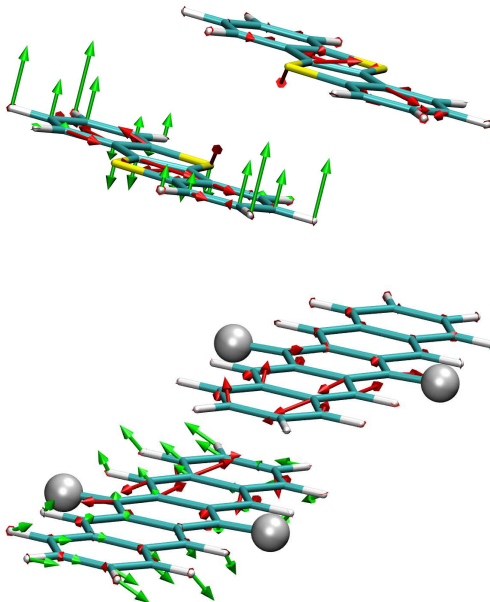
Figure 8.8.   Superposition of the gradient of the transfer integral (red arrows) and the displacements (green arrows) for the mode showing the greatest contribution to the total σ for: BTBT-A (top) and TIPS-C (bottom), where the Si atoms and the alkyl chains, which have almost zero values of ∇V, are replaced by a gray sphere. Note that the displacements are shown only on one molecule since in our approach the crystal vibrations are localized on one molecule.

to investigate which mutual molecular configurations are less susceptible to dynamic disorder and why. As an example, we have computed $|\nabla V|$ and $|V|$ for various relative positions of two molecules in the DNTT-A couple, chosen because of its low $|\nabla V|/|V|$ value. In practice we start from the crystallographic geometry ($\Delta x = \Delta y = \Delta z = 0$) and translate one molecule with respect to the other along the molecular axis Δx in fig. 8.9. As shown in the figure, $|\nabla V|$ and $|V|$ seem to follow independent behaviours, i.e. there is no relation between the maxima of $|V|$ and the value of $|\nabla V|$. For this reason, in the interval 1 Å$< \Delta x <$7 Å, where the molecules have a good
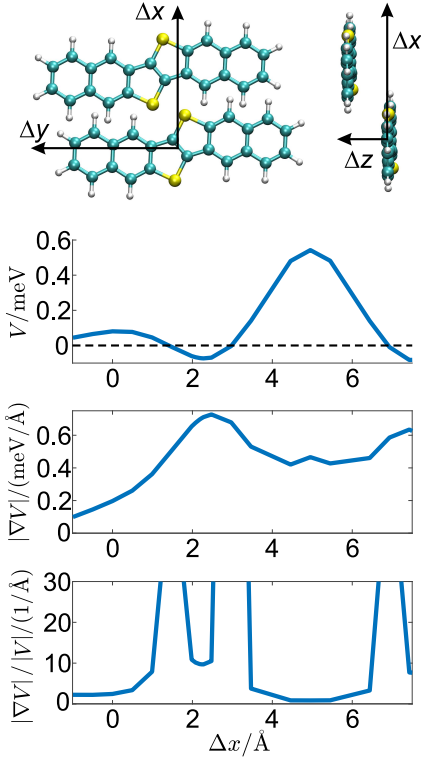
Figure 8.9. Top: reference frame for the relative shift of the two DNTT molecules. Below, a plot showing: values of V (top), $|\nabla V|$ (middle) and $|\nabla V|/|V|$ (bottom) for different relative positions of the two molecules in the DNTT-A couple. As shown on the top reference frame, positive Δx values mean that the molecules are rigidly shifted towards the direction in which they are closer than at the experimental geometry.

overlap, $|\nabla V|/|V|$ is small when $|V|$ is large, i.e. 4.5 Å $< \Delta x < 5.6$ Å. This area could have been identified simply following the popular idea of maximizing the transfer integral [77], but another interesting region occurs when the overlap between the two molecules is limited to only few atoms, e.g. for $\Delta x < 1$ Å. This area could not have been identified only on the basis of the maximization of the transfer integral, since this time $|\nabla V|/|V|$ becomes

small because $|\nabla V|$ is smaller (fewer atoms are involved in the transfer integral and the displacement of the atoms not involved does not influence it). This analysis suggests that molecular crystals displaying arrangements where molecules interact through their edges could be of potential interest and should be further investigated since they can have small non-local electron-phonon couplings.
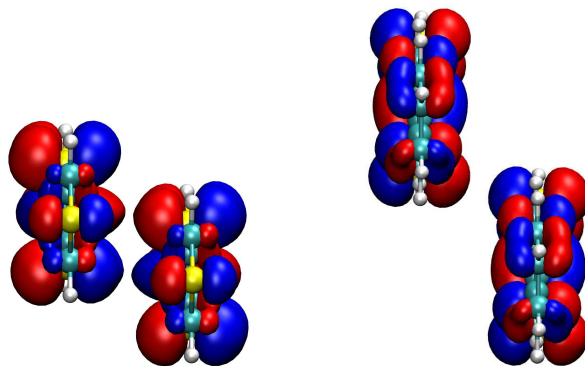
Figure 8.10.   Side view of DTTTF-A (left) and DNTT-A (right) HOMO orbitals.

It is interesting to notice that our investigation could explain the difference between DTTTF-A and DNTT-A, two of the molecules under examination, which possess similar V values but significantly different $|\nabla V|$ (see Table 8.1). Indeed, in line with the analysis proposed, the two DTTTF molecules show a partial stacking, while the DNTT molecules interact through their extremities, as shown in fig. 8.10 where their HOMOs are represented.

8.1   Mobility using TLT approach

We can use the data evaluated in the previous section together with the TLT approach to evaluate the mobility for all the molecules under investigation.

As a first study, we have decided to focus on a smaller subset composed by the same four molecules (i.e. pentacene, tetracene, picene and rubrene) we have already studied in the previous chapter using Marcus, FGR and SOC approach, with the aim of making a comparison between the performances of all these models.

As outlined in the introduction, the TLT approach only allows to evaluate a mean value for the mobility, without providing the possibility of computing the variation of μ depending on the direction considered, i.e. the anisotropic mobility. Despite this limitation, a mean μ value is still of interest since it allows to compare different molecules identifying the best semiconductors. With this in mind, using eq.s 3.32 and 5.10, we have computed the mean μ for the molecules under study using TLT, FGR, SOC and Marcus (table 8.2).

Table 8.2. List of mean value of mobility $(cm^2V^{-1}s^{-1})$ obtained using different approaches for pentacene, rubrene, tetracene and picene. Experimental values from: [a] ref. 24; [b] ref. 54; [c] ref. 193; [d] ref. 212.

Molecule	TLT	SOC	FGR	Marcus	Experimental
Tn	2.35	2.21	18.7	1.76	2.4[a]
Pn	2.94	2.24	17.4	2.27	1-2.5[b]
Rb	11.8	10.7	11.1	10.2	8.6-12[b,c]
Pc	9.81	10.2	10.8	4.51	9.0[d]

We have already discussed in the previous chapter about the inapplicability of FGR to pentacene and tetracene, along with the shortcomings of the Marcus theory, so here we focus only on the comparison among SOC and TLT results. It is easy to see that TLT and SOC results are very similar, being also in good agreement with experimental results. Thus, we can conclude that both TLT and SOC approaches are adequate for the

description of charge transfer in organic semiconductors.

However, TLT approach has at least two advantages compared with SOC. First of all, it does not introduce the arbitrary assumption of a monoexponential decay used in interpolating SOC populations to get a time averaged rate constant. Moreover, TLT resorts to assumptions in line with the physics underlying CT in organic semiconductors: it takes into account the oscillations of transfer integrals, it does not require the loss of coherence after each step and it includes quantum localization corrections.

We conclude this section pointing out that, in the evaluation of μ we have assumed (eq. 5.9) $\tau_{in} = 1$ ps, a typical value for an intermolecular oscillation. However, it has been shown in ref. 54 that the dependence of the mobility on the molecular fluctuation time is weak, as illustrated in fig. 8.11, since $L^2(\tau_{in})$ increases with fluctuation time in the subdiffusive regime, which partially cancels the explicit factor τ_{in} in the denominator of eq. 5.9.
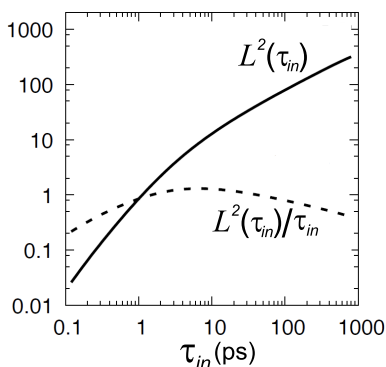
Figure 8.11. Dependence of the statistically averaged transient localisation length on the fluctuation time. Adapted from ref. 54.

113

Part IV

AN UNCONVENTIONAL OSC: THE DNA

Chapter 9

Hole Transfer in DNA

9.1 Overview

In this part we will analyze the performances of our quantum dynamics approach in the description of CT in a system quite different from molecular crystals, which we have discussed in the previous part: the DNA, a macromolecule containing the genetic information for the growth and development of all known living organisms. Despite their differences, DNA has also been identified as an organic semiconductor [213]. Indeed, even if first studies on the electrical conductivity of DNA focused on the correlation between oxidative damages and apoptosis or cancer [214–219], following research highlighted that an improvement in charge transfer efficiency could be achieved by accurately tuning its sequence or by using modified nucleobases [220, 221], observing CT for distances up to 200 Å [222–236]. In this respect, DNA has already been used for the design of sensors or as a template, by exploiting its self-assembly properties [237, 238].

In particular here we will focus on hole transfer (HT) between 2 guanines separated by several A/T bases, a process experimentally investigated by Giese [239], and Schuster [235, 240], showing how our approach allows either to quantitatively reproduce experimental data and to offer a point of view

that reconciles discordant interpretations about this phenomenon.

9.2 DNA structures and first studies

From a chemical point of view, DNA is a nucleic acid, i.e. an aperiodic macromolecule constituted by units called nucleotides. Each nucleotide
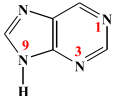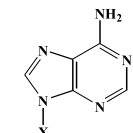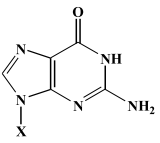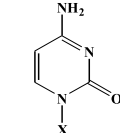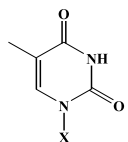
Precursor	Structure	Nucleobase X = H	Nucleoside X = Deoxyribose	Nucleotide X = Deoxyribose phosphate
purine		Adenine	Deoxyadenosine	Deoxyadenosine monophosphate
		Guanine	Deoxyguanosine	Deoxyguanosine monophosphate
pyrimidine		Cytosine	Deoxycytidine	Deoxycytidine monophosphate
		Thymine	Thymidine	Thymidine monophosphate

Figure 9.1.   Structure and nomenclature of the DNA bases.

consists in a phosphate group, a pentose carboidrate (deoxyribose or ribose) and a nitrogenous base or nucleobase. Nucleobases are classifies as purines, adenine (A) and guanine (G), constituted by two fused heterocyclic

ring derived from purine, or as pyrimidines, cytosine (C) and thymine (T), constituted by one heterocyclic ring, derived from pirimidine (fig. 9.1).

Nucleic acids are molecules formed by two chains (composed of nucleotides) that coil around each other to form a double helix [241, 242], where the nitrogenous bases of the two strands are bound together by hydrogen bonds established according to base pairing rules (A-T and G-C). The stability of the double helix structure is mainly ensured by hydrogen bonding interactions and by π-stacking, i.e. hydrofobic interactions established among by stacked pirimidines and/or purines [243].

Since the discovery of its structure [241, 242], DNA has been the subject of extensive medical and biotechnological research, in particular for its applications in nanotechnologies. In this respect, Duchesne performed the first measurements about DNA conduction properties [244] before 1960, and few years later, Eley *et al.* [245] on the basis of theoretical studies, proposed that the double-helical structure of DNA allows an efficient charge transfer in DNA thanks to π-stacking interactions. Long distance hole transfer (HT) in DNA is of paramount importance, for several reasons: chemico-physical properties of DNA under oxidative stress [218, 219], as well as its potential applications in the area of molecular electronics [213, 246–249], are strictly related to the efficiency of charge migration along the duplex.

Time resolved spectroscopical measurements and steady state analysis of oxidative damage have shown that hole transfer is able to cover distances up to 200 Å before irreversible oxidation occurs [222–236]. Oxidation usually occurs on guanine (G) the nucleobase showing the lowest oxidation potential [250–254], while HT takes place by essentially two mechanisms:

- Superexchange (fig. 9.2 a)

- Hopping (fig. 9.2 b)

A simple analysis of a donor-bridge-acceptor DNA system shows that HT mechanism is determined by the relative energy of the bridge vibronic states with respect to donor and acceptor vibronic states [255].
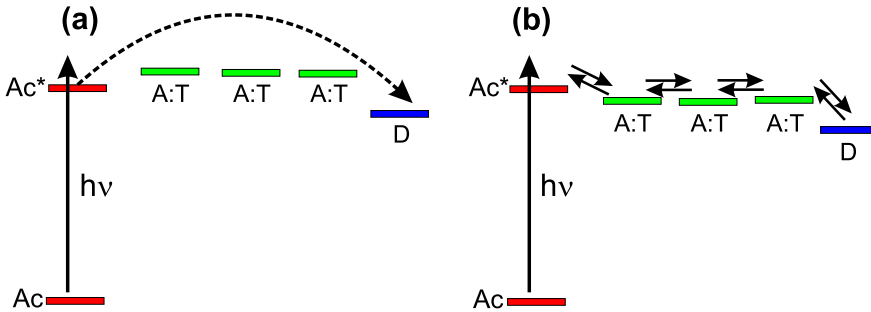
Figure 9.2. Superexchange (a) and hopping (b) mechanisms for charge transfer between excited acceptor and ground state donor separated by three A:T bases.

If bridge states have higher energy than donor states, charge migration takes place by superexchange, i.e. the hole is transferred to the acceptor in a single step, through the bridge virtual states, a process similar to Raman scattering. It is worth noting that in this process charge is never localized on the bridge.

Charge transfer rates strongly depend on distances, accordingly to Marcus-Levich-Jortner equation [256, 257]:

$$k = A \exp(-\beta R), \qquad (9.1)$$

where k is the rate constant, R is the distance between donor and acceptor, while A and β are constants whose value depends on the system studied.

On the other hand, when bridge and donor states possess almost the same energy, HT occurs through multi-step hopping, where, in contrast to superexchange, the charge is localized on the bridge states during the overall process. If each hopping step occurs across the same distance, then the overall HT rate shows a weak dependence on the number of hopping steps N_{hs} [256, 257]:

$$k \propto N_{hs}^{-\eta}, \qquad (9.2)$$

where η depends on the system studied (usually $1 \leq \eta \leq 2$).

120

9.3   Experimental works

In the following we will briefly describe two experimental results, which disagree on the conductivity of some DNA sequences, showing in the next section how our simulations lead to an interpretation that can reconcile them.
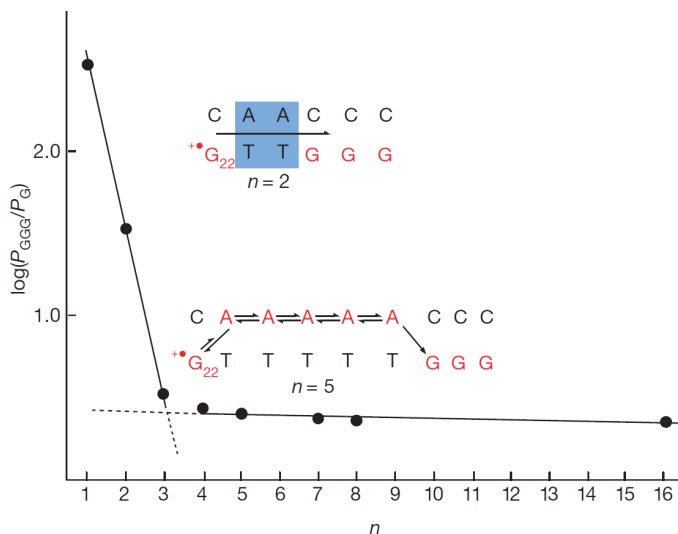
Figure 9.3. $\ln(P_{GGG}/P_G)$ vs. number n of A:T bases (reproduced from ref. 239). The ratio (P_{GGG}/P_G) is proportional to charge transfer rate. The steepest line identifies superexchange intra-strand mechanism with a slope $\beta = 0.6$ Å^{-1} ([239]) interpolated with the Marcus-Levich-Jortner [256] equation. The flat line identifies inter-strand charge transfer (see Results section).

The first experiment was conducted by Giese's group [239]. They measured the efficiency of photoinduced charge transfer in DNA double strands where one strand is $G(T)_n GGG$ with $1 \leq n \leq 16$ and the other strand is the complementary strand; the hole was initially located on the first guanine. The product ratio P_{GGG}/P_G, a measure of the HT rate along the strand compared with the rate of nucleobase oxidation, was determined for

different n. For short bridges, up to $n = 3$, HT efficiency dropped by a factor of 8 for each additional A:T step; in longer sequences, for $n = 4$-7, the $P_{\mathrm{GGG}}/P_{\mathrm{G}}$ ratio exhibits a much weaker distance dependence; finally for $n = 7$-16, no change in the $P_{\mathrm{GGG}}/P_{\mathrm{G}}$ has been observed.

These results have been interpreted in terms of a switch of HT mechanism from intra-strand superexchange for shorter distances to an inter-strand mechanisms for bridges constituted by more than three thymines [239].

However, these data are somewhat in disagreement with later experimental results [235, 240] reported by Schuster *et al.*, who studied the one-electron oxidation of seven DNA oligonucleotides, shown in figure 9.4. We

|																												
DNA(1)	5'- *A	A	A	C	G	C	G	C	G	C	G	C	A	A	A	T	T	-3'										
	3'- T	T	T	G	C	G	C	G	C	G	C	G	T	T	T	A	A	AQ	-5'									
DNA(2)	5'- *A	A	A	T	G	T	G	T	G	T	G	T	A	A	A	T	T	-3'										
	3'- T	T	T	A	C	A	C	A	C	A	C	A	T	T	T	A	A	AQ	-5'									
DNA(3)	5'- *A	A	A	T	G	G	T	G	T	G	T	G	T	G	T	G	G	T	A	A	A	T	T	-3'				
	3'- T	T	T	A	C	C	A	C	A	C	A	C	A	C	A	C	C	A	T	T	T	A	A	AQ-5'				
DNA(4)	5'- *A	A	A	C	G	G	C	G	C	G	C	G	C	G	C	G	G	C	A	A	A	T	T	-3'				
	3'- T	T	T	G	C	C	G	C	G	C	G	C	G	C	G	C	C	G	T	T	T	A	A	AQ-5'				
DNA(5)	5'- *A	A	A	T	8	G	T	G	T	G	T	G	T	G	T	G	G	T	A	A	A	T	T	-3'				
	3'- T	T	T	A	C	C	A	C	A	C	A	C	A	C	A	C	C	A	T	T	T	A	A	AQ-5'				
DNA(6)	5'- *A	A	A	C	8	G	C	G	C	G	C	G	C	G	C	G	G	C	A	A	A	T	T	-3'				
	3'- T	T	T	G	C	G	G	C	G	C	G	C	G	C	G	C	C	G	T	T	T	A	A	AQ-5'				
DNA(7)	5'- *A	A	A	T	8	G	T	G	T	G	T	T	T	T	G	T	G	T	G	G	T	A	A	A	T	T-3'		
	3'- T	T	T	A	C	C	A	C	A	C	A	A	A	A	C	A	C	A	C	C	A	T	T	T	AA	AQ-5'		

AQ-DNA

8-oxo G (8)
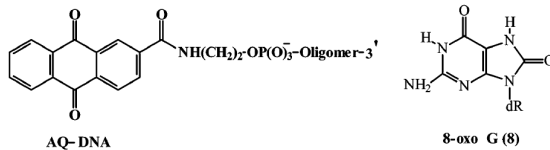
Figure 9.4. Structures of the DNA oligomers studied in ref. 240 (reproduced from there).

focus our attention on the last oligomer, that presents a thymine bridge similar to Giese's oligomers. In this one, the hole was initially located on the antraquinone moiety but, even if the 8-oxo guanosine is an easier site to

oxidize, the damage was experimentally found only on the GG step near the anthraquinone. The authors concluded that "the 4 thymines sequence introduces a sufficiently high barrier that the radical cation [. . .] is prevented from falling into the deep 8-oxoG trap" [240].

In summary, while in Giese's experiment it is evident that the thymine bridge does not act as a barrier for hole transfer, Schuster's data for an oligomer showing the same bridge indicate that the charge cannot migrate beyond a 4-thymines moiety.

9.4 Results

We have applied our quantum dynamics methodology (see part II) to Giese's experiment trying to reproduce the distance dependence of hole transfer (HT) in ds-$G(T)_n$GGG oligonucleotides. Hole site energies and electronic couplings used in the dynamics are reported in Table 9.1. All values have been obtained by our group through DFT computations including both the sugar-phosphate ionic backbone and the effects of the aqueous environment, see ref. 258 for details; moreover they are in good agreement with experimental voltammetric and spectroelectrochemical data [259–262].

Table 9.1. Hole site energies (E_Y, eV, relative to the G/G^+ pair) and electronic coupling parameters for base-base interactions (V_{YX}, eV). All values have been obtained by DFT computations published in ref. 258 and in good agreement with experimental observations [251, 252, 263].

Y	E_Y	V_{YG}	V_{YA}	V_{YC}	V_{YT}
G	0.00	0.09	0.16	0.23	0.16
A	0.43	0.12	0.24	0.15	0.09
C	0.68	0.25	0.18	0.12	0.13
T	0.70	0.13	0.08	0.09	0.12

As explained in part II, in order to reduce the basis set considered in the dynamics, we first analyze the equilibrium position displacements upon oxidation of the redox half-pairs G/G^+, A/A^+, C/C^+ and T/T^+. The

components of the **K** vectors, c.f. eq. 4.11, which are by far the quantities playing a major role in determining the value of the effective couplings between vibronic states, are reported in Table 9.2 for the four redox half-pair G/G^+, A/A^+, C/C^+, and T/T^+, together with their contribution to the total reorganization energy, evaluated by using harmonic approximation.

Inspection of Table 9.2 show that more than 80% of the reorganization energy arises from a subset of 13, 8, 8 and 6 normal modes of G, A, C and T, respectively. Thus, a model including only those modes should provide a qualitatively correct picture of the HT dynamics [264, 265]. Furthermore, due to the high frequency of the most displaced vibrations with respect to the thermal quantum at room temperature, we can neglect any temperature effect and assume that the system is initially in its vibrational ground state.

Table 9.2. Wavenumbers (ω, cm^{-1}), intramolecular reorganization energies (E_r, cm^{-1}), and equilibrium position displacements (**K**, absolute values Å uma$^{1/2}$) of the most displaced normal modes of G/G^+, A/A^+, C/C^+ and T/T^+ redox pairs. Electronic calculation at the B3LYP/6-31+g(d,p) level, PCM, water solvent.

G/G$^+$			A/A$^+$			C/C$^+$			T/T$^+$		
ω	E_r^a	**K**	ω	E_r^a	**K**	ω	E_r^a	**K**	ω	E_r^a	**K**
338	76	0.21	724	88	0.106	348	27	0.39	394	90	0.20
435	223	0.28	1328	83	0.056	500	32	0.36	536	127	0.17
477	80	0.15	1143	83	0.065	574	187	0.81	709	93	0.11
521	166	0.20	1353	204	0.087	1043	123	0.49	1320	449	0.13
528	78	0.14	1367	84	0.055	1244	194	0.56	1363	139	0.071
1230	75	0.058	1510	424	0.11	1277	87	0.37	1590	675	0.13
1366	85	0.055	1622	109	0.053	1361	107	0.40			
1403	121	0.064	1639	167	0.065	1506	87	0.34			
1435	90	0.054									
1477	259	0.089									
1526	80	0.048									
1639	488	0.11									
1742	160	0.06									
$E_{r,tot}^b$ 2249			1658			1121			1937		

^{a} Computed by harmonic approximation from **K** components. ^{b}From electronic computations.

Quantum dynamics simulations have been performed on the oligomers

Table 9.3. Transition times (ps) at different levels of approximation for HT in ds-G(T)$_n$G oligonucleotides. s is the number of simultaneously excited modes and m_s denotes the maximum vibrational quantum number used for the s-th subspace.

		Intra-strand				Inter-strand				
s	m_s	T	TT	(T)$_3$	(T)$_4$	A	AA	(A)$_3$	(A)$_4$	(A)$_5$
1	5	0.78	9.1	107	1270	35	58	90	134	191
1	6	0.77	9.1	108	1270	35	58	89	134	190
2	5 3	0.55	4.9	44.2	395	31	44	53	55	52
2	5 4	0.54	4.9	43.8	390	31	44	53	54	51
3	5 3 2	0.54	4.7	39.2	339	30	42	49	48	46
3	5 3 3	0.53	4.5	37.8	315	30	42	49	48	

reported in table 9.3 for different choices of the Hilbert subspaces, defined in eq. 4.10. The computed transition times, taken at complete depopulation of the initial state, are reported in table 9.3. A satisfactory convergence is reached by including in calculations subspaces up to order $s = 3$, and using $m_1 = 5$, $m_2 = 3$, $m_3 = 2$, where m_s denotes the maximum vibrational quantum number used for the s-th subspace. We notice that by employing local vibrational eigenstates the number of basis functions to reach convergence is very small.

Our computations predict that for G(T)$_n$G the intra-strand HT transition time drops by a factor of ≈ 8.4 for each additional T, in very good agreement with the experimental results for shorter, $n = 1$-3, oligonucleotides. The process which takes place is a genuine superexchange, inasmuch as the charge is never localized over the T bridge. The logarithmic plot of the computed transition times against the distance between the D/A nucleobases yields a straight line, whose slope leads to $\beta = 0.63$ Å^{-1} of the Marcus-Levich-Jortner equation [256], to be compared with $\beta = 0.6$ Å^{-1}

obtained experimentally. Up to $n = 3$, simulations are in excellent agreement with the experimental results. It is worth noting that in ref. 239 only experimental chemical yield product ratio P_{GGG}/P_G are given. However, it has been shown by Bixon et al. [134] that, since the water-trapping rate for the holes in GGG is much larger than back charge transfer rate, it is possible to write the P_{GGG}/P_G as the ratio of the hole transport rate k_{HT} and the trapping rate k_{tr} , i.e. $P_{GGG}/P_G \approx k_{HT}/k_{tr}$. Since it is reasonable to assume that k_{tr} is the same for different oligomers, we are allowed to compare the change in k_{HT} for different oligomers with the variation of P_{GGG}/P_G for the same oligomers reported in ref. 239.

Noteworthy, the results show that the expansion (4.10) of $\Psi(t)$ exhibits good convergence properties, especially for the fastest processes. For $n = 1$ the computed transition time τ is 0.77 ps by considering only subspace S_1, decreasing to 0.54 and 0.53 ps by including subspaces S_2 and S_3, respectively. For slower processes the achieved convergence is less stringent, see Table 9.3.

For $n = 4$ the predicted HT rate lines up with those for $n = $ 1-3 in the logarithmic plot of the computed transition times against the tunneling distance, see green squares in fig. 9.5, in contrast with the clear change in the slope experimentally observed. We have thus also considered the possibility of inter-strand hole transfer mediated by the A bridge of the complementary strand, as originally proposed by Giese [239]. The inter-strand coupling element for G-A has been set to 100 cm^{-1}.

Transition times for the inter-strand HT are reported in Table 9.3. Inter-strand HT is significantly slower than intra-strand one up to $n = 2$ and becomes about one order of magnitude faster for $n = 4$. That behaviour is clearly due to the establishment of a hole delocalized domain over the A tract: the high value found by electrochemical measurements for the V_{AA} electronic coupling element, see Table 9.1, makes the electronic energy of a hole delocalized over a domain consisting of four or more consecutive A
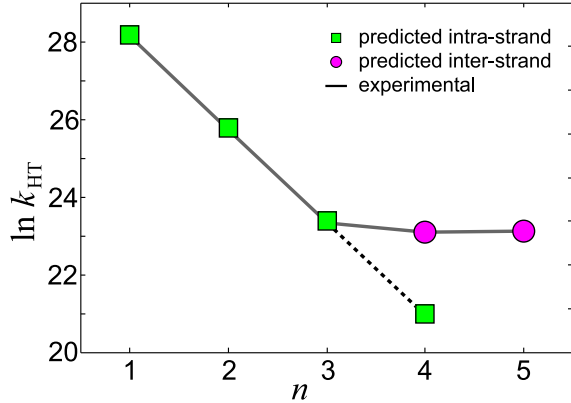
Figure 9.5. Predicted rate constants ($k_{HT} = 1/\tau$, τ being the transition time in ps) for the HT in ds-G(T)$_n$G plotted as a function of the number of thymine spacers separating the donor and the acceptor G sites. Green squares: intra-strand, violet circles: inter-strand HT via the (A)$_n$ bridge of the complementary strand. We have rescaled the experimental values, keeping fixed their slope, as justified in the main text.

nucleobases quasi degenerate with that of a hole localized on a single G nucleobase. The formation of such charge delocalized domains not only speeds up coherent HT processes, but makes also hopping an energetically possible mechanism. Our computations do not predict substantial population of the electronic states of the A tract, neither for $n = 4$ nor for $n = 5$, but energy fluctuations, even those of the order of thermal quantum [266, 267], can lead to substantial population of the A bridge electronic state [268, 269], leading to coexistence of coherent and incoherent processes [270].

Noteworthy, the establishment of hole delocalized domains over the A-rich complementary strand makes HT rates independent of distance even for a coherent process: for ds-G(T)$_5$G the predicted HT rate is slightly higher than in ds-G(T)$_4$G. Oscillations in the length dependence of charge transport has been indeed observed in atomic wires [271] and in single DNA molecules directly bridged to two electrodes [270]. In A-rich oligomers, HT rates show indeed oscillatory behaviour, with a period of 4-5 base pairs.[272,

273]

In light of our excellent agreement with Giese's experimental results, our next step is the study of Schuster's oligomer, with the final goal of finding an explanation reconciling the experimental observations of both groups, which, as outlined in the previous section, do not agree about the behaviour in HT of double strands where two G bases are separated by a bridge formed by four thymines. In order to do this, we focused on the main difference between the oligomers studied by the two groups, i.e. the different number of guanine sites. Indeed, we suggest that tunneling becomes extremely slow in oligomers containing several guanine sites ahead of the thymine bridge, because the charge tends to bounce among them rather than crossing the bridge.

To check this hypothesis, we studied the three oligomers in table 9.4, which are simply obtained by repeatedly adding a guanine-thymine couple on both ends of Giese's oligomer (GT_4G). Inspection of table 9.4,

Table 9.4. Time (ps) required to have a sum of damages over all the bases beyond the thymine bridge of 10%.

	GT_4G	$GTGT_4GTG$	$GTGTGT_4GTGTG$
intra-strand	80	320	>1000
inter-strand	10	40	50

which reports the time required for the total amount of damage located on all the G bases beyond the thymine bridge to be 10%, shows that the charge transport is faster if it occurs inter-strand i.e. involving the A bases on the complementary strand, as it could have been anticipated from our previous analysis of Giese's oligomers (table 9.3). More importantly, the time significantly increases when passing from Giese's $G(T)_4G$ to $GTG(T)_4GTG$, further increasing when considering Schuster's oligomer. We have studied $GTG(T)_4GTG$ as an intermediate between Giese's and Schuster's oligomers, to show that a significant increase in transition times
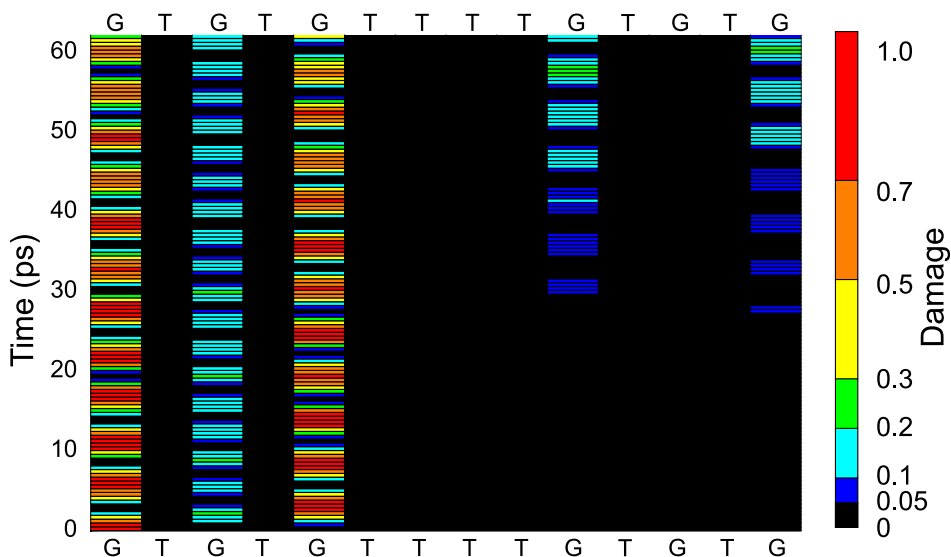
already occurs when two Gs are near.

Figure 9.6.   Time evolution of hole initially localized on the leftmost
G in Schuster's oligomer. As outlined by the legend in the figure, a red
square means that at this time the damage fraction on the molecule is
between 0.7 and 1.0, etc.

To gain deeper insight about this peculiar behaviour, we have reported
in fig. 9.6 the time evolution of the population for an hole initially localized
on the leftmost guanine in Schuster's oligomer. We can easily notice that
at the beginning and for a quite long time, the charge goes back and forth
among the three Gs ahead of the thymine bridge before any fraction of dam-
age on the Gs beyond can be observed. In other words, the bridge crossing
may occur only on timescales maybe not consistent with the experimental
time range, thus explaining why in ref. 240 no damage is observed at the
final 8-oxoG step.

In summary, from our data we can conclude that the T_4 bridge is not
a barrier for charge transfer itself. The different behaviour observed by the
two groups is related to the fact that, in Schuster's experiment the charge

does not cross the bridge because it bounces between nearest guanine sites, an effect that cannot take place in Giese's oligomers where there are no Gs close to each other.

Part V

CONCLUSIONS

Chapter 10

Conclusions

Organic semiconductor-based electronic devices have raised great expectations because of their novel material properties and favorable economic synthesis and processing. Substantial experimental effort has been devoted to the identification of better semiconductors (i.e. those showing higher mobilities) suitable for everyday applications. Despite the intense research effort, new OSCs have usually been discovered by trial and error and, even retrospectively, it was not always possible to explain why some materials exhibit better performances than others. However, in light of the difficulties, slowness and high cost of experimental synthesis and characterization of new semiconductors, a more efficient approach is now required, and, in thie respect, the use of computer-aided material discovery can be important to accelerate the pace of organic semiconductor discovery. Unfortunately, progresses in this area have been slowed down because of the active debate about the most appropriate theoretical approach to model charge transport in these materials.

In this thesis we have described and applied five among the most used theoretical approaches for the description of CT in organic semiconductors: the Marcus theory, the Fermi Golden Rule (FGR), the Second Order Cumulant expansion of the density matrix (SOC), the quantum dynamics, and

a recently developed approach, the Transient Localization Theory (TLT). Along with this analysis, substantial effort has been devoted to the development of two approximate strategies that ensure a remarkable shortening of the computational time without affecting the reliability of the results. The first one, applicable in quantum dynamics, allows to effectively reduce the Hilbert space, still retaining the most important features of the dynamical behaviour of the system. The second approximate procedure, developed in collaboration with prof. Alessandro Troisi from Liverpool University, allows the fast evaluation of the non-local electron-phonon coupling, a quantity describing the strength of thermal motions in organic crystals, with the final goal of developing a method suitable for the analysis of big databases. We have then compared their performances in reproducing experimental results and stressed their strengths and shortcomings together with their range of validity.

We have analyzed the performances of Marcus formula, FGR and SOC in reproducing experimental anisotropic mobilities for tetracene, pentacene, picene and rubrene single crystals. SOC predictions, which are in good agreement with results obtained by quantum dynamic simulations, well reproduce experimental data, with a slight overestimation, though. That is possibly due to the influence of surface contamination, grain boundaries, defects, etc., which have been omitted in simulations but are always present in real samples. Therefore, the SOC approach appears to provide a computationally economical and reliable way for estimating hole transfer mobilities, including their temperature dependence, considering the whole set of intramolecular vibrational coordinates. That approach can also handle cases in which the Fermi Golden Rule is inadequate, i.e. ultrafast hole transfer processes, occurring in molecular systems exhibiting strongly peaked Franck-Condon weighted density of states. Marcus semiclassical approach can provide qualitatively correct values of mobilities at room temperature, but it is unable to predict reliable temperature dependencies because it

cannot account for tunneling effects, which are dominating at low temperatures.

We have then applied a recently developed method, the TLT approach, to the same systems. TLT should be physically more sound for the description of CT in organic semiconductors, since it takes into account quantum localization together with dynamic disorder, i.e. the oscillations of the transfer integrals because of thermal motions. Since evaluating dynamic disorder is computationally expensive, we have developed a methodology for its quick computation relying on two main approximations: the evaluation of the Cartesian gradient of transfer integral and the use of approximate phonons computed within the rigid body approximation. Despite the severe approximations, our method has led to results in excellent agreement with data obtained with more accurate approaches. The relatively high number of molecules studied by this approach has allowed us to outline some general trends. First of all, we have shown that there is almost no correlation between the transfer integral V and their room temperature fluctuation σ. For this reason, the fluctuation of the transfer integral should not be considered an unavoidable property of these materials while, on the contrary, one could search for materials for which the ratio $\sigma/|V|$ is minimized. Secondly, since our data point out that materials with small σ are invariably characterized by small values of the gradient of the transfer integral with respect to all atomic translations $|\nabla V|$, and this quantity is substantially cheaper to evaluate, we highlight the possibility of using $|\nabla V|$ instead of σ to identify materials showing low dynamic disorder.

Using these quantities, we have evaluated mobility in pentacene, rubrene, tetracene and picene single crystal in the framework of TLT approach. We have found a very good agreement between SOC and TLT predictions, and with experimental data, suggesting that both the models are adequate in describing CT in organic semiconductors. However, TLT approach seems to be more appealing than SOC because it does not introduce the arbitrary interpolation assumption of a monoexponential decay (used to get SOC

time averaged rate constants) and it resorts to assumptions in line with the physics underlying CT in organic semiconductors.

Finally, we have presented a strategy for a computationally efficient simulation of charge transfer in DNA. Interest on this topic has arisen because, apart from the biochemical relevance connected with the oxidative damage of nucleic acids, long range hole transfer (HT) makes DNA a potentially well-suited material for nanoelectronics. Indeed DNA has already been used for the design of sensors or as a template, by exploiting its self-assembling properties. In this thesis HT rates through some DNA oligomers has been studied resorting to our quantum dynamics approach, using a set of parameters obtained by reliable density functional calculations carried out in our group, which show a good agreement with results of spectro-electrochemical measurements. Our analysis reproduce in a quantitative way the observed distance dependence of hole transfer rates reported in the literature by Giese's group, shedding light on the role played by delocalized domains in the hole transfer process. Furthermore, analysis over other oligomers, studied by Schuster's group, has allowed us to offer a point of view that can explain the experimental results of both groups, even though they have been considered discordant for a long time, focusing on the impact of different number of guanines in the strands.

It is author's hope that the analysis carried out throughout this thesis may contribute to shed light on the interesting yet controversial topic of computer-aided material science, in a first step towards a future where theory can play a larger role in material design. The spirit that animates the author of this thesis is the hope that one day, quoting ref. 4, "the computational chemist will not only be asked «Why does this material work?», but can also answer «Which derivative do I expect the best outcome, even before synthesis begins?», [...] with a productive collaborative relationships between computational chemists, synthetic chemists, and device engineers."

Part VI

APPENDICES

Appendix A

Marcus formula derivation

One of the simplest derivations of the Marcus equation considers the CT reaction as a radiationless transition between 2 electronic states a and b, resorting to the Landau-Zener formula [96, 109–111] to express the probability for a system to cross from a to b:

$$P_{ab} = \frac{2\pi}{\hbar} \frac{|V_{ab}|^2}{\frac{dx}{dt} \frac{d(V_a - V_b)}{dx}} \tag{A.1}$$

where V_{ab} is the coupling between the two states, $\frac{d(V_a - V_b)}{dx}$ is the difference in slope of the potential energy surfaces and $\frac{dx}{dt}$ is the velocity of the system moving to state b. We rewrite here for convenience eq. 3.1, describing the potential energies of the two states as two parabolas with the same curvature $K = M\omega^2$:

$$V_a = \frac{K(x - x_a)^2}{2} + E_a \qquad\qquad V_b = \frac{K(x - x_b)^2}{2} + E_b. \tag{A.2}$$

The transition rate k_{v_a} for a vibrational state v_a is the product of the frequency the system hits the barrier $(\omega/2\pi)$ and the probability to make the transition P_{ab}. Since the system passes the barrier point twice per vibration cycle (once from the left and once from the right), the rate is

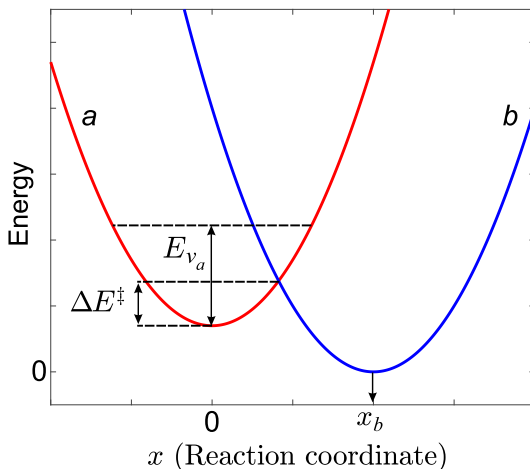$$k_{v_a} = \frac{\omega}{\pi} P_{ab} \tag{A.3}$$

Figure A.1.   Potential energy surfaces for the states a and b.

For a classical harmonic oscillator $(E = M\omega^2 x^2/2 \Rightarrow x\omega = \sqrt{2E/M})$, the velocity $\frac{\mathrm{d}x}{\mathrm{d}t}$ to reach the barrier point is:

$$\frac{\mathrm{d}x}{\mathrm{d}t} = \sqrt{\frac{2}{M}(E_{v_a} - \Delta E^{\ddagger})} \tag{A.4}$$

where we expressed the energy E as the difference between the energy of the state v_a and the activation energy $\Delta E^{\ddagger}$. Finally, from eq. A.2, the difference between the two potential surfaces is

$$V_a - V_b = \frac{M\omega^2 x^2}{2} - \frac{M\omega^2 (x - x_b)^2}{2} \tag{A.5}$$

and taking its derivative we get the difference in slope:

$$\frac{\mathrm{d}(V_a - V_b)}{\mathrm{d}x} = M\omega^2 x_b^2 \tag{A.6}$$

Combining eq.s A.1, A.3, A.4 and A.6, the rate for the state v_a can be written as:

$$k_{v_a} = \frac{2\,|V_{ab}|^2}{\hbar\omega x_b \sqrt{2M(E_{v_a} - \Delta E^{\ddagger})}} \tag{A.7}$$

The mean CT rate k is now obtained averaging over a Boltzmann distribution of vibrational states:

$$k = \frac{\int_0^\infty k_{ab} e^{-\beta E_{v_a}} \mathrm{d}E_{v_a}}{\int_0^\infty e^{-\beta E_{v_a}} \mathrm{d}E_{v_a}} \tag{A.8}$$

that is (making a change of variable in the numerator $z = \sqrt{E_n - \Delta E^\ddagger}$):

$$k = \frac{|V_{ab}|^2}{\hbar\omega x_b \sqrt{2M}} \frac{e^{-\beta \Delta E^\ddagger} \int_0^\infty 2z\,dz\,e^{-\beta z^2}/z}{\int_0^\infty e^{-\beta E_{v_a}} \mathrm{d}E_{v_a}} \tag{A.9}$$

which, after integration, gives the desired result

$$k = \sqrt{2\pi} \frac{|V_{ab}|^2}{\hbar\omega x_b \sqrt{2M k_\mathrm{B} T}} e^{-\Delta E^\ddagger/(k_\mathrm{B} T)} \tag{A.10}$$

Marcus further simplified this formula by assuming that there is neither entropic nor volume change (i.e. $\Delta E^\ddagger = \Delta G^\ddagger$) and relating the activation free energy $\Delta G^\ddagger$ to physically well-sound quantities: the free energy change of the CT reaction (ΔG^0) and the reorganization energy λ, i.e. the energy spent from the state a to reach the nuclear configuration of the state b without actually changing electronic state (fig. A.2).

Rewriting eq. A.2 with the abovementioned assumptions (no entropy changes, $x_a = 0$, $E_b = 0$) we have:

$$G_a = \frac{kx^2}{2} + \Delta G^0 \qquad\qquad G_b = \frac{k(x - x_b)^2}{2} \tag{A.11}$$

Where ΔG^0 is the free energy change of the CT reaction.

It is evident from fig. A.2 that the activation energy $\Delta G^\ddagger$ can be written as:

$$\Delta G^\ddagger = G_b(x_c) + \Delta G^0 \tag{A.12}$$

where x_C is the point where the two potential curves intersect, i.e.
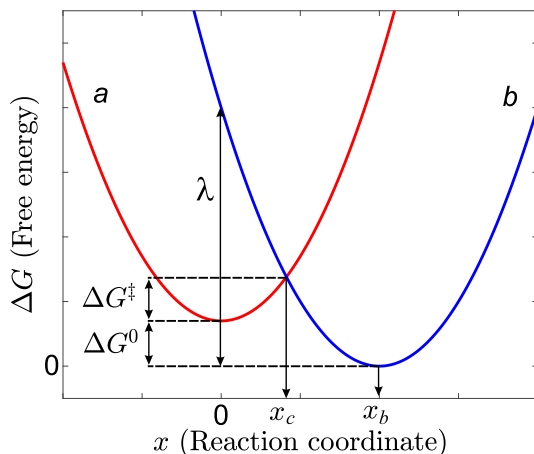
$$G_a(x_C) = G_b(x_C) \tag{A.13}$$

Figure A.2.   Nuclear motion accompanying electron transfer.   Curves *a* and *b* represent the change in free energy with nuclear coordinate *x* for the states between which CT occurs.

Using eq.s A.11 and A.13 and substituting in eq. A.12 we obtain

$$\Delta G^{\ddagger} = \frac{kx_b^2}{8} + \frac{\Delta G^0}{2kx_b^2} + \frac{\Delta G^0}{2} \tag{A.14}$$

Now, defining the reorganization energy λ as the change in Gibbs energy if the reactant state *a* is at the equilibrium conformation of the product state *b* without the electron transfer, it is easy to see that:

$$\lambda = G_b(0) \tag{A.15}$$

Using this definition we can rewrite eq. A.14 as

$$\Delta G^{\ddagger} = \frac{\left(\Delta G^0 + \lambda\right)^2}{4\lambda} \tag{A.16}$$

Substituting this in eq. A.10, and using the definition of the reorganization energy λ (eq. A.15) we finally obtain the kinetic rate expression for CT reaction according to Marcus:

$$k = \frac{|V|^2}{\hbar} \sqrt{\frac{\pi}{\lambda k_{\mathrm{B}}T}} \exp{\frac{\left(\Delta G^0 + \lambda\right)^2}{4\lambda k_{\mathrm{B}}T}} \tag{A.17}$$

Appendix B

FGR derivation and the GF approach

One of the simplest derivation of FGR formula relies on the time-dependent perturbation theory under the assumption that the time of the measurement is larger than the transition time [274], as we shall see in the following.

We start from the time-dependent Schrödinger equation:

$$i\hbar\frac{\partial\big|\Psi(t)\big\rangle}{\partial t} = \mathcal{H}\big|\Psi(t)\big\rangle, \tag{B.1}$$

assuming that the Hamiltonian can be splitted in two contributions:

$$\mathcal{H} = \mathcal{H}^0 + \eta\mathcal{V}(t), \tag{B.2}$$

where $\mathcal{H}^0$ is a time-independent part modeling the isolated system, having eigenvalues and eigenfunctions known, while $\mathcal{V}(t)$ is the perturbing Hamiltonian. η is a dummy variable introduced to take advantage of series expansion.

Denoting by $\{\psi_k^0\}$ the set of eigenfunctions of $\mathcal{H}^0$ with eigenvalues E_k^0

$$\mathcal{H}^0\psi_k^0 = E_k^0\psi_k^0, \tag{B.3}$$

$\{\psi_k^0\}$ are a complete basis set, so $\big|\Psi(x,t)\big\rangle$, eigenfunction of the whole Hamiltonian $(\mathcal{H})$ at time t, can be expressed as linear combination of the eigenfunctions of $\mathcal{H}^0$

$$\big|\Psi(x,t)\big\rangle = \sum_k c_k(t)\big|\psi_k^0(x,t)\big\rangle. \tag{B.4}$$

Since $\big|\psi^0\big\rangle$ is a stationary state, its time dependence is [274]:

$$\big|\psi^0(t)\big\rangle = \big|\psi^0\big\rangle \times \exp\left(-\frac{iE^0 t}{\hbar}\right) \tag{B.5}$$

So we can rewrite eq. B.4 as:

$$\big|\Psi(t)\big\rangle = \sum_k c_k\big|\psi_k^0\big\rangle \times \exp\left(-\frac{iE_k^0 t}{\hbar}\right) \tag{B.6}$$

It is useful to explicitly write out the time dependence of the basis set, so that all the time dependence resides in the combination coefficients c_k. Substituting $\big|\Psi(t)\big\rangle$ in the eq. B.1 we get:

$$
\begin{aligned}
i\hbar\frac{\partial}{\partial t}\left[\sum_k c_k(t)\big|\psi_k^0\big\rangle \times \exp\left(-\frac{iE_k^0 t}{\hbar}\right)\right] = \\
= (\mathcal{H}_0 + \mathcal{V})\left[\sum_l c_l(t)\big|\psi_l^0\big\rangle \times \exp\left(-\frac{iE_l^0 t}{\hbar}\right)\right]
\end{aligned}
\tag{B.7}
$$

From which:

$$i\hbar\left[\sum_k \dot{c}_k(t)\big|\psi_k^0\big\rangle \times \exp\left(-\frac{iE_k^0 t}{\hbar}\right)\right] = \sum_l c_l\mathcal{V}\big|\psi_l^0\big\rangle \times \exp\left(-\frac{iE_l^0 t}{\hbar}\right) \tag{B.8}$$

Multiplying both sides by $\langle\psi_b|$ we get:

$$i\hbar\dot{c}_b(t) = \sum_l c_l\big\langle\psi_b^0\big|\mathcal{V}\big|\psi_l^0\big\rangle \times \exp\left(-i\omega_{lb}t\right) \tag{B.9}$$

Where $\omega_{lb} = \frac{(E_l^0 - E_b^0)}{\hbar}$.

Since (eq. B.2) $\mathcal{V}$ depends on η, so do c_l and c_b, and we can write both c_l and c_b as a (Maclaurin) power series in η,

$$c_b = c_b^{(0)} + \eta c_b^{(1)} + \eta^2 c_b^{(2)} + \ldots . \tag{B.10}$$

Substituting eq. B.10 in eq. B.9 and comparing coefficients of each power of η results in an infinite series of simultaneous equations. The zeroth and first-order equations are respectively

$$i\hbar\dot{c}_b^0(t) = 0 \tag{B.11}$$

$$i\hbar\dot{c}_b^1(t) = \sum_l c_l^0 \langle\psi_b^0|\mathcal{V}|\psi_l^0\rangle \times \exp\left(-i\omega_{lb}t\right). \tag{B.12}$$

Assuming that at time $t = 0$ the system is in one state a, so that $c_a(t = 0) = 1$ while $c_l(t = 0) = 0\ \forall l \neq a$, eq. B.6 becomes:

$$|\psi(0)\rangle = |\psi_a^0(0)\rangle, \tag{B.13}$$

while eq. B.12 is, since $c_n^0 = 1$:

$$i\hbar\dot{c}_b^{(1)}(t) = \langle\psi_b^0|\mathcal{V}|\psi_a^0\rangle \times \exp\left(-i\omega_{ab}t\right). \tag{B.14}$$

Assuming now that $\langle\psi_b^0|\mathcal{V}|\psi_a^0\rangle$, which in the following will be denoted as V_{ba}, is time independent, we get after integration:

$$c_b^{(1)}(t) = \frac{V_{ba}}{\hbar\omega_{ab}} \times [1 - \exp\left(-i\omega_{ab}t\right)] \tag{B.15}$$

This is the amplitude probability to find the system in the state $|b\rangle$ at time t, for a system in the state $|a\rangle$ at time $t = 0$ as a consequence of the action of the perturbation $\mathcal{V}$. Its square modulus is the probability:

$$P = \left(\frac{2|V_{ba}|}{\hbar}\right)^2 \frac{\sin^2\left[\frac{(E_b - E_a)}{2\hbar}t\right]}{|E_b - E_a|^2/\hbar^2} \tag{B.16}$$

Integrating for long times $t \to \infty$, we can take advantage of the limit

$$\lim_{\alpha\to\infty} \frac{1}{\pi} \frac{\sin^2 \alpha x}{\alpha x^2} = \delta(x) \tag{B.17}$$

So we can rewrite eq. B.16 as

$$\lim_{t\to\infty} P = 4 \int \frac{\pi t}{2\hbar} \delta(E_b - E_a)|V_{ba}|^2 \rho(E_b)dE_b \tag{B.18}$$

And since the rate constant is defined as the transition probability per unit time, we have

$$k_{FGR} = \lim_{t \to \infty} \frac{P}{t} = \frac{2\pi}{\hbar} |V_{ba}|^2 \delta(E_{v_b} - E_{v_a}) \tag{B.19}$$

If the transition involves several vibrational states v_a and v_b belonging respectively to state a and b, the transition probability is given by the sum over all vibrational states v_b of b, thermally averaged over all vibrational states v_a of the initial electronic state a. Substituting eq. B.17 in eq. B.16, and taking into account this summation, we get

$$k = \frac{1}{Z} \sum_{v_a, v_b} \exp(-\beta E_{v_a}) \langle a, v_a | V | b, v_b \rangle^2 \delta \left(E_{b,v_b} - E_{a,v_a} - h\nu \right). \tag{B.20}$$

Here Z is the vibrational partition function of the initial electronic state, and the sum runs over all vibrational states of $|a\rangle$ and $|b\rangle$. This infinite summation can be avoided by resorting to the generating function (GF) approach [90, 98], which we will discuss in the next section.

B.1   The generating function approach

As demonstrated in ref.s 90, 91, 98, the absorption cross section for a radiative transition between the electronic states $|a\rangle$ and $|b\rangle$ for unit time occurring at a certain frequency ν is :

$$\sigma(\nu) = \frac{8\pi^3 \nu}{3nc} I_{ba}(\nu)$$
$$I_{ba}(\nu) = \frac{1}{Z} \sum_{v_a, v_b} |\langle b, v_b | \mu | a, v_a \rangle|^2 \, \delta(E_{b,v_b} - E_{a,v_a} - h\nu) \tag{B.21}$$

where c and n are the light velocity in vacuum and the index of refraction, μ denotes the dipole moment operator, v_a and v_b are the vibrational states of $|a\rangle$ and $|b\rangle$, respectively, and Z indicates thermal average over the initial vibrational state. This quantity, which allows to reproduce the experimental absorption/emission spectra, presents the same infinite summation as

in eq. B.20; in other words its solution is of paramount importance also for the evaluation of kinetic constants by FGR.

Following Lax [90] and Kubo [98], the infinite summation in eq. B.21 can be conveniently avoided by introducing the integral representation of Dirac's δ function:

$$\delta(E_{b,v_b} - E_{a,v_a} - h\nu) = h^{-1} \int_{-\infty}^{\infty} \exp\left[-i\left(E_{b,v_b} - E_{a,v_a} - h\nu\right)t/\hbar\right] dt \quad \text{(B.22)}$$

We introduce now the inverse Fourier transform of the function $I_{ba}(t)$:

$$I_{ba}(\nu) = h^{-1} \int dt\, e^{-i\omega t} I_{ba}(t), \quad \text{(B.23)}$$

where

$$I_{ba}(t) = \sum_{v_a} \sum_{v_b} \langle a, v_a | \mu^\dagger e^{-\lambda E_{b,v_b}} | b, v_b \rangle \langle b, v_b | \mu e^{-(\beta-\lambda)E_{a,v_a}} | a, v_a \rangle / Z_a,$$
$$\text{(B.24)}$$

where $\omega = 2\pi\nu$, $\lambda = \mathrm{i}t/\hbar$ and $Z_a = \sum_{v_a} e^{-\beta E_{a,v_a}}$, with $\beta = 1/k_B T$.

Using the completeness relation, we can write the interaction representation of the time independent Hamiltonian as:

$$\sum_{v_a} \exp(-E_{a,v_a}) |a, v_a\rangle\langle a, v_a| = \exp(-\mathcal{H}_a) \quad \text{(B.25)}$$

and integrating over the electronic coordinates $I_{ba}(t)$ can be rewritten in the very simple form:

$$I_{ba}(t) = \frac{1}{Z_a} \sum_{v_a} \langle v_a | \mu_{ab} e^{-\lambda \mathcal{H}_b} \mu_{ba} e^{-(\beta-\lambda)\mathcal{H}_a} | v_a \rangle / Z_a, \quad \text{(B.26)}$$

where μ_{ab} and μ_{ba} are operators in the space of the vibrational coordinates. As outlined in part II, we neglect rotational contributions to the electronic band shape and model the Hamiltonian operators for the nuclear vibrational motion $\mathcal{H}_a$ and $\mathcal{H}_b$ in harmonic approximation. Using mass weighted Cartesian coordinates $\mathbf{Q}$ a generic Hamiltonian operator $\mathcal{H}_z$ can be written as:

$$\mathcal{H}_z = \frac{1}{2}\mathbf{P}^\dagger\mathbf{P} + \frac{1}{2}(\mathbf{Q} - \mathbf{Q^0}_z)^\dagger \mathbf{\Omega}_z^2 (\mathbf{Q} - \mathbf{Q^0}_z), \quad \text{(B.27)}$$

where $\mathbf{Q}_z^0$ is the nuclear equilibrium position vector of the electronic state $|z\rangle$ and $\mathbf{\Omega}_z$ is the vector containing its frequencies. The matrix representation of $\mathcal{H}_z$ can be brought into diagonal form by adopting the set of normal coordinates:

$$\mathbf{Q} - \mathbf{Q_z^0} = \mathbf{L}_z^{-1}\mathbf{q}_z, \tag{B.28}$$

chosen in such a way that:

$$(\mathbf{Q} - \mathbf{Q^0}_z)^\dagger\mathbf{\Omega}_z^2(\mathbf{Q} - \mathbf{Q^0}_z) = \mathbf{q_z}^\dagger\mathbf{L}_z\mathbf{\Omega}_z^2\mathbf{L}_z^{-1}\mathbf{q}_z = \mathbf{q}_z^\dagger\boldsymbol{\omega}_z^2\mathbf{q}_z \tag{B.29}$$

with $\boldsymbol{\omega}_z$ being a diagonal matrix.

From the definition of the normal modes of the electronic states $|a\rangle$ and $|b\rangle$:

$$\mathbf{Q} - \mathbf{Q}_a^0 = \mathbf{L}_a^{-1}\mathbf{q}_a \qquad \mathbf{Q} - \mathbf{Q}_b^0 = \mathbf{L}_b^{-1}\mathbf{q}_b$$

it follows that:

$$\mathbf{Q}_a^0 + \mathbf{L}_a^{-1}\mathbf{q}_a = \mathbf{Q}_b^0 + \mathbf{L}_b^{-1}\mathbf{q}_b$$

getting

$$\mathbf{q}_a = \mathbf{J}\mathbf{q}_b + \mathbf{K}, \qquad \mathbf{J} = \mathbf{L}_a\mathbf{L}_b^{-1}, \qquad \mathbf{K} = \mathbf{L}_a\left(\mathbf{Q}_b^0 - \mathbf{Q}_a^0\right) \tag{B.30}$$

which is the well known Duschinky's affine transformation, allowing to relate the normal coordinates of two different electronic states a and b, where $\mathbf{J}$ is the rotation matrix and $\mathbf{K}$ the displacement vector.

Following derivation in ref.s 96, 119, 120, we will use in the following the Cartesian coordinates, the most convenient representation for small equilibrium displacements.

To numerically evaluate $I_{ba}(\lambda)$ we transform eq. B.26 in the coordinate representation, multiplying it several times by the unit operator in the coordinate representation:

$$\int_\infty^\infty \mathrm{d}\mathbf{Q}|\mathbf{Q}\rangle\langle\mathbf{Q}| = \hat{1} \tag{B.31}$$

148

writing:

$$
\begin{aligned}
I_{ba}(t) =& \frac{1}{Z_a} \int_{-\infty}^{\infty} d\mathbf{Q} \int_{-\infty}^{\infty} d\mathbf{Q}' \int_{-\infty}^{\infty} d\mathbf{Q}'' \int_{-\infty}^{\infty} d\mathbf{Q}''' \int_{-\infty}^{\infty} d\mathbf{Q}^{iv} \\
& \sum_{v_a} \langle v_a | \mathbf{Q} \rangle \langle \mathbf{Q} | \mu_{ab} | \mathbf{Q}' \rangle \langle \mathbf{Q}' | e^{-\lambda \mathcal{H}_b} | \mathbf{Q}'' \rangle \\
& \langle \mathbf{Q}'' | \mu_{ba} | \mathbf{Q}''' \rangle \langle \mathbf{Q}''' | e^{-(\beta-\lambda)\mathcal{H}_a} | \mathbf{Q}^{iv} \rangle \langle \mathbf{Q}^{iv} | v_a \rangle
\end{aligned}
\tag{B.32}
$$

We now interrupt the derivation to focus on some relations and properties that will allow us to significantly simplify eq. B.32.

First of all, we will resort to Condon approximation, assuming that the transition dipole moment does not act over vibrational coordinates, i.e.:

$$
\int d\mathbf{Q}' \langle \mathbf{Q} | \mu_{ab} | \mathbf{Q}' \rangle = \mu_{ab} \delta(\mathbf{Q} - \mathbf{Q}')
\tag{B.33}
$$

Concerning the term $\langle \mathbf{Q} | e^{-\lambda \mathcal{H}_z} | \mathbf{Q}' \rangle$, we first observe that adopting normal coordinates (which uncouple vibrational motion) the Hamiltonian operator can be written as a sum of terms, one for each normal coordinate:

$$
\mathcal{H}_z = \sum_i \hat{h}_{zi}(q_{zi}),
$$

with :

$$
\hat{h}_{zi} \psi_n^{(zi)}(q_{zi}) = \left(n + \frac{1}{2} \right) \hbar \omega_{zi} \psi_n^{(zi)}(q_{zi})
$$

In the normal coordinate representation the total vibrational wavefunction is a product of $3N_A - 6$ harmonic oscillator wavefunctions ($N_A =$ number of atoms):

$$
\Psi_z(\mathbf{q}) = \prod_i \psi_i(q_i)
\tag{B.34}
$$

We can thus write:

$$
\langle \mathbf{q} | e^{-\lambda \mathcal{H}_z} | \mathbf{q}' \rangle = \prod_i \langle q_i | e^{-\lambda \hat{h}_{zi}} | q_i' \rangle
\tag{B.35}
$$

Inserting the unit operator $\sum_{v_i} \langle v_i | v_i \rangle$, where $|v_i\rangle$ is an eigenstate of $\hat{h}_{zi}$, each term of the product in eq. B.35 can be written as:

$$
\begin{aligned}
\langle q_i | e^{-\lambda \hat{h}_{zi}} | q_i' \rangle &= \sum_{v_i} \langle q_i | e^{-\lambda \hat{h}_{zi}} | v_i \rangle \langle v_i | q_i' \rangle = \sum_{v_i} \langle q_i | v_i \rangle e^{-\lambda E_{v_i}} \langle v_i | q_i' \rangle \\
&= \sum_{v_i} e^{-\lambda E_{v_i}} \psi_{v_i}^{(zi)}(q_i) \psi_{v_i}^{(zi)*}(q_i')
\end{aligned}
\tag{B.36}
$$

Resorting to Mehler formula, we can write infinite summation appearing in eq. B.36 into a closer form:

$$
\sum_{v_i} e^{-\lambda E_{v_i}} \Psi_{v_i}(q_i) \Psi_{v_i}^*(q_i') = f_{zi}(q_i, q_i') = \frac{\omega_{zi}}{\sqrt{2\pi \sinh(\lambda \hbar \omega_i)}}
$$

$$
\exp\left[-\frac{\omega_{zi}}{4\hbar} \tanh(\lambda \hbar \omega_{zi}/2)(q_i + q_i')^2 - \frac{\omega_{zi}}{4\hbar} \coth(\lambda \hbar \omega_{zi}/2)(q_i - q_i')^2 \right]
\tag{B.37}
$$

ω_{zi} being the vibrational frequency if the i-th mode of the electronic state $|z\rangle$. Thus:

$$
\langle \mathbf{q} | e^{-\lambda \mathcal{H}_z} | \mathbf{q}' \rangle = f_z(\mathbf{q}, \mathbf{q}') = \prod_i f_{zi}(q_i, q_i')
\tag{B.38}
$$

where for simplicity we have dropped the index z from $\mathbf{q}$. Eq. B.38 can be written in tensor form:

$$
f_z(\mathbf{q}, \mathbf{q}') = \det\left[\frac{\omega_z}{\sqrt{2\pi \sinh(\lambda \hbar \omega_z)}} \right] \times \exp\left[-\frac{1}{4\hbar}(\mathbf{q} + \mathbf{q}')^\dagger \omega_z \right.
$$

$$
\left. \tanh(\lambda \hbar \omega_z/2)(\mathbf{q} + \mathbf{q}') - \frac{1}{4\hbar}(\mathbf{q} - \mathbf{q}')^\dagger \omega_z \coth(\lambda \hbar \omega_z/2)(\mathbf{q} - \mathbf{q}') \right]
\tag{B.39}
$$

where $\boldsymbol{\omega}_z$ is the diagonal matrix of the vibrational frequency of $|z\rangle$. Expressing $f_z(\mathbf{q}, \mathbf{q}')$ as a function of a set of Cartesian displacement coordinates and making explicit the hyperbolic functions and considering that $[\boldsymbol{\omega}, e^{\boldsymbol{\omega}}] = 0$ since each power of an operator commutes with the operator itself, eq. B.39 can be rewritten as:

$$
f_z(q, q') = \det\left[\frac{\omega_z}{\sqrt{2\pi \sinh(\lambda \hbar \boldsymbol{\omega}_z)}} \right] \times \exp\left[-\frac{1}{4\hbar}(\mathbf{q} + \mathbf{q}')^\dagger \right.
$$

$$
(e^{\lambda \hbar \boldsymbol{\omega}_z/2} - e^{-\lambda \hbar \boldsymbol{\omega}_z/2}) \boldsymbol{\omega}_z (e^{\lambda \hbar \boldsymbol{\omega}_z/2} + e^{\frac{-\lambda \hbar \boldsymbol{\omega}_z}{2}})(\mathbf{q} + \mathbf{q}') - \frac{1}{4\hbar}
$$

$$
\left. (\mathbf{q} - \mathbf{q}')^\dagger (e^{\lambda \hbar \boldsymbol{\omega}_z/2} + e^{-\lambda \hbar \boldsymbol{\omega}_z/2}) \boldsymbol{\omega}_z (e^{\lambda \hbar \boldsymbol{\omega}_z/2} - e^{-\lambda \hbar \boldsymbol{\omega}_z/2})(\mathbf{q} - \mathbf{q}') \right]
\tag{B.40}
$$

Since

$$\boldsymbol{\omega}_z = \mathbf{L}_z \boldsymbol{\Omega}_z {\mathbf{L}_z}^{-1},$$

and

$$\mathbf{q} = \mathbf{L}_z(\mathbf{Q} - \mathbf{Q_z^0}),$$

which gives:

$$f_z(\mathbf{Q}, \mathbf{Q}') = \det \left[\frac{\boldsymbol{\Omega}_z}{\sqrt{2\pi \sinh(\lambda\hbar\boldsymbol{\Omega}_z)}} \right] \times$$

$$\times \exp \left[-\frac{1}{4\hbar}(\mathbf{Q} + \mathbf{Q}' - 2\mathbf{Q_z^0})^\dagger \mathbf{L}_z^{-1} (e^{\lambda\hbar\boldsymbol{\omega}_z/2} - e^{-\lambda\hbar\boldsymbol{\omega}_z/2})\mathbf{L}_z\boldsymbol{\Omega_z}\mathbf{L}_z^{-1} \right. \tag{B.41}$$

$$(e^{\lambda\hbar\boldsymbol{\omega}_z/2} + e^{-\lambda\hbar\boldsymbol{\omega}_z/2})\mathbf{L}_z(\mathbf{Q} + \mathbf{Q}' - 2\mathbf{Q_z^0}) - \frac{1}{4\hbar}(\mathbf{Q} - \mathbf{Q}')^\dagger \mathbf{L}_z^{-1}$$

$$\left. (e^{\lambda\hbar\boldsymbol{\omega}_z/2} + e^{-\lambda\hbar\boldsymbol{\omega}_z/2})\mathbf{L}_z\boldsymbol{\Omega_z}\mathbf{L}_z^{-1}(e^{\lambda\hbar\boldsymbol{\omega}_z/2} - e^{-\lambda\hbar\boldsymbol{\omega}_z/2})\mathbf{L}(\mathbf{Q} - \mathbf{Q}') \right]$$

where we have used the identity:

$$\det(\boldsymbol{\omega}_z) = \det(\boldsymbol{\Omega}_z).$$

Considering now that:

$$\mathbf{L}_z^{-1}(e^{\lambda\hbar\boldsymbol{\omega}_z/2} - e^{-\lambda\hbar\boldsymbol{\omega}_z/2})\mathbf{L}_z = e^{\lambda\hbar\boldsymbol{\Omega}_z/2} - e^{-\lambda\hbar\boldsymbol{\Omega}_z/2}$$

eq. B.40 can be rewritten:

$$f_z(\mathbf{Q}, \mathbf{Q}') = \det \left[\frac{\boldsymbol{\Omega}_z}{\sqrt{2\pi \sinh(\lambda\hbar\boldsymbol{\Omega}_z)}} \right] \times$$

$$\times \exp \left[-\frac{1}{4\hbar}(\mathbf{Q} + \mathbf{Q}' - 2\mathbf{Q_z^0})^\dagger \boldsymbol{\Omega_z} \tanh(\lambda\hbar\boldsymbol{\Omega}_z/2)(\mathbf{Q} + \mathbf{Q}' - 2\mathbf{Q_z^0}) \right. \tag{B.42}$$

$$\left. -\frac{1}{4\hbar}(\mathbf{Q} - \mathbf{Q}')^\dagger \boldsymbol{\Omega_z} \coth(\lambda\hbar\boldsymbol{\Omega}_z/2)(\mathbf{Q} - \mathbf{Q}') \right]$$

We now can return to the derivation of GF formula, taking advantage of some of the results shown to simplify eq. B.32.

By substituting eq. B.38 in B.32, we get:

$$I_{ba}(t) = \frac{1}{Z_a} \int_{-\infty}^{\infty} d\mathbf{Q} \int_{-\infty}^{\infty} d\mathbf{Q}'' \int_{-\infty}^{\infty} d\mathbf{Q}^{iv}$$

$$\sum_{v_a} \langle v_a | \mathbf{Q} \rangle |\mu_{ab}|^2 f_b(\mathbf{Q}, \mathbf{Q}'') f_a(\mathbf{Q}'', \mathbf{Q}^{iv}) \langle \mathbf{Q}^{iv} | v_a \rangle$$

$$\frac{1}{Z_a} \int_{-\infty}^{\infty} d\mathbf{Q} \int_{-\infty}^{\infty} d\mathbf{Q}'' \int_{-\infty}^{\infty} d\mathbf{Q}^{iv} \qquad (B.43)$$

$$\sum_{v_a} |\mu_{ab}|^2 f_b(\mathbf{Q}, \mathbf{Q}'') f_a(\mathbf{Q}'', \mathbf{Q}^{iv}) \langle \mathbf{Q}^{iv} | v_a \rangle \langle v_a | \mathbf{Q} \rangle =$$

$$\frac{|\mu_{ab}|^2}{Z_a} \int_{-\infty}^{\infty} d\mathbf{Q} \int_{-\infty}^{\infty} d\mathbf{Q}'' f_b(\mathbf{Q}, \mathbf{Q}'') f_a(\mathbf{Q}'', \mathbf{Q})$$

Using eq. B.42, it becomes:

$$I_{ba}(t) = \frac{|\mu_{ab}|^2}{Z_a} \det\left[\frac{\mathbf{\Omega}_b}{\sqrt{2\pi \sinh((\beta - \lambda)\hbar\mathbf{\Omega}_b)}} \right] \times$$

$$\times \det\left[\frac{\mathbf{\Omega}_a}{\sqrt{2\pi \sinh(\lambda\hbar\mathbf{\Omega}_a)}} \right] \int_{-\infty}^{\infty} d\mathbf{Q} \int_{-\infty}^{\infty} d\mathbf{Q}''$$

$$\exp\left[-\frac{1}{4\hbar}(\mathbf{Q} + \mathbf{Q}'' - 2\mathbf{Q_b^0})^\dagger \mathbf{K_b} \tanh((\beta - \lambda)\hbar\mathbf{\Omega}_b/2)(\mathbf{Q} + \mathbf{Q}'' - 2\mathbf{Q_b^0}) \right.$$

$$-\frac{1}{4\hbar}(\mathbf{Q} - \mathbf{Q}'')^\dagger \mathbf{K_b} \coth((\beta - \lambda)\hbar\mathbf{\Omega}_b/2)(\mathbf{Q} - \mathbf{Q}'')$$

$$-\frac{1}{4\hbar}(\mathbf{Q}'' + \mathbf{Q} - 2\mathbf{Q_a^0})^\dagger \mathbf{K_a} \tanh(\lambda\hbar\mathbf{\Omega}_a/2)(\mathbf{Q}'' + \mathbf{Q} - 2\mathbf{Q_a^0})$$

$$\left. -\frac{1}{4\hbar}(\mathbf{Q}'' - \mathbf{Q})^\dagger \mathbf{K_a} \coth(\lambda\hbar\mathbf{\Omega}_a/2)(\mathbf{Q}'' - \mathbf{Q}) \right]$$

$$(B.44)$$

To solve the integral we make the following change of variables:

$$x = \frac{\mathbf{Q} + \mathbf{Q}''}{2}; y = \frac{\mathbf{Q} - \mathbf{Q}''}{2}; \qquad (B.45)$$

with

$$\begin{pmatrix} Q \\ Q'' \end{pmatrix} = \begin{pmatrix} I & I \\ I & -I \end{pmatrix} \begin{pmatrix} x \\ y \end{pmatrix} \qquad (B.46)$$

and 2^n Jacobian of the transformation $(\mathbf{Q}, \mathbf{Q}")$ to (x, y). The integral obtained is:

$$
I_{ba}(t) = \frac{|\mu_{ab}|^2}{Z_a} \det \left[\frac{\boldsymbol{\Omega}_b}{\sqrt{2\pi \sinh((\beta - \lambda)\hbar\boldsymbol{\Omega}_b)}} \right]
$$

$$
\det \left[\frac{\boldsymbol{\Omega}_a}{\sqrt{2\pi \sinh(\lambda\hbar\boldsymbol{\Omega}_a)}} \right] 2^n \int_{-\infty}^{\infty} dx \int_{-\infty}^{\infty} dy
$$

$$
\exp \left[-\frac{1}{\hbar}(x - \mathbf{Q_b^0})^\dagger \mathbf{K_b} \tanh((\beta - \lambda)\hbar\boldsymbol{\Omega}_b/2)(x - \mathbf{Q_b^0}) \right.
$$

$$
-\frac{1}{\hbar}(y)^\dagger \mathbf{K_b} \coth((\beta - \lambda)\hbar\boldsymbol{\Omega}_b/2)(y)
$$

$$
-\frac{1}{\hbar}(x - \mathbf{Q_a^0})^\dagger \mathbf{K_a} \tanh(\lambda\hbar\boldsymbol{\Omega}_a/2)(x - \mathbf{Q_a^0})
$$

$$
\left. -\frac{1}{\hbar}(-y)^\dagger \mathbf{K_a} \coth(\lambda\hbar\boldsymbol{\Omega}_a/2)(-y) \right]
$$

(B.47)

Using the notation:

$$
\mathbf{T_b} = \frac{1}{\hbar}\mathbf{K_b} \tanh((\beta - \lambda)\hbar\boldsymbol{\Omega}_b/2) \quad \mathbf{C_b} = \frac{1}{\hbar}\mathbf{K_b} \coth((\beta - \lambda)\hbar\boldsymbol{\Omega}_b/2) \quad \text{(B.48)}
$$

$$
\mathbf{T_a} = \frac{1}{\hbar}\mathbf{K_a} \tanh(\lambda\hbar\boldsymbol{\Omega}_a/2) \qquad\qquad \mathbf{C_a} = \frac{1}{\hbar}\mathbf{K_a} \coth(\lambda\hbar\boldsymbol{\Omega}_a/2)
$$

eq. (B.47) becomes:

$$
I_{ba}(t) = \frac{|\mu_{ab}|^2}{Z_a} \det \left[\frac{\boldsymbol{\Omega}_b}{\sqrt{2\pi \sinh((\beta - \lambda)\hbar\boldsymbol{\Omega}_b)}} \right]
$$

$$
\det \left[\frac{\boldsymbol{\Omega}_a}{\sqrt{2\pi \sinh(\lambda\hbar\boldsymbol{\Omega}_a)}} \right] 2^n \int_{-\infty}^{\infty} dx \int_{-\infty}^{\infty} dy \exp \left[-(x - \mathbf{Q_b^0})^\dagger \mathbf{T_b} \right.
$$

$$
\left. (x - \mathbf{Q_b^0}) - (y)^\dagger \mathbf{C_b}(y) - (x - \mathbf{Q_a^0})^\dagger \mathbf{T_a}(x - \mathbf{Q_a^0}) - (-y)^\dagger \mathbf{C_a}(-y) \right]
$$

(B.49)

Solving the two integrals (ref. [96]) we finally obtain:

$$
I_{ba}(t) = \frac{|\mu_{ab}|^2}{Z_a} [\det \Phi]^{-1/2} \exp \left(-\mathbf{KJT_a}(\mathbf{T_a} + \mathbf{T_b})^{-1} \mathbf{T_b JK} \right) \quad \text{(B.50)}
$$

where $[\det\Phi]^{-1/2}$ is:

$$[\det\Phi]^{-1/2} = \det\left[\frac{\mathbf{\Omega}_b}{\sqrt{2\pi\sinh((\beta-\lambda)\hbar\mathbf{\Omega}_b)}}\right]$$
$$\det\left[\frac{\mathbf{\Omega}_a}{\sqrt{2\pi\sinh(\lambda\hbar\mathbf{\Omega}_a)}}\right](\mathbf{C_b}+\mathbf{C_a})(\mathbf{T_b}+\mathbf{T_a})2^n \tag{B.51}$$

Equations B.50 and B.51 depend on the vibrational frequencies of the initial and final state as well as on $\mathbf{J}$ and $\mathbf{K}$ of Duschinky's transformation (B.30). Substituting this result in the inverse Fourier transform, eq. B.23, it is possible to evaluate the Franck-Condon weighted density of states avoiding the infinite summation in eq. B.21.

The generating function approach here described is the most efficient method to evaluate Franck-Condon weighted densities of states, since it allows to include in computations all the normal modes, taking also into account the displacements of the equilibrium positions of the two electronic states, the change of the vibrational frequencies and the effects of normal mode mixing.

Appendix C

Numerical methods for Quantum Dynamics

The most straightforward method for the resolution of the time dependent Schrödinger equation is the diagonalization of the entire Hamiltonian matrix [275], leading to formally exact results. However, this method is computationally extremely expensive (it scales as N^3, where N is the size of the matrix), so it is rarely used in quantum dynamics simulations, where big-sized matrices are usually involved. A popular approximate method capable of handling time evolution for big matrices is the Lanczos method [275–278]. It starts from the time-dependent Schrödinger equation

$$-i\hbar\frac{d\mathbf{C}}{dt} = \mathcal{H}\mathbf{C}, \tag{C.1}$$

whose exact solution would be:

$$\mathbf{C}(t) = \exp\left(-\frac{i}{\hbar}\mathcal{H}t\right)\mathbf{C}(0). \tag{C.2}$$

Expansion of eq. C.2 to the p-th order (with $p < N$) defines p independent vectors in the N-dimensional space:

$$\exp\left(-\frac{i}{\hbar}\mathcal{H}t\right)\mathbf{C}(0) \approx \sum_{k=0}^{p-1}\frac{(-it/\hbar)^k}{k!}\mathcal{H}^k\mathbf{C}(0) = \sum_{k=0}^{p-1}\frac{(-it/\hbar)^k}{k!}\mathbf{d_k}, \tag{C.3}$$

where $\mathbf{d}_k$ are defined as:

$$\mathbf{d}_k = \mathcal{H}\mathbf{d}_{k-1} \qquad\qquad \mathbf{d}_0 = \mathbf{C}_0 \qquad\qquad (C.4)$$

Unfortunately, the p vectors defined in this way are usually not independent. The great advantage of Lanczos procedure is that it yields a set of p independent vectors $\{\mathbf{C}\}_p$, spanning the same subspace of $\{\mathbf{d}\}_p$, in terms of which the Hamiltonian assumes a tridiagonal form.

$$\mathcal{H}\mathbf{C}_0 = \alpha_0\mathbf{C}_0 + \beta_0\mathbf{C}_1$$
$$\mathcal{H}\mathbf{C}_k = \beta_{K-1}\mathbf{C}_k + \alpha_k\mathbf{C}_k + \beta_k\mathbf{C}_{k+1} \qquad (k > 0), \qquad (C.5)$$

where:

$$\alpha_k = \mathbf{C}_k^+\mathcal{H}\mathbf{C}_k$$
$$\beta_{k-1} = \mathbf{C}_{k-1}^+\mathcal{H}\mathbf{C}_k \qquad\qquad (C.6)$$

The vectors and matrix elements in eq.s C.5 and C.6 define a rectangular transformation matrix $\mathbf{A}_{N\times p}$ from the basis $\{\left|l, \bar{v}_l\right\rangle\}_N$ to the p-dimensional subspace spanned by $\{\mathbf{C}\}_p$ and by the Hamiltonian matrix $\mathbf{H}_p$ in this subspace:

$$\mathbf{A}_p = [\mathbf{C}_0\mathbf{C}_1\mathbf{C}_2...\mathbf{C}_{p-1}] \qquad\qquad (C.7)$$

$$\mathbf{H}_p = \begin{pmatrix} \alpha_0 & \beta_0 & 0 & ... & 0 & 0 \\ \beta_0 & \alpha_1 & \beta_1 & ... & 0 & 0 \\ 0 & \beta_1 & \alpha_2 & ... & 0 & 0 \\ ... & ... & ... & ... & ... & ... \\ 0 & 0 & 0 & ... & \alpha_{p-2} & \beta_{p-2} \\ 0 & 0 & 0 & ... & \beta_{p-2} & \alpha_{p-1} \end{pmatrix} \qquad (C.8)$$

We now solve the TDSE in this reduced representation, defining $\mathbf{a}(t)$ (whose dimensions are $p\times 1$) as the vector containing the coefficients of the p vectors $\{\mathbf{C}\}_p$, which are in turn coefficients of the basis $\left|l, \bar{v}_l\right\rangle$.

The Lanczos-reduced TDSE can be now defined as:

$$\frac{\partial\mathbf{a}}{\partial t} = -\frac{i}{\hbar}\mathbf{H}_p\mathbf{a}. \qquad\qquad (C.9)$$

Eq. (C.9) can be solved by diagonalization because of its reduced dimensionality, giving:

$$\mathbf{a}(t) = \exp\left\{-\frac{\mathrm{i}}{\hbar}\mathbf{H}_p t\right\}\mathbf{a}(0). \tag{C.10}$$

Where the coefficients $\mathbf{C}$ are obtained from the matrix $\mathbf{A}_p$,

$$\mathbf{C}(t) = \mathbf{A}_p \mathbf{a}(t). \tag{C.11}$$

Finally the wavefunction can be evaluated as:

$$\Psi(t) = \sum_{l,\bar{v}_l} \mathbf{C}_{\bar{v}_l}^{(l)}(t)\big|l,\bar{v}_l\big\rangle. \tag{C.12}$$

From this derivation it is apparent that Lanczos method leads to wrong results when amplitude in the last reduced basis vector $\mathbf{C}_{p-1}$ cannot escape to the (unknown) vector $\mathbf{C}_p$ outside the reduced basis. Therefore the simplest criterion for the time τ, over which eq. C.10 is valid, is to set a limit on the probability that the system is in the last reduced vector $\mathbf{C}_{p-1}$, i.e.

$$\big|[\mathbf{a}(t)]_p\big|^2 \leq \epsilon. \tag{C.13}$$

It can be shown that [136, 275], given an accuracy parameter ϵ, the Lanczos method yields errors lower than ϵ in a time interval $0 \leq t \leq \tau$, where

$$\tau = \left[\epsilon\left(\frac{(p-1)!}{\prod_{k=0}^{p-1}\beta_k}\right)^2\right]^{1/[2(p-1)]}. \tag{C.14}$$

In practical implementation it has been noticed that convergence is achieved for $p = 20 - 30$ for the time intervals analyzed in this thesis [275].

Bibliography

[1] Wang, C.; Dong, H.; Jiang, L.; Hu, W. *Chem. Soc. Rev.* **2018**, *47*, 422–500.

[2] Coropceanu, V.; Cornil, J.; da Silva Filho, D. A.; Olivier, Y.; Silbey, R.; Brédas, J.-L. *Chem. Rev.* **2007**, *107*, 926–952.

[3] Köhler, A.; Bässler, H. *Electronic Processes in Organic Semiconductors*; Wiley-VCH Verlag: Germany, 2015.

[4] Mei, J.; Diao, Y.; Appleton, A. L.; Fang, L.; Bao, Z. *J. Am. Chem. Soc.* **2013**, *135*, 6724–6746.

[5] Facchetti, A. *Mater. Today* **2007**, *10*, 28 – 37.

[6] Brütting, W.; Frischeisen, J.; Schmidt, T. D.; Scholz, B. J.; Mayr, C. *Phys. Stat. Sol. (a)* **2013**, *210*, 44–65.

[7] Kippelen, B.; Brédas, J. L. *Energy Environ. Sci.* **2009**, *2*, 251–261.

[8] Das, R.; Ghaffarzadeh, K.; He, X. *Printed, Organic & Flexible Electronics Forecasts, Players & Opportunities 2017-2027*; IdTechEx, 2017.

[9] Pochettino, A. *Rend. Mat. Acc. Lincei* **1906**, *5*, 355–363.

[10] Stark, J.; Steubing, W. *Phys. Z.* **1908**, *9*, 481.

[11] E., P. W. *Annal. Phys.* **1913**, *345*, 677–700.

[12] Pochettino, A. *J. Chim. Phys.* **1953**, *50*, 64.

[13] Pope, M.; Kallmann, H. P.; Magnante, P. *J. Chem. Phys.* **1963**, *38*, 2042–2043.

[14] Helfrich, W.; Schneider, W. G. *Phys. Rev. Lett.* **1965**, *14*, 229–231.

[15] Tang, C. W.; VanSlyke, S. A. *Appl. Phys. Lett.* **1987**, *51*, 913–915.

[16] Burroughes, J. H.; Bradley, D. D. C.; Brown, A. R.; Marks, R. N.; Mackay, K.; Friend, R. H.; Burns, P. L.; Holmes, A. B. *Nature* **1990**, *347*, 539–541.

[17] Hasegawa, T.; Takeya, J. *Sci. Tech. Adv. Mat.* **2009**, *10*, 024314.

[18] Jurchescu, O. D.; Baas, J.; Palstra, T. T. M. *Appl. Phys. Lett.* **2004**, *84*, 3061–3063.

[19] Yavuz, I.; Martin, B. N.; Park, J.; Houk, K. N. *J. Am. Chem. Soc.* **2015**, *137*, 2856–2866.

[20] Dong, H.; Wang, C.; Hu, W. *Chem. Commun.* **2010**, *46*, 5211–5222.

[21] D'Avino, G.; Muccioli, L.; Zannoni, C.; Beljonne, D.; Soos, Z. G. *J. Chem. Theory Comput.* **2014**, *10*, 4959–4971.

[22] Atahan-Evrenk, S.; Aspuru-Guzik, A. *Top. Curr. Chem.* **2014**, *345*, 95–138.

[23] Podzorov, V.; Menard, E.; Borissov, A.; Kiryukhin, V.; Rogers, J. A.; Gershenson, M. E. *Phys. Rev. Lett.* **2004**, *93*, 086602.

[24] Reese, C.; Chung, W.-J.; Ling, M.-m.; Roberts, M.; Bao, Z. *Appl. Phys. Lett.* **2006**, *89*, 202108.

[25] da Silva Filho, D. A.; Kim, E. G.; Brédas, J. L. *Adv. Mater.* **2005**, *17*, 1072–1076.

[26] Lilienfeld, E. J. Method and apparatus for controlling electric currents. 1930; US Patent 1745175.

[27] Moore, G. E. *Electronics Magazine* **1965**, *38*, 114–116.

[28] Horowitz, G. *Adv. Mater.* **1998**, *10*, 365–377.

[29] Pesavento, P. V.; Chesterfield, R. J.; Newman, C. R.; Frisbie, C. D. *J. Appl. Phys.* **2004**, *96*, 7312–7324.

[30] Podzorov, V.; Sysoev, S. E.; Loginova, E.; Pudalov, V. M.; Gershenson, M. E. *Appl. Phys. Lett.* **2003**, *83*, 3504–3506.

[31] Veres, J.; Ogier, S.; Leeming, S.; Cupertino, D.; Mohialdin Khaffaf, S. *Adv. Funct. Mater.* **2003**, *13*, 199–204.

[32] Stassen, A. F.; de Boer, R. W. I.; Iosad, N. N.; Morpurgo, A. F. *Appl. Phys. Lett.* **2004**, *85*, 3899–3901.

[33] Haber, K. S.; Albrecht, A. C. *J. Phys. Chem.* **1984**, *88*, 6025–6030.

[34] Kepler, R. G. *Phys. Rev.* **1960**, *119*, 1226–1229.

[35] LeBlanc, O. H. *J. Chem. Phys.* **1960**, *33*, 626–626.

[36] Afzali, A.; Dimitrakopoulos, C. D.; Breen, T. L. *J. Am. Chem. Soc.* **2002**, *124*, 8812–8813.

[37] Gundlach, D. J.; Jackson, T. N.; Schlom, D. G.; Nelson, S. F. *Appl. Phys. Lett.* **1999**, *74*, 3302–3304.

[38] Lin, Y.-Y.; Gundlach, D. I.; Nelson, S. F.; Jackson, T. N. *IEEE Trans. Electron Devices* **1997**, *44*, 1325–1331.

[39] Yang, H.; Shin, T. J.; Ling, M.-M.; Cho, K.; Ryu, C. Y.; Bao, Z. *J. Am. Chem. Soc.* **2005**, *127*, 11542–11543.

[40] Kelley, T. W.; Muyres, D. V.; Baude, P. F.; Smith, T. P.; Jones, T. D. *Mater. Res. Soc. Symp. Proc.* **2003**, *771*, L6.5.1–L6.5.10.

[41] Warman, J. M.; de Haas, M. P.; Dicker, G.; Grozema, F. C.; Piris, J.; Debije, M. G. *Chem. Mater.* **2004**, *16*, 4600–4609.

[42] Prins, P.; Grozema, F. C.; Schins, J. M.; Savenije, T. J.; Patil, S.; Scherf, U.; Siebbeles, L. D. A. *Phys. Rev. B* **2006**, *73*, 045204.

[43] Pope, M.; Swenberg, C. E. *Electronic Processes in Organic Crystals and Polymers*; Oxford University Press: New York, 1999.

[44] Kepler, R. G. Electron and hole mobility in anthracene. Annual Report 1963 Conference on Electrical Insulation. 1963; p 64.

[45] Karl, N.; Marktanner, J. *Mol. Cryst. Liq. Cryst.* **2001**, *355*, 149–173.

[46] Xia, Y.; Kalihari, V.; Frisbie, C. D.; Oh, N. K.; Rogers, J. A. *Appl. Phys. Lett.* **2007**, *90*, 162106.

[47] Mattheus, C. C.; de Wijs, G. A.; de Groot, R. A.; Palstra, T. T. M. *J. Am. Chem. Soc.* **2003**, *125*, 6323–6330.

[48] Takeyama, Y.; Ono, S.; Matsumoto, Y. *Appl. Phys. Lett.* **2012**, *101*, 083303.

[49] Lee, J. Y.; Roth, S.; Park, Y. W. *Appl. Phys. Lett.* **2006**, *88*, 252106.

[50] Roberson, L. B.; Kowalik, J.; Tolbert, L. M.; Kloc, C.; Zeis, R.; Chi, X.; Fleming, R.; Wilkins, C. *J. Am. Chem. Soc.* **2005**, *127*, 3069–3075.

[51] Niimi, K.; Shinamura, S.; Osaka, I.; Miyazaki, E.; Takimiya, K. *J. Am. Chem. Soc.* **2011**, *133*, 8732–8739.

[52] Tönshoff, C.; Bettinger, H. *Angew. Chem. Int. Ed.* **2010**, *49*, 4125–4128.

[53] Illig, S.; Eggeman, A. S.; Troisi, A.; Jiang, L.; Warwick, C.; Nikolka, M.; Schweicher, G.; Yeates, S. G.; Geerts, Y. H.; Anthony, J. E.; Sirringhaus, H. *Nat. Commun.* **2016**, *7*, 10736.

[54] Fratini, S.; Ciuchi, S.; Mayou, D.; De Laissardière, G. T.; Troisi, A. *Nat. Mater.* **2017**, *16*, 998–1002.

[55] Xie, X.; Santana-Bonilla, A.; Troisi, A. *J. Chem. Theory Comput.* **2018**, *14*, 3752–3762.

[56] Landi, A.; Borrelli, R.; Capobianco, A.; Velardo, A.; Peluso, A. *J. Chem. Theory Comput.* **2018**, *14*, 1594–1601.

[57] Okamoto, T.; Kudoh, K.; Wakamiya, A.; Yamaguchi, S. *Chem. Eur. J.* **2007**, *13*, 548–556.

[58] Takimiya, K.; Osaka, I.; Mori, T.; Nakano, M. *Acc. Chem. Res.* **2014**, *47*, 1493–1502.

[59] Yamamoto, T.; Takimiya, K. *J. Am. Chem. Soc.* **2007**, *129*, 2224–2225.

[60] Haas, S.; Takahashi, Y.; Takimiya, K.; Hasegawa, T. *Appl. Phys. Lett.* **2009**, *95*, 022111.

[61] Sokolov, A.; Atahan, S.; Mondal, R.; Akkerman, H.; Sánchez-Carrera, R.; Granados, S.; Schrier, J.; Mannsfeld, S.; Zoombelt, A.; Zhenan, B.; Aspuru-Guzik, A. *Nat. Commun.* **2011**, *2*, 437.

[62] Gao, J.; Li, R.; Li, L.; Meng, Q.; Jiang, H.; Li, H.; Hu, W. *Adv. Mater.* **2007**, *19*, 3008–3011.

[63] Li, R.; Jiang, L.; Meng, Q.; Gao, J.; Li, H.; Tang, Q.; He, M.; Hu, W.; Liu, Y.; Zhu, D. *Adv. Mater.* **2009**, *21*, 4492–4495.

[64] Wade, J.; Steiner, F.; Niedzialek, D.; James, D. T.; Jung, Y.; Yun, D.-J.; Bradley, D. D. C.; Nelson, J.; Kim, J.-S. *J. Mater. Chem. C* **2014**, *2*, 10110–10115.

[65] Ebata, H.; Izawa, T.; Miyazaki, E.; Takimiya, K.; Ikeda, M.; Kuwabara, H.; Yui, T. *J. Am. Chem. Soc.* **2007**, *129*, 15732–15733.

[66] Liu, C.; Minari, T.; Lu, X.; Kumatani, A.; Takimiya, K.; Tsukagoshi, K. *Adv. Mater.* **2011**, *23*, 523–526.

[67] Sakamoto, Y.; Suzuki, T.; Kobayashi, M.; Gao, Y.; Fukai, Y.; Inoue, Y.; Sato, F.; Tokito, S. *J. Am. Chem. Soc.* **2004**, *126*, 8138–8140.

[68] Moon, H.; Zeis, R.; Borkent, E.-J.; Besnard, C.; Lovinger, A. J.; Siegrist, T.; Kloc, C.; Bao, Z. *J. Am. Chem. Soc.* **2004**, *126*, 15322–15323.

[69] Tang, M. L.; Oh, J. H.; Reichardt, A. D.; Bao, Z. *J. Am. Chem. Soc.* **2009**, *131*, 3733–3740.

[70] An, Z.; Yu, J.; Jones, S.; Barlow, S.; Yoo, S.; Domercq, B.; Prins, P.; Siebbeles, L.; Kippelen, B.; Marder, S. *Adv. Mater.* **2005**, *17*, 2580–2583.

[71] Bashir, A.; Heck, A.; Narita, A.; Feng, X.; Nefedov, A.; Rohwerder, M.; Mullen, K.; Elstner, M.; Woll, C. *Phys. Chem. Chem. Phys.* **2015**, *17*, 21988–21996.

[72] Singh, T. B.; Sariciftci, N. S.; Yang, H.; Yang, L.; Plochberger, B.; Sitter, H. *Appl. Phys. Lett.* **2007**, *90*, 213512.

[73] Mendil, N.; Daoudi, M.; Berkai, Z.; Belghachi, A. *J. Phys.: Conf. Series* **2015**, *647*, 012057.

[74] Dürkop, T.; Kim, B. M.; Fuhrer, M. S. *J. Phys.: Condens. Matter* **2004**, *16*, R553.

[75] Mondal, S.; Lin, W.-H.; Chen, Y.-C.; Huang, S.-H.; Yang, R.; Chen, B.-H.; Yang, T.-F.; Mao, S.-W.; Kuo, M.-Y. *Org. Electr.* **2015**, *23*, 64 – 69.

[76] Cornil, J.; Beljonne, D.; Calbert, J.-P.; Brédas, J.-L. *Adv. Mater.* **2001**, *13*, 1053–1067.

[77] Brédas, J. L.; Calbert, J. P.; da Silva Filho, D. A.; Cornil, J. *Proc. Natl. Acad. Sci.* **2002**, *99*, 5804–5809.

[78] Chua, L.-L.; Zaumseil, J.; Chang, J.-F.; Ou, E. C.-W.; Ho, P. K.-H.; Sirringhaus, H.; Friend, R. H. *Nature* **2005**, *434*, 194–199.

[79] Akimov, A. V.; Prezhdo, O. V. *Chem. Rev.* **2015**, *115*, 5797–5890.

[80] Price, S. L. *Chem. Soc. Rev.* **2014**, *43*, 2098–2111.

[81] Wang, L.; Nan, G.; Yang, X.; Peng, Q.; Li, Q.; Shuai, Z. *Chem. Soc. Rev.* **2010**, *39*, 423–434.

[82] Needs, R. J.; Pickard, C. J. *APL Mater.* **2016**, *4*, 053210.

[83] Feng, X.; Marcon, V.; Pisula, W.; Hansen, M. R.; Kirkpatrick, J.; Grozema, F.; Andrienko, D.; Kremer, K.; Müllen, K. *Nat. Mater.* **2009**, *8*, 421–426.

[84] Blouin, N.; Michaud, A.; Gendron, D.; Wakim, S.; Blair, E.; Neagu-Plesu, R.; Belletête, M.; Durocher, G.; Tao, Y.; Leclerc, M. *J. Am. Chem. Soc.* **2008**, *130*, 732–742.

[85] Li, J.; Zhao, Y.; Tan, H. S.; Guo, Y.; Di, C.-A.; Yu, G.; Liu, Y.; Lin, M.; Lim, S. H.; Zhou, Y.; Su, H.; Ong, B. S. *Sci. Rep.* **2012**, *2*, 754.

[86] Sánchez-Carrera, R. S.; Atahan, S.; Schrier, J.; Aspuru-Guzik, A. *J. Phys. Chem. C* **2010**, *114*, 2334–2340.

[87] Landi, A.; Troisi, A. *J. Phys. Chem. C* **2018**, *122*, 18336–18345.

[88] Groom, C. R.; Bruno, I. J.; Lightfoot, M. P.; Ward, S. C. *Acta Cryst. B* **2016**, *72*, 171–179.

[89] Libby, W. F. *J. Phys. Chem.* **1952**, *56*, 863–868.

[90] Lax, M. *J. Chem. Phys.* **1952**, *20*, 1752–1760.

[91] Kubo, R. *Phys. Rev.* **1952**, *86*, 929–937.

[92] Marcus, R. A. *J. Chem. Phys.* **1956**, *24*, 966–978.

[93] Marcus, R. A. *J. Chem. Phys.* **1956**, *24*, 979–989.

[94] Marcus, R. A. *J. Chem. Phys.* **1957**, *26*, 867–871.

[95] Marcus, R. A. *J. Chem. Phys.* **1984**, *81*, 4494–4500.

[96] Borrelli, R.; Peluso, A. *WIREs: Comput. Mol. Sci.* **2013**, *3*, 542–559.

[97] Dirac, P. A. M. *Proc. R. Soc. A* **1927**, *114*, 243–265.

[98] Kubo, R.; Toyozawa, Y. *Prog. Theor. Phys.* **1955**, *13*, 160–182.

[99] Borrelli, R.; Peluso, A. *J. Chem. Theory Comput.* **2015**, *11*, 415–422.

[100] Landi, A.; Borrelli, R.; Capobianco, A.; Velardo, A.; Peluso, A. *J. Phys. Chem. C* **2018**, Just Accepted.

[101] Kubo, R. *J. Math. Phys.* **1963**, *4*, 174–183.

[102] Mukamel, S. *Principles of Nonlinear Optical Spectroscopy*; Oxford University Press: USA, 1995; Chapter 3.

[103] Breuer, H. P.; Petruccione, F. *The Theory of Open Quantum Systems*; Oxford University Press: USA, 2002; Chapter 3.

[104] Van Kampen, N. G. *Physica* **1974**, *74*, 215–238.

[105] Izmaylov, A. F.; Mendive-Tapia, D.; Bearpark, M. J.; Robb, M. A.; Tully, J. C.; Frisch, M. J. *J. Chem. Phys.* **2011**, *135*, 234106.

[106] Pereverzev, A.; Bittner, E. R. *J. Chem. Phys.* **2006**, *125*, 104906.

[107] Fratini, S.; Mayou, D.; Ciuchi, S. *Adv. Funct. Mater.* **2016**, *26*, 2292–2315.

[108] Ciuchi, S.; Fratini, S. *Phys. Rev. B* **2012**, *86*, 245201.

[109] Levich, V. G. *Adv. Electrochem. Electrochem. Eng.* **1966**, *4*, 249–371.

[110] Landau, L. *Physik Z Sowjetunion* **1932**, *2*, 46–51.

[111] Zener, C. *Proc. R. Soc. London A* **1932**, *137*, 696–702.

[112] Troisi, A.; Orlandi, G. *Chem. Phys. Lett.* **2001**, *344*, 509 – 518.

[113] Norton, J. E.; Brédas, J.-L. *J. Am. Chem. Soc.* **2008**, *130*, 12377–12384.

[114] McMahon, D. P.; Troisi, A. *J. Phys. Chem. Lett.* **2010**, *1*, 941–946.

[115] He, Y.; Bussolotti, F.; Xin, Q.; Yang, J.; Kera, S.; Ueno, N.; Duhm, S. *J. Phys. Chem. C* **2016**, *120*, 14568–14574.

[116] Fermi, E. *Nuclear Physics*; Chicago Press: Chicago, 1950.

[117] Duschinsky, F. *Acta Physicochim. USSR* **1937**, *7*, 551–566.

[118] Nan, G.; Yang, X.; Wang, L.; Shuai, Z.; Zhao, Y. *Phys. Rev. B* **2009**, *79*, 115203.

[119] Borrelli, R.; Peluso, A. *Phys. Chem. Chem. Phys.* **2011**, *13*, 4420–4426.

[120] Borrelli, R.; Capobianco, A.; Peluso, A. *J. Phys. Chem. A* **2012**, *116*, 9934–9940.

[121] Borrelli, R.; Capobianco, A.; Peluso, A. *Can. J. Chem.* **2013**, *91*, 495–504.

[122] Kubo, R. *J. Phys. Soc. Jpn.* **1962**, *17*, 1100–1120.

[123] Nitzan, A.; Jortner, J. *J. Chem. Phys.* **1973**, *58*, 2412–2434.

[124] Jang, S.; Jun, Y.; Silbey, R. *J. Chem. Phys.* **2002**, *275*, 319 – 332, Photoprocesses in Multichromophoric Molecular Assemblies.

[125] Domcke, W.; Stock, G. *Adv. Chem. Phys.* **1997**, *100*, 1–169.

[126] Domcke, W.; Yarkony, D. R. *Annu. Rev. Phys. Chem.* **2012**, *63*, 325–352.

[127] Fox, R. F. *J. Math. Phys.* **1975**, *16*, 289–297.

[128] Magnus, W. *Comm. Pure Appl. Math.* **1954**, *7*, 649–673.

[129] Deng, W.-Q.; Goddard, W. A. *J. Phys. Chem. B* **2004**, *108*, 8614–8621.

[130] Zhang, Y.; Cai, X.; Bian, Y.; Li, X.; Jiang, J. *J. Phys. Chem. C* **2008**, *112*, 5148–5159.

[131] Wen, S.-H.; Li, A.; Song, J.; Deng, W.-Q.; Han, K.-L.; Goddard, W. A. *J. Phys. Chem. B* **2009**, *113*, 8813–8819.

[132] Deng, W.; Sun, L.; Huang, J.; Chai, S.; Wen, S.; Han, K. *Nature Protocols* **2015**, *10*, 632–642.

[133] Blülle, B.; Troisi, A.; Häusermann, R.; Batlogg, B. *Phys. Rev. B* **2016**, *93*, 035205.

[134] Bixon, M.; Giese, B.; Wessely, S.; Langenbacher, T.; Michel-Beyerle, M. E.; Jortner, J. *Proc. Natl. Acad. Sci. USA* **1999**, *96*, 11713–11716.

[135] Landi, A. Studio teorico della migrazione di carica in oligomeri del DNA. M.Sc. thesis, Universitá degli studi di Salerno, 2015.

[136] Lubich, C. *From Quantum to Classical Molecular Dynamics: Reduced Models and Numerical Analysis*; European Mathematical Society Publishing House: Zuerich, Switzerland, 2008; Chapter 10.

[137] Jankowiak, H.-C.; Stuber, J. L.; Berger, R. *J. Chem. Phys.* **2007**, *127*, 234101.

[138] Santoro, F.; Lami, A.; Improta, R.; Bloino, J.; Barone, V. *J. Chem. Phys.* **2008**, *128*, 224311.

[139] Borrelli, R.; Capobianco, A.; Landi, A.; Peluso, A. *Phys. Chem. Chem. Phys.* **2015**, *17*, 30937–30945.

[140] Sharp, T. E.; Rosenstock, H. M. *J. Chem. Phys.* **1964**, *41*, 3453–3463.

[141] Warshel, A.; Karplus, M. *Chem. Phys. Lett.* **1972**, *17*, 7 – 14.

[142] Peluso, A.; Santoro, F.; Del Re, G. *Int. J. Quantum Chem.* **1997**, *63*, 233–244.

[143] Reimers, J. R. *J. Chem. Phys.* **2001**, *115*, 9103–9109.

[144] Borrelli, R.; Peluso, A. *J. Chem. Phys.* **2003**, *119*, 8437–8448.

[145] Borrelli, R.; Peluso, A. *J. Chem. Phys.* **2006**, *125*, 194308–8.

[146] Borrelli, R.; Peluso, A. *J. Chem. Phys.* **2008**, *128*, 044303–7.

[147] Heck, A.; Kranz, J. J.; Kubar, T.; Elstner, M. *J. Chem. Theory Comput.* **2015**, *11*, 5068–5082.

[148] Heck, A.; Kranz, J. J.; Elstner, M. *J. Chem. Theory Comput.* **2016**, *12*, 3087–3096.

[149] Troisi, A.; Orlandi, G. *Phys. Rev. Lett.* **2006**, *96*, 086601.

[150] Ortmann, F.; Bechstedt, F.; Hannewald, K. *Phys. Stat. Sol. (b)* **2011**, *248*, 511–525.

[151] Troisi, A. *J. Chem. Phys.* **2011**, *134*, 034702.

[152] Wang, L.; Beljonne, D. *J. Phys. Chem. Lett.* **2013**, *4*, 1888–1894.

[153] Lee, C. K.; Moix, J.; Cao, J. *J. Chem. Phys.* **2015**, *142*, 164103.

[154] De Filippis, G.; Cataudella, V.; Mishchenko, A. S.; Nagaosa, N.; Fierro, A.; de Candia, A. *Phys. Rev. Lett.* **2015**, *114*, 086601.

[155] Chen, D.; Ye, J.; Zhang, H.; Zhao, Y. *J. Phys. Chem. B* **2011**, *115*, 5312–5321.

[156] Spencer, J.; Gajdos, F.; Blumberger, J. *J. Chem. Phys.* **2016**, *145*, 064102.

[157] Ciuchi, S.; Fratini, S.; Mayou, D. *Phys. Rev. B* **2011**, *83*, 081202.

[158] Su, W. P.; Schrieffer, J. R.; Heeger, A. J. *Phys. Rev. Lett.* **1979**, *42*, 1698–1701.

[159] Yi, Y.; Coropceanu, V.; Brédas, J.-L. *J. Chem. Phys.* **2012**, *137*, 164303.

[160] Coropceanu, V.; Sánchez-Carrera, R. S.; Paramonov, P.; Day, G. M.; Brédas, J.-L. *J. Phys. Chem. C* **2009**, *113*, 4679–4686.

[161] Sánchez-Carrera, R. S.; Paramonov, P.; Day, G. M.; Coropceanu, V.; Brédas, J.-L. *J. Am. Chem. Soc.* **2010**, *132*, 14437–14446.

[162] Ordejón, P.; Boskovic, D.; Panhans, M.; Ortmann, F. *Phys. Rev. B* **2017**, *96*, 035202.

[163] Nyman, J.; Pundyke, O. S.; Day, G. M. *Phys. Chem. Chem. Phys.* **2016**, *18*, 15828–15837.

[164] Howard, J. A. K.; Allen, F. H.; Shields, G. P. *Implications of Molecular and Materials Structure for New Technologies*; Springer Science & Business Media, 2012.

[165] Kim, J.; Kwon, O.-P.; Brunner, F. D. J.; Jazbinsek, M.; Lee, S.-H.; Günter, P. *J. Phys. Chem. C* **2015**, *119*, 10031–10039.

[166] Venuti, E.; Della Valle, R. G.; Farina, L.; Brillante, A.; Masino, M.; Girlando, A. *Phys. Rev. B* **2004**, *70*, 104106.

[167] Abdulla, M.; Refson, K.; Friend, R. H.; Haynes, P. D. *J. Phys. Condens. Matter* **2015**, *27*, 375402.

[168] Venuti, E.; Bilotti, I.; Della Valle, R. G.; Brillante, A.; Ranzieri, P.; Masino, M.; Girlando, A. *J. Phys. Chem. C* **2008**, *112*, 17416–17422.

[169] Schettino, V. *J. Mol. Spectrosc.* **1970**, *34*, 78 – 96.

[170] Girlando, A.; Grisanti, L.; Masino, M.; Bilotti, I.; Brillante, A.; Della Valle, R. G.; Venuti, E. *Phys. Rev. B* **2010**, *82*, 035208.

[171] Li, Y.; Coropceanu, V.; Brédas, J.-L. *J. Chem. Phys.* **2013**, *138*, 204713.

[172] Hannewald, K.; Stojanović, V. M.; Schellekens, J. M. T.; Bobbert, P. A.; Kresse, G.; Hafner, J. *Phys. Rev. B* **2004**, *69*, 075211.

[173] Nguyen, T. P.; Shim, J. H.; Lee, J. Y. *J. Phys. Chem. C* **2015**, *119*, 11301–11310.

[174] Schober, C.; Reuter, K.; Oberhofer, H. *J. Phys. Chem. Lett* **2016**, *7*, 3973–3977.

[175] Troisi, A. *Org. Electr.* **2011**, *12*, 1988 – 1991.

[176] Stehr, V.; Fink, F., R.; Tafipolski, M.; Deibel, C.; Engels, B. *WIREs Comput. Mol. Sci.* **2016**, *6*, 694–720.

[177] Troisi, A. *Adv. Mater.* **2007**, *19*, 2000–2004.

[178] Ren, J.; Vukmirović, N.; Wang, L.-W. *Phys. Rev. B* **2013**, *87*, 205117.

[179] Friedman, L. *Phys. Rev.* **1964**, *133*, A1668–A1679.

[180] Cheng, Y. C.; Silbey, R. J.; da Silva Filho, D. A.; Calbert, J. P.; Cornil, J.; Brédas, J. L. *J. Chem. Phys.* **2003**, *118*, 3764–3774.

[181] Vehoff, T.; Baumeier, B.; Troisi, A.; Andrienko, D. *J. Am. Chem. Soc.* **2010**, *132*, 11702–11708.

[182] Shuai, Z.; Wang, L.; Song, C. *Theory of Charge Transport in Carbon Electronic Materials*; Springer Briefs in Molecular Science; Springer Press, 2012.

[183] Sundar, V. C.; Zaumseil, J.; Podzorov, V.; Menard, E.; Willett, R. L.; Someya, T.; Gershenson, M. E.; Rogers, J. A. *Science* **2004**, *303*, 1644–1646.

[184] Bakulin, A. A.; Lovrincic, R.; Yu, X.; Selig, O.; Bakker, H. J.; Rezus, Y. L. A.; Nayak, P. K.; Fonari, A.; Coropceanu, V.; Brédas, J.-L.; Cahen, D. *Nat. Commun.* **2015**, *6*, 7880.

[185] Schmidt, W. *J. Chem. Phys.* **1977**, *66*, 828–845.

[186] Malagoli, M.; Coropceanu, V.; da Silva Filho, D. A.; Brédas, J. L. *J. Chem. Phys.* **2004**, *120*, 7490–7496.

[187] Capobianco, A.; Borrelli, R.; Noce, C.; Peluso, A. *Theor. Chem. Acc.* **2012**, *131*, 1181.

[188] Peluso, A.; Borrelli, R.; Capobianco, A. *J. Phys. Chem. A* **2009**, *113*, 14831–14837.

[189] Ling, M.; Reese, C.; Briseno, A. L.; Bao, Z. *Synth. Met.* **2007**, *157*, 257 – 260.

[190] Choi, H. H.; Cho, K.; Frisbie, C. D.; Sirringhands, H.; Podzorov, V. *Nat. Mater.* **2017**, *17*, 2.

[191] Yamashita, Y. *Sci. Technol. Adv. Mater.* **2009**, *10*, 024313.

[192] Klauk, H.; Halik, M.; Zschieschang, U.; Schmid, G.; Radlik, W.; Weber, W. *J. Appl. Phys.* **2002**, *92*, 5259–5263.

[193] Podzorov, V.; Menard, E.; Rogers, J. A.; Gershenson, M. E. *Phys. Rev. Lett.* **2005**, *95*, 226601.

[194] Kubozono, Y.; He, X.; Hamao, S.; Teranishi, K.; Goto, H.; Eguchi, R.; Kambe, T.; Gohda, S.; Nishihara, Y. *Eur. J. Inorg. Chem.* **2014**, *24*, 3806–3819.

[195] Sarker, B. K.; Khondaker, S. I. *Solid State Electron.* **2014**, *99*, 55 – 58.

[196] Zhu, M.; Liang, G.; Cui, T.; Varahramyan, K. *Solid State Electron.* **2005**, *49*, 884 – 888.

[197] Nelson, S. F.; Lin, Y.-Y.; Gundlach, D. J.; Jackson, T. N. *Appl. Phys. Lett.* **1998**, *72*, 1854–1856.

[198] Wang, C.; Dong, H.; Hu, W.; Liu, Y.; Zhu, D. *Chem. Rev.* **2012**, *112*, 2208–2267.

[199] Aradi, B.; Hourahine, B.; Frauenheim, T. *J. Phys. Chem. A* **2007**, *111*, 5678–5684.

[200] Elstner, M.; Porezag, D.; Jungnickel, G.; Elsner, J.; Haugk, M.; Frauenheim, T.; Suhai, S.; Seifert, G. *Phys. Rev. B* **1998**, *58*, 7260–7268.

[201] Seifert, G.; Joswig, J. O. *WIREs: Comput. Mol. Sci.* **2012**, *2*, 456–465.

[202] Kubas, A.; Hoffmann, F.; Heck, A.; Oberhofer, H.; Elstner, M.; Blumberger, J. *J. Chem. Phys.* **2014**, *140*, 104105.

[203] Kubas, A.; Gajdos, F.; Heck, A.; Oberhofer, H.; Elstner, M.; Blumberger, J. *Phys. Chem. Chem. Phys.* **2015**, *17*, 14342–14354.

[204] Kubar, T.; Woiczikowski, P. B.; Cuniberti, G.; Elstner, M. *J. Phys. Chem. B* **2008**, *112*, 7937–7947.

[205] Oliveira, A. F.; Seifert, G.; Heine, T.; Duarte, H. A. *J. Braz. Chem. Soc.* **2009**, *20*, 1193 – 1205.

[206] Li, W.; Kotsis, K.; Manzhos, S. *Phys. Chem. Chem. Phys.* **2016**, *18*, 19902–19917.

[207] Frisch, M. J. et al. Gaussian 09 Revision D.01. Gaussian Inc. Wallingford CT 2009.

[208] Xie, Y.; Zheng, J.; Lan, Z. *J. Chem. Phys.* **2015**, *142*, 084706.

[209] Kobayashi, H.; Kobayashi, N.; Hosoi, S.; Koshitani, N.; Murakami, D.; Shirasawa, R.; Kudo, Y.; Hobara, D.; Tokita, Y.; Itabashi, M. *J. Chem. Phys.* **2013**, *139*, 014707.

[210] Baumeier, B.; Kirkpatrick, J.; Andrienko, D. *Phys. Chem. Chem. Phys.* **2010**, *12*, 11103–11113.

[211] Aghtar, M.; Liebers, J.; Strümpfer, J.; Schulten, K.; Kleinekathöfer, U. *J. Chem. Phys.* **2012**, *136*, 214101.

[212] Xin, Q.; Duhm, S.; Bussolotti, F.; Akaike, K.; Kubozono, Y.; Aoki, H.; Kosugi, T.; Kera, S.; Ueno, N. *Phys. Rev. Lett.* **2012**, *108*, 226401.

[213] Porath, D.; Bezryadin, A.; de Vries, S.; Dekker, C. *Nature* **2000**, *403*, 635–638.

[214] O'Neill, P.; Frieden, E. M. *Advances in Radiation Biology: DNA and Chromatin Damage Caused by Radiation*; Academic Press: New York, 1993; Chapter 17.

[215] Armitage, B. *Chem. Rev.* **1998**, *98*, 1171–1200.

[216] Burrows, C. J.; Muller, J. G. *Chem. Rev.* **1998**, *98*, 1109–1152.

[217] Cooke, M. S.; Evans, M. D.; Dizdaroglu, M.; Lunec, J. *FASEB J.* **2003**, *17*, 1195–1214.

[218] Rokhlenko, Y.; Cadet, J.; Geacintov, N. E.; Shafirovich, V. *J. Am. Chem. Soc.* **2014**, *136*, 5956–5962.

[219] Heller, A. *Faraday Discuss.* **2000**, *116*, 1–13.

[220] Kawai, K.; Majima, T. *Acc. Chem. Res.* **2013**, *46*, 2616–2625.

[221] Lewis, F. D.; Zhu, H.; Daublain, P.; Fiebig, T.; Raytchev, M.; Wang, Q.; Shafirovich, V. *J. Am. Chem. Soc.* **2006**, *128*, 791–800.

[222] Murphy, C. J.; Arkin, M. R.; Jenkins, Y.; Ghatlia, N. D.; Bossmann, S. H.; Turro, N. J.; Barton, J. K. *Science* **1993**, *262*, 1025–1029.

[223] Murphy, C. J.; Arkin, M. R.; Ghatlia, N. D.; Bossmann, S.; Turro, N. J.; Barton, J. K. *Proc. Natl. Acad. Sci.* **1994**, *91*, 5315–5319.

[224] Schuster, G. B. *Acc. Chem. Res.* **2000**, *33*, 253–260.

[225] Giese, B. *Acc. Chem. Res.* **2000**, *33*, 631–636.

[226] Giese, B.; Wessely, S. *Angew. Chem. Int. Ed.* **2000**, *39*, 3490–3494.

[227] Wan, C.; Fiebig, T.; Schiemann, O.; Barton, J. K.; Zewail, A. H. *Proc. Natl. Acad. Sci. USA* **2000**, *97*, 14052–14055.

[228] Lewis, F. D.; Liu, X.; J., L.; Miller, S. E.; Hayes, R. T.; Wasielewski, M. R. *Nature* **2000**, *406*, 51–53.

[229] Lewis, F. D.; Letsinger, R. L.; Wasielewski, M. R. *Acc. Chem. Res.* **2001**, *34*, 159–170.

[230] Hess, S.; Götz, M.; Davis, W. B.; Michel-Beyerle, M. E. *J. Am. Chem. Soc.* **2001**, *123*, 10046–10055.

[231] Lewis, F. D.; Zuo, X.; Liu, J.; Hayes, R. T.; Wasielewski, M. R. *J. Am. Chem. Soc.* **2002**, *124*, 4568–4569.

[232] Lewis, F. D.; Liu, J.; Zuo, X.; Hayes, R. T.; Wasielewski, M. R. *J. Am. Chem. Soc.* **2003**, *125*, 4850–4861.

[233] Takada, T.; Kawai, K.; Tojo, S.; Majima, T. *J. Phys. Chem. B* **2003**, *107*, 14052–14057.

[234] Takada, T.; Kawai, K.; Fujitsuka, M.; Majima, T. *Proc. Natl. Acad. Sci.* **2004**, *101*, 14002–14006.

[235] Kanvah, S.; Joseph, J.; Schuster, G. B.; Barnett, R. N.; Cleveland, C. L.; Landman, U. *Acc. Chem. Res.* **2010**, *43*, 280–287.

[236] Genereux, J. C.; Barton, J. K. *Chem. Rev.* **2010**, *110*, 1642–1662.

[237] Heim, T.; Deresmes, D.; Vuillaume, D. *J. Appl. Phys.* **2004**, *96*, 2927–2936.

[238] Kumar, A.; Hwang, J.-H.; Kumar, S.; Nam, J.-M. *Chem. Commun.* **2013**, *49*, 2597–2609.

[239] Giese, B.; Amaudrut, J.; Köhler, A.-K.; Spormann, M.; Wessely, S. *Nature* **2001**, *412*, 318–320.

[240] Joseph, J.; Schuster, G. B. *J. Am. Chem. Soc.* **2006**, *128*, 6070–6074.

[241] Watson, J. D.; Crick, F. H. C. *Nature* **1953**, *171*, 737.

[242] Wilkins, M. H. F.; Stokes, A. R.; Wilson, H. R. *Nature* **1953**, *171*, 738.

[243] Stewart, R. F.; Jensen, L. H. *J. Chem. Phys.* **1964**, *40*, 2071–2075.

[244] Duchesne, J.; Depireux, J.; Bertinchamps, A.; Cornet, N.; Van Der Kaa, J. M. *Nature* **1960**, *188*, 405.

[245] Eley, D. D.; Spivey, D. I. *Trans. Faraday Soc.* **1962**, *58*, 411–415.

[246] Braun, E.; Eichen, Y.; Sivan, U.; Ben-Yoseph, G. *Nature* **1998**, *391*, 775–778.

[247] Shu, J.-J.; Wang, Q.-W.; Yong, K.-Y. *Phys. Rev. Lett.* **2011**, *106*, 188702.

[248] Yoo, K.-H.; Ha, D. H.; Lee, J.-O.; Park, J. W.; Kim, J.; Kim, J. J.; Lee, H.-Y.; Kawai, T.; Choi, H. Y. *Phys. Rev. Lett.* **2001**, *87*, 198102.

[249] Endres, R. G.; Cox, D. L.; Singh, R. R. P. *Rev. Mod. Phys.* **2004**, *76*, 195–214.

[250] Faraggi, M.; Broitman, F.; Trent, J. B.; Klapper, M. H. *J. Phys. Chem.* **1996**, *100*, 14751–14761.

[251] Caruso, T.; Carotenuto, M.; Vasca, E.; Peluso, A. *J. Am. Chem. Soc.* **2005**, *127*, 15040–15041.

[252] Caruso, T.; Capobianco, A.; Peluso, A. *J. Am. Chem. Soc.* **2007**, *129*, 15347–15353.

[253] Capobianco, A.; Carotenuto, M.; Caruso, T.; Peluso, A. *Angew. Chem. Int. Ed.* **2009**, *48*, 9526–9528.

[254] Yang, X.; Wang, X.-B.; Vorpagel, E. R.; Wang, L.-S. *Proc. Natl. Acad. Sci. USA* **2004**, *101*, 17588–17592.

[255] Jortner, J.; Bixon, M.; Langenbacher, T.; Michel-Beyerle, M. E. *Proc. Natl. Acad. Sci.* **1998**, *95*, 12759–12765.

[256] Jortner, J.; Bixon, M.; Langenbacher, T.; Michel-Beyerle, M. E. *Proc. Natl. Acad. Sci. USA* **1998**, *95*, 12759.

[257] Prunkl, C.; Berndl, S.; Wanninger-Weiß, C.; Barbaric, J.; Wagenknecht, H.-A. *Phys. Chem. Chem. Phys.* **2010**, *12*, 32–43.

[258] Capobianco, A.; Landi, A.; Peluso, A. *Phys. Chem. Chem. Phys.* **2017**, *19*, 13571–13578.

[259] Capobianco, A.; Caruso, T.; Celentano, M.; D'Ursi, A. M.; Scrima, M.; Peluso, A. *J. Phys. Chem. B* **2013**, *117*, 8947–8953.

[260] Capobianco, A.; Peluso, A. *RSC Adv.* **2014**, *4*, 47887–47893.

[261] Capobianco, A.; Caruso, T.; Peluso, A. *Phys. Chem. Chem. Phys.* **2015**, *17*, 4750–4756.

[262] Capobianco, A.; Caruso, T.; Celentano, M.; La Rocca, M. V.; Peluso, A. *J. Chem. Phys.* **2013**, *139*, 145101–4.

[263] Capobianco, A.; Caruso, T.; D'Ursi, A. M.; Fusco, S.; Masi, A.; Scrima, M.; Chatgilialoglu, C.; Peluso, A. *J. Phys. Chem. B* **2015**, *119*, 5462–5466.

[264] Borrelli, R.; Domcke, W. *Chem. Phys. Lett.* **2010**, *498*, 230 – 234.

[265] Borrelli, R.; Thoss, M.; Wang, H.; Domcke, W. *Mol. Phys.* **2012**, *110*, 751–763.

[266] Borrelli, R.; Di Donato, M.; Peluso, A. *Biophys. J.* **2005**, *89*, 830–841.

[267] Borrelli, R. *Chem. Phys. Lett.* **2007**, *445*, 84.

[268] Reanaud, N.; Berlin, Y. A.; Lewis, F. D.; Ratner, M. A. *J. Am. Chem. Soc.* **2013**, *135*, 3953–3963.

[269] Levine, A. D.; Iv, M.; Peskin, U. *Chem. Sci.* **2016**, *7*, 1535–1542.

[270] Xiang, L.; Palma, J. L.; Bruot, C.; Mujica, V.; Ratner, M. A.; Tao, N. *Nat. Chem.* **2015**, *7*, 221–226.

[271] Smit, R. H. M.; Untiedt, C.; Rubio-Bollinger, G.; Segers, R. C.; van Ruitenbeek, J. M. *Phys. Rev. Lett.* **2003**, *91*, 076805.

[272] O'Neill, M. A.; Barton, J. K. *J. Am. Chem. Soc.* **2004**, *126*, 11471–11483.

[273] Genereux, J. C.; Barton, J. K. *Chem. Rev.* **2010**, *110*, 1642–1662.

[274] Sakurai, J. J.; Napolitano, J. *Modern Quantum Mechanics*, 2nd ed.; Cambridge University Press, 2017.

[275] Park, T. J.; Light, J. C. *J. Chem. Phys.* **1986**, *85*, 5870–5876.

[276] Tal-Ezer, H.; Kosloff, R. *J. Chem. Phys.* **1984**, *81*, 3967–3971.

[277] Nauts, A.; Wyatt, R. E. *Phys. Rev. Lett.* **1983**, *51*, 2238–2241.

[278] Friesner, R. A.; Wyatt, R. E. *J. Chem. Phys.* **1985**, *82*, 1973–1982.